Electronic Thesis and Dissertation Repository

6-12-2023 10:00 AM

In Utero Magnetic Resonance Relaxometry for Fetal Tissue Development

Simran Sethi, *Western University*

© Simran Sethi 2023

Follow this and additional works at: https://ir.lib.uwo.ca/etd

Part of the Medical Biophysics Commons

Abstract

Fetal life is a significant period of human development because organ systems that sustain life outside the uterus begin to develop during this time. A necessary process that begins during fetal life is myelination, which is the process by which myelin, a lipid-rich substance, is wrapped around neurons in the brain to increase the speed of action potential transmission. Since myelination is critical for the normal function of the central nervous system, fetal myelin assessment is important for understanding neurodevelopment and neurodegeneration, such as intrauterine growth restriction (IUGR).

Magnetic resonance imaging (MRI) is an excellent tool for visualizing fetal anatomy and identifying pathology. Relaxometry quantifies T_1, T_2, and T_2^* relaxation times, which are MR parameters that reflect fundamental tissue properties sensitive to the tissue microenvironment, providing an interpretation of images in absolute units. For the first time, fetal tissue T_1 and T_2^* relaxation times were successfully quantified in uncomplicated pregnancies as a function of gestational age (GA) in the third trimester.

A tissue microenvironment that can be investigated by MR relaxometry is myelin water. Myelin water imaging (MWI) uses MR relaxometry to visualize the aqueous components associated with myelin sheath to quantify myelin water fraction (MWF), a validated myelin marker. Moving to a guinea pig model of pregnancy, MWI was successfully conducted in the fetal environment as MWF was quantified in various fetal brain regions late in gestation. To investigate the effects of IUGR on myelination *in utero*, MWI was applied in a guinea pig model of natural IUGR late in gestation. MWF was significantly reduced in different brain regions of guinea pigs with IUGR compared to those without IUGR. Furthermore, the study highlighted the utility of MWF as a functional marker for IUGR.

In conclusion, this dissertation demonstrates using MR relaxometry to quantify T_1 and T_2^* relaxation times of fetal tissues throughout pregnancy and assess fetal brain myelin content in both a normal and IUGR environment. The findings demonstrate MR relaxometry's utility in assessing fetal tissue development *in utero*.

Summary for Lay Audience

Fetal life is an important period of human development because organs and tissues, which help us survive outside the womb, undergo significant development. Furthermore, pathologies, such as intrauterine growth restriction (IUGR), developed during this developmental period can lead to life-long consequences, such as a reduction in brain myelin content; myelin is a fatty substance found in the brain that is necessary for normal cerebral functioning. This thesis investigates fetal tissue development and the effect of IUGR on fetal brain myelin using magnetic resonance imaging (MRI).

Human fetal tissue development was first investigated by measuring various tissues' MR tissue relaxation times in normal pregnancies in the third trimester. The study found that the parameters of most analyzed tissues did not change because these tissues are well-differentiated before the third trimester.

A specialized MRI technique that quantifies relaxation times has been used previously to assess myelin in adults, children, and neonates but never in fetuses. Before assessing the effects of IUGR on fetal brain myelin, the feasibility of the specialized technique was determined in a guinea pig model of pregnancy late in gestation. Myelin content was successfully measured in different brain regions, with initial data showing the myelin content to be less in fetuses with IUGR.

Moving to a guinea pig model of natural IUGR, it was found that myelin content in all analyzed brain regions was significantly less in fetuses with IUGR than those without IUGR. This was the first time that the IUGR-related reduction in myelin was visualized non - invasively with MRI.

The research in this thesis is important because it demonstrates MRI's utility in assessing fetal tissue development by measuring tissue relaxation times and the impact of pathologies on biological processes, such as the IUGR-related reduction in myelin. These results promote the use of MRI to assess fetal tissue development as well as the possibility of myelin as a biomarker for IUGR.

Co-Authorship Statement

Chapters 2, 3, and 4 of this thesis contain original research studies completed in collaboration with other authors. Acknowledgements of the contributions from myself and others to this work are described below for each project.

Chapter 2 was adapted from an original research manuscript published in the *Journal of Magnetic Resonance Imaging,* Volume 54, Issue 1, pages 113-121 DOI: 10.1002/jmri.27547 [1]. The work, entitled "Quantification of 1.5 T T_1 and T_2^* Relaxation Times of Fetal Tissues in Uncomplicated Pregnancies", was published in 2021 and authored by Simran Sethi, Stephanie A. Giza, Estee Goldberg, Mary-Ellen E.T. Empey, Sandrine de Ribaupierre, Genevieve D.M. Eastabrook, Barbra de Vrijer, and Charles A. McKenzie. As first author, I was involved in data collection, data analysis, interpretation, and preparation and submission of the manuscript. Stephanie Giza was involved in imaging data collection and data interpretation. Estee Goldberg and Mary-Ellen Empey were involved in data interpretation. Sandrine de Ribaupierre and Genevieve Eastabook provided guidance on data interpretation and manuscript revisions. Barbra de Vrijer and Charles McKenzie were responsible for study conception and design and provided guidance on data interpretation and manuscript revisions.

Chapter 3 was adapted from an original research manuscript published in the *Journal of Magnetic Resonance Imaging* in 2022 entitled "Feasibility of MRI Quantification of Myelin Water Fraction in the Fetal Guinea Pig Brain" DOI: 10.1002/jmri.28482 [2]. It was authored by Simran Sethi, Lanette J. Friesen-Waldner, Trevor P. Wade, Marc Courchesne, Karen Nygard, Ousseynou Sarr, Brian Sutherland, Timothy R.H. Regnault, and Charles A. McKenzie. As first author, I was involved in study design, imaging data collection, data analysis, interpretation, and preparation and submission of the manuscript. Lanette Friesen-Waldner was involved in data collection and animal care. Trevor Wade was involved in the implantation of pulse sequence changes. Marc Courchesne and Karen Nygaard were involved in histology and myelin staining. Ousseynou Sarr and Brian Sutherland were involved in *ex vivo* tissue collection and analysis. Timothy Regnault and Charles McKenzie were responsible for the study conception and design and provided guidance on data interpretation and manuscript revisions.

Chapter 4 was adapted from an original research manuscript that is in preparation for publication and entitled "Quantifying Myelin Water Fraction in a Guinea Pig Model of Spontaneous Intrauterine Growth-Restriction". It was authored by Simran Sethi, Lanette J. Friesen-Waldner, Timothy R.H. Regnault, and Charles A. McKenzie. As first author, I was involved in study design, imaging data collection, data analysis, interpretation, and preparation and submission of the manuscript. Lanette Friesen-Waldner was involved in data collection and animal care. Timothy Regnault and Charles McKenzie were responsible for the study conception and design and provided guidance on data interpretation and manuscript revisions.

Dedicated to my parents and brother.

Acknowledgements

To my supervisor, Dr. Charles McKenzie: thank you for welcoming me into the lab as an undergrad and then as a graduate student. Thank you for your kindness, patience, encouragement, faith, and for putting up with me these past six years. I feel fortunate to have benefited from your dedicated mentorship, which has been invaluable to my growth as a scientist.

To my advisory committee members, Dr. Corey Baron, Dr. Barbra de Vrijer, and Dr. Tim Regnault: thank you for the invaluable scientific discussions and for providing excellent guidance throughout my Ph.D.

To Dr. Lanette Friesen-Waldner: thank you for your support, advice, and mentorship throughout my time in the lab. I thoroughly enjoyed all our time spent in the lab and at the scanner and sharing recipes.

To Dr. Trevor Wade: thank you for your technical support and patience in helping me set up the mcDESPOT scans. Thank you for being on standby and helping us whenever something went wrong with the scans.

To Stephanie Giza: thank you for being a welcoming mentor when I first joined the lab as an undergrad, helping me navigate graduate school, and for your friendship.

To the McKenzie lab members, Lindsay Morris, Lauren Smith, Mary-Ellen Empey, and Dr. Takashi Hashimoto: thank you for making the lab a great workplace. Thank you for the conversations, friendships, and willingness to go on walks for coffee and treats.

To my friends: thank you so much for providing a welcoming escape. Thank you for the board game nights, thoughtful conversations, incredible support, and much-needed night outs. Thanks especially to Alicia for being an incredible roommate and friend and putting up with my craziness for the past three years.

To my cat, Mishti: thank you for putting up with my cuddles, kisses, and annoyance. You were a gift for getting into the Ph.D. and have made every day better since coming into my life.

To my family: I dedicate my thesis to you all, as I would not have made it here without your love, encouragement, and unconditional support over my academic career. To my older brother, thank you for being the best big brother and my confidante. To my parents, thank you for all the sacrifices you've made for us, as achieving our dreams would otherwise not be possible. I dedicate my thesis to you three.

Table of Contents

List of Tables

List of Figures

List of Appendices

List of Symbols, Acronyms, and Abbreviations

α	Flip angle (°)
γ	Gyromagnetic ratio (rad·s^{-1}·T^{-1})
h	Planck's constant
I	Spin quantum number
μm	Micrometer
ϕ	Initial angle of the net magnetization in the transverse plane
ω_0	Larmor frequency (Hz)
^{1}H	Hydrogen-1
3D	3-Dimensional
AGA	Appropriate for gestational age
aIUGR	Asymmetrical intrauterine growth restriction
ANOVA	One-way analysis of variance
ARC	Autocalibrating reconstruction for cartesian imaging
ASSET	Array coil spatial sensitivity encoding
AT	Adipose tissue
$\vec{B}_0$	Main magnetic field strength (T)
$\vec{B}_1$	RF pulse magnetic field strength (T)
BBVR	Brain-to-body volume ratio
BBWR	Brain-to-body weight ratio

BLVR	Brain-to-liver volume ratio
BLWR	Brain-to-liver weight ratio
BMI	Body mass index
BMP	Bone morphogenetic proteins
BMP4	Bone morphogenetic protein 4
BPlVR	Brain-to-placenta volume ratio
BPlWR	Brain-to-placenta weight ratio
BPrVR	Body -to-pregnancy volume ratio
BPrWR	Body-to-pregnancy weight ratio
bSSFP	Balanced steady-state free precession
BV	Body volume
BW	Body weight
CC	Corpus callosum
CNS	Central nervous system
CO_2	Carbon dioxide
CPR	Cerebroplacental ratio
CSE	Chemical-shift encoded
$DESPOT_1$	Driven equilibrium single pulse of observation of T_1
$DESPOT_2$	Driven equilibrium single pulse of observation of T_2
FL	Florida

FOR	Fornix
FOV	Field-of-view
GA	Gestational age
GM	Grey matter
GRE	Gradient echo
IDEAL-IQ	Iterative decomposition of water and fat with echo asymmetry and least-squares estimation
IEW	Intra-/extra-cellular water
IHC	Immunohistochemical
IQ	Intelligent quotient
IUGR	Intrauterine growth restriction
Kg	Kilogram
LFB	Luxol fast blue
m	Meter
MA	Massachusetts
MBP	Myelin basic protein
MCA	Middle cerebral artery
mcDESPOT	Multicomponent driven equilibrium single pulse of observation of T_1 and T_2
MD	Maryland
MRI	Magnetic resonance imaging

ms	Millisecond
MT	Magnetization transfer
MWF	Myelin water fraction
MWI	Myelin water imaging
O_2	Oxygen
PBS	Phosphate-buffered saline
PDFF	Proton-density fat fraction
PI	Pulsatility index
PLP	Proteolipid protein
PSW	Parasagittal white matter
RF	Radiofrequency
ROI	Region of interest
s	Second
SD	Standard deviation
SEM	Standard error of the mean
SGA	Small for gestational age
sIUGR	Symmetrical intrauterine growth restriction
SSFSE	Single-shot fast spin-echo
T	Tesla
T_1	Longitudinal relaxation time

T_1^*	Apparent longitudinal relaxation time
T_2	Transverse relaxation time
T_2^*	Apparent transverse relaxation time
TE	Echo time
TR	Repetition time
UAD	Umbilical artery doppler
UAL	Uterine artery ligation
URL	Uniform resource locators
WI	Wisconsin
WM	White matter

CHAPTER 1

1   Introduction

This introductory chapter provides the information necessary to understand the topics presented in the subsequent chapters of the thesis. A brief overview of human tissue development throughout the fetal period is presented before presenting a definition of intrauterine growth restriction (IUGR) and its impact on fetal neurodevelopment, specifically brain myelination. In addition, the fundamentals of magnetic resonance imaging (MRI) and myelin water imaging (MWI) techniques are thoroughly explained so the reader can appreciate the imaging modality's technical details, advantages, and limitations.

1.1   Fetal Life and Normal Development

A fetus is the unborn human that develops from an embryo. Following embryonic development, the fetal stage of development begins at approximately 10-11 weeks gestational age (GA) and continues until birth [3]. A normal fetus is characterized by the presence of all major body organs, although they may not all be fully developed or functional [4, 5]. In short, fetal life is a significant period of human development because organ systems, which sustain life outside the uterus, develop during this gestational period.

1.1.1   10 – 18 Weeks Gestation

Before the fetal period, the fetal heart is well developed as the 4 chambers of the heart are formed by seven weeks GA [6]. The brain makes up approximately 50% of the fetus' weight as neurons in the brain develop and begin to myelinate [7]. Breathing-like movements begin and are necessary for lung development rather than acquiring oxygen. By the end of the period, the producers of red blood cells are the bone marrow, liver, and spleen [8, 9]. The thyroid gland matures and produces hormones along with the liver synthesizing primary bile acids and the pancreas secreting insulin and glucagon [10-13].

Amniotic fluid is circulated by the fetus swallowing it and producing urine as the kidneys begin functioning [14]. Although the primary organs are present, such as the brain, they are only at the beginning of their development and have limited operation. The reproductive organs form quite rapidly, and the genitalia of the fetus can be differentiated [15]. In the fetal period, muscles, the brain, and other neurological pathways begin to develop, resulting in subtle movements and twitches [4, 5].

The first lipid depots are detected in the cheeks at around 14 weeks GA [16-18]. The primitive adipose lobules develop from head-to-toe and proximal-to-distal as their number increases until about 23 weeks before levelling off; adipose lobule size is linearly related to fetal crown-rump (i.e., cranial-to-caudal end of body) length [19]. The lungs' tertiary bronchial buds form the initial components of the respiratory tree at 16 weeks GA, with the terminal bronchioles forming by the end of this stage [20, 21].

This gestational period is also marked by sensory organ development as the eyes move to a forward-facing position while the ears lie flatter against the head. The structural parts of the cochlea are fully formed and functional as an auditory response can be first seen at 16 weeks GA [22-24].

1.1.2   19 – 27 Weeks Gestation

Myelination in the spinal cord occurs, starting with the medial longitudinal fasciculus [25]. The lungs consist of primitive alveoli as epithelial cell differentiation and surfactant production begin [26]. Hepatic hematopoiesis, which began at six weeks GA, reaches its maximal activity near the end of this developmental period. The bone marrow becomes the primary location of red blood cell synthesis by the end of the period [8, 9, 27]. Sulci first appear on the surface of the cerebral hemispheres, with the first being on the parieto-occipital fissure at 18.5 weeks GA as the fetus becomes viable at around 24 weeks GA [28, 29]. Around 25-29 weeks GA, the ganglion cells of the spiral nucleus in the cochlea connect inner hair cells to the temporal lobe and brain stem, resulting in the auditory system becoming functional [24].

Between 23-29 weeks GA, adipose tissue development consists primarily of an increase in adipose lobule size and the development of their capillary network and adipocytes [16]. Subcutaneous adipose tissue begins development later than subfascial, intramuscular, and subserous adipose tissue and continuously covers the whole body till birth [30].

1.1.3   28 – 40 Weeks Gestation

This developmental period of gestation is dominated by rapid weight gain as dramatic morphological changes tend not to be observed in the third trimester [31]. Although the lungs are not fully mature, the terminal respiratory sacs develop to become functioning alveoli; pulmonary blood flow increases during the third trimester in readiness for the essential circulatory changes at birth [26]. The liver is histologically complete, although it may have accelerated growth in morphology and function after approximately 32 weeks GA [32].

The fetus is considered full-term between 37 and 40 weeks GA. Birth is imminent and likely to occur as the fetus is sufficiently developed for survival outside the uterus [33]. Before birth, the average crown-to-rump length is 35.5-40.5 cm, and the fetus weighs approximately 2.5-4 kg. Since a newborn is no longer confined to the fetal position, the average length from head-to-foot is approximately 51 cm at birth [34].

During the last 10 weeks of gestation, body weight increases linearly with GA as the amount of adipose tissue in the body rapidly increases [35, 36]. Most adipose tissue the fetus acquires during the last weeks of gestation is subcutaneous. At the end of the gestational period, lipid depots contain various adipocyte sub-populations, which differ primarily by their degree of lipid filling and, hence, by size [37]. A brief visual overview and summary of the fetal development period are presented in Figure 1.1.

10 – 18 Weeks GA	19 – 27 Weeks GA	28 – 40 Weeks GA

- Myelination begins in brain
- Hematopoiesis in bone marrow, liver & spleen
- Genitalia is differentiated
- Adipose tissue first detected in cheeks

- Myelination begins in spinal cord
- Lungs consist of alveoli
- Main sites of hematopoiesis: liver & bone marrow
- Increase in adipose lobule size
- Fetus becomes viable

- Rapid weight gain
- Alveoli become functional
- Adipose tissue rapidly increases
- Fetus reaches full-term

Figure 1.1. A brief overview of the human fetal development period.

1.2 Placenta

The human placenta is a temporary, circular discoid-shaped organ that develops from the blastocysts after embryo implantation in the uterine wall [38]. The placenta is necessary for pregnancy because its central role is to facilitate gas, nutrients, and waste exchange between the maternal and fetal circulatory systems that do not come into physical contact with each other. It is also a vital endocrine organ because it produces hormones that regulate both fetal and maternal physiology throughout pregnancy [38]. The proper functioning of the placenta is essential to ensure the proper development of the fetus throughout the gestational period.

1.2.1 Development

The placenta begins to develop when the embryonic pole of the blastocyst implants into the uterine endometrium at around 4 weeks GA [39, 40]. The outer layer of the blastocyst becomes the trophoblast, forming the placental outer layer. The outer layer is further divided into two layers: cytotrophoblast and syncytiotrophoblast. The cytotrophoblast is the underlying layer of the trophoblast, while the syncytiotrophoblast is a multi-nucleated continuous cell layer that overlies the cytotrophoblast. The syncytiotrophoblast forms

from the differentiation and fusion of the underlying cytotrophoblast cells throughout placental development. Hence, the syncytiotrophoblast forms the outermost layer and contributes to the barrier function of the placenta, interacting directly with the maternal circulation and is involved in the exchange of materials between the maternal-fetal circulations [41, 42]. Although maternal blood supply to the placenta is established by 14 weeks GA, the placenta grows in volume throughout gestation [43].

1.2.2   Circulation

The placenta can be divided into maternal and fetal components [40]. The maternal component develops from the decidua basalis, while the fetal component develops from the chorion frondosum. The placenta is haemomonochorial, as the maternal and fetal circulations are separated by a single layer of trophoblast cells [44].

The maternal-placental circulation begins with the maternal blood entering the placenta through the decidual spiral arteries to perfuse the intervillous space. The fetal-placental circulation consists of the umbilical arteries carrying the deoxygenated and nutrient-depleted fetal blood from the fetus to the villous core vessels. The functional exchange of oxygen, nutrients, and waste occurs in the intervillous space as maternal and fetal blood flow around the terminal villi [43]. Following the exchange, the in-flowing maternal blood pushes the deoxygenated blood into the venous orifices in the basal place and then through the uterine veins to the maternal circulation [43, 45]. Meanwhile, the umbilical vein carries the oxygenated and nutrient-rich blood to the fetus [43].

At term, the placenta weighs 500-600 grams, has approximately 120 spiral arterial entries to the intervillous space, and has 15-28 cotyledons, each containing 10-12 terminal villi [40, 45, 46]. Maternal blood flow to the placenta is 600-700 mL/minute at term and has an average perfusion rate of 176 ± 24 ml/100 gram/minute in the latter half of gestation (Figure 1.2) [43, 47].
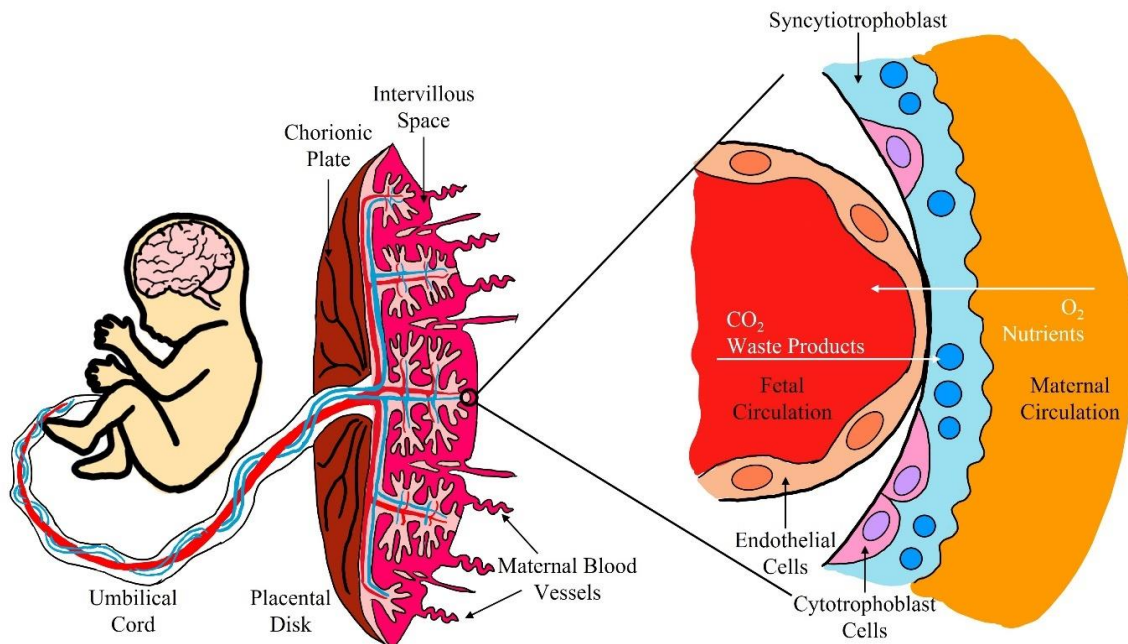
Figure 1.2. Visual representation of the human placental disk with a close-up of the placental villi structure depicting the exchange of gases, nutrients, and waste products between the fetal and maternal circulations. This figure was reproduced with permission from Dr. Christiane Albrect, University of Bern.

1.2.3   Placenta and Fetal Growth

Fetal growth depends on fetal oxygen and nutrient demand, determined by its genetic growth potential. As previously mentioned, the placenta mediates fetal circulation with maternal circulation, thus, being essential to proper fetal development. Consequently, fetal development can be dictated by a three-compartment model – the mother, placenta, and fetus – with each compartment having its own metabolism and function while interacting with each other [38, 48, 49]. In short, the fetus relies on the maternal supply of oxygen and nutrients, supplied through the placenta, for proper growth [43].

The maternal-placental supply of oxygen and nutrients is affected by maternal nutrition and metabolism, maternal-fetal concentration gradient, uteroplacental blood flow, placental size, and placental function [38, 50]. Suppose the fetus does not receive the appropriate oxygen and nutrients to grow as programmed due to an issue with one or

more of the above-mentioned factors. In that case, the fetus is said to experience intrauterine growth restriction (IUGR).

1.3   Intrauterine Growth Restriction

1.3.1   Classification

Intrauterine growth restriction (IUGR) is an obstetrical complication where a fetus demonstrates diminished growth and cannot grow to its programmed genetic weight and size potential [51]. Following World Health Organization standards, Canada defines fetuses with IUGR as below the 10th percentile for their GA with a cut-off birth weight of 2500 grams at birth [52]. IUGR is a leading cause of fetal and neonatal morbidity and mortality, second only to prematurity [53]. The complication is often the result of different underlying pathological conditions, with the primary being placental insufficiency, exposing the IUGR fetus to both short-term consequences, such as respiratory distress syndrome, fetal hypoxia and acidosis, and long-term consequences, such as an increased risk of metabolic syndrome and cardiovascular disease, hypertension, and insulin resistance [54-56]. Thus, an expanding area of research is needed to better understand the causes of IUGR and its impact on life-long health.

According to traditional classification, IUGR phenotypically presents as either asymmetrical IUGR (aIUGR) or symmetrical IUGR (sIUGR) [56]. Fetuses with aIUGR, the more common of the two, have disproportionate body dimensions and a low ponderal [i.e., weight (grams) /length (cm^3)] index at birth. aIUGR manifests in the latter half of the gestational period as fetuses with aIUGR are observed to have normal estimated fetal weight and measurements until the third trimester, after which a decline in growth is observed [57, 58]. aIUGR is often accompanied by 'brain sparing,' which is a protective mechanism to maintain brain size and head circumference throughout gestation to maximize fetal survival by redistributing cardiac output [57, 59, 60]; this is also accompanied by a reduction in soft tissue mass and skeletal muscle [61, 62]. On the other hand, sIUGR manifests earlier in gestation, where brain growth inhibition is proportional to weight, length, and head circumference reductions, as an sIUGR fetus tends to have a

normal ponderal index at birth [57, 58, 61, 63]. Unlike aIUGR, the causes of sIUGR are likely due to genetic abnormalities and congenital infections as opposed to malnutrition due to placental insufficiency [56]. In addition, sIUGR can be challenging to distinguish from fetuses that are constitutionally small for their GA (SGA) because although they are proportionally similar, SGA fetuses are unlikely to have the same risk for poor perinatal outcomes as IUGR fetuses [56]. Hence, separating IUGR into asymmetrical and symmetrical is often seen as outdated, and the focus primarily falls on aIUGR (Figure 1.3).

As the definition indicates, the obvious classifiers of IUGR are related to the size and weight of the fetus, such as body weight (BW). Other common parameters in classifying IUGR are weight ratios that include the brain. For instance, one parameter is the brain-to-liver weight ratio (BLWR). IUGR fetuses have a high BLWR because they tend to have a normal head circumference and brain weight accompanied by a decreased liver weight that is not proportional due to brain sparing [64, 65]. In addition to BLWR, brain-to-liver volume ratio (BLVR), as determined by MRI, has been validated in identifying aIUGR, acting as an alternate non-invasive *in utero* marker to BLWR [66]. Other weight markers, and their respective volume markers, used for IUGR classification include body weight (BW) and volume (BV), brain-to-placenta weight ratio (BPlWR) and volume ratio (BPlVR), and brain-to-body weight ratio (BBWR) and volume ratio (BBVR) [64, 67-70].

Normal Growth   Asymmetrical IUGR   Symmetrical IUGR
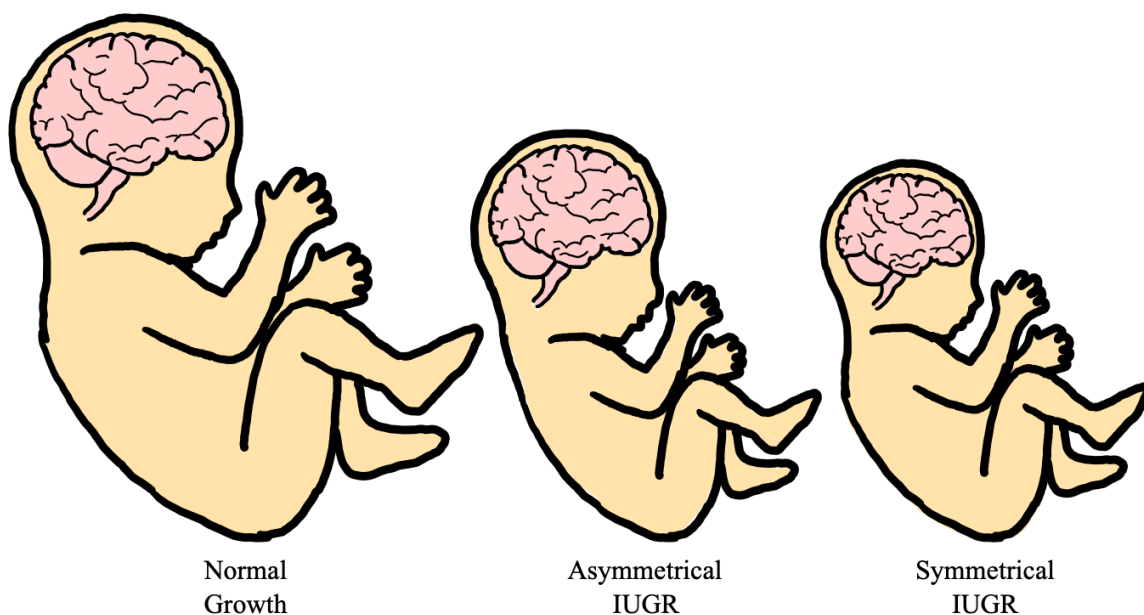
Figure 1.3. Visual comparison of a fetus with normal growth (left), a fetus with asymmetrical IUGR (middle), and a fetus with symmetrical IUGR (right).

Other than size and body proportions, IUGR-related changes in placental blood flow, blood oxygenation, and fetal circulation can be investigated by imaging modalities like ultrasound, Doppler ultrasounds, and MRI [66, 71, 72]. Umbilical artery Doppler (UAD) ultrasound measurements are a functional method of identifying and assessing IUGR. The presence of abnormal UAD waveforms, such as reversed or absent end-diastolic waves, is excellent in identifying severe cases of IUGR but often fails to identify less severe cases early and late in gestation due to low sensitivity [73]. The cerebroplacental ratio (CPR), which is the ratio of the pulsatility index (PI) of the middle cerebral artery (MCA) to the PI of the umbilical artery, is another parameter in identifying IUGR. CPR is useful in detecting minor changes in placental resistance and identifying brain sparing since cerebral resistance is decreased to allow for increased cardiac perfusion to the brain [74, 75].

1.3.2   Etiology

Fetal growth depends on three main factors: the fetus' programmed genetic growth potential, maternal environment, and placental sufficiency in transporting the necessary

nutrients and gases to the fetus [76]. IUGR occurs when one or more of these essential factors is compromised, resulting in a substandard *in utero* environment that cannot promote normal fetal growth and development. Fetal causes of IUGR include genetic-chromosomal abnormalities, congenital malformations, viral infections, and multiple fetuses [69, 77-80]. Maternal factors include chronic hypoxia, such as from living at high altitudes, smoking, undernutrition, overnutrition, hypertension, pre-eclampsia, vascular and renal disease, diabetes, autoimmune diseases, anaemia, environmental choices such as substance use and abuse, and prior incidence of IUGR [74, 76, 78, 80-83]. Furthermore, epidemiological studies show IUGR to be associated with maternal age, maternal stature, parental ethnicity, socioeconomic status, and parental education. For instance, the incidence of IUGR is six times higher in developing countries than developed countries [63, 69, 81, 83, 84]. Placental causes include placenta previa, placental infarcts, abnormal cord insertion, placental abruption, or multiple gestations [61]. In short, approximately 60% of IUGR is idiopathic, resulting from a combination of factors, most of which are due to improper placental development and/or function; this impairment is known as placental insufficiency [61, 63, 85].

1.3.3   Placental Insufficiency

As previously mentioned, the placenta provides the fetus with water, oxygen, and all essential nutrients, proteins, and hormones while removing fetal excretory products [38]. Placental insufficiency describes any impairment in placental function that disrupts the intended movement of sufficient oxygen and nutrients from the maternal to fetal circulation for fetal growth. This insufficiency or dysfunction can arise from numerous reasons, such as failed trophoblast invasion, thrombo-occlusive lesions to placental villi, increased umbilical cord length, defects in the development of terminal villi, reduced density of stem arteries, and abnormal patterning of the chorionic plate [86-90]. These changes can lead to inefficient blood flow, subsequently leading to insufficient transfer of oxygen, glucose, nutrients, and amino acids to the fetus, resulting in IUGR [60, 91-94]. Hence, the fetus has no choice but to change its metabolic and developmental processes to ensure survival in substandard conditions at the expense of its programmed genetic growth.

1.3.4   IUGR and Neurological Consequences

The consequences of IUGR are evident in almost every body system, including the nervous system. These consequences manifest in structural deficits, such as a smaller head circumference, a decrease in grey matter (GM), cerebral, hippocampal, and total brain volume, thinner cortex and altered gyrification, and an overall reduction in the total number of brain cells [68, 95-99].

An association between IUGR and functional neurological deficits is also apparent in most age groups, beginning in childhood; these deficits include autism spectrum disorder, attention deficit disorder, and cerebral palsy [58, 100, 101]. Some minor effects of IUGR also manifest in childhood, such as difficulty with attention, impaired memory, deficits in cognitive skills, learning difficulties, poor academic performance, behaviour problems, deficits in mathematical abilities, and reduced intelligent quotient (IQ) scores [63, 100-103]. For instance, children of 6-7 years who were growth-restricted had lower developmental scores, mainly in coordination, lateralization, presence of associated movements, and spatial and graph motor skills; their cognition, neurodevelopmental performance, and somatic growth were also found to be lacking [104]. At two years of age, IUGR fetuses were at a higher risk of neurodevelopmental deficits, which manifested in an abnormal score in an age & stage questionnaire (communication, gross motor, fine motor, problem-solving, and personal-social) [105]. Furthermore, children with IUGR born at-term scored low, and those born pre-term scored even lower on all the following neurodevelopmental assessments: cognitive, language, motor, behaviour, vision, hearing, and sleep [106].

The neurological deficits of IUGR-born children continue beyond childhood and are evident in adolescence and young adulthood. For example, in a sample of 106 Finnish 10-year-old children, SGA children had a higher incidence of failing at school, poor academic achievement, inattentiveness, and low verbal IQ score compared to appropriate for GA (AGA) children [107]. Birth-weight centile at term was found to positively correlate with school performance of 12-year old Dutch children, with the $\leq 10^{th}$ centile children having the lowest scores [108]. One study by Issacs *et al.* found IUGR-born 13-

year-olds to have poor memory, numerical operation skills, and mathematical reasoning compared to age-matched controls [109]. Geva *et al.* found late-onset IUGR children to have reduced IQ scores and deficits in short-term memory of auditory or visio-spatially presented information while controlling for sex and general cognitive ability at 10 years of age [103]. A study by Indredavik *et al.* followed the progress of IUGR neonates born at-term and pre-term through to 14 years of age; the study reported structural and functional deficits in Norwegian children. Along with a reduced head circumference, the children had increased inattention, hyperactivity, autism spectrum disorder score, psychiatric diagnosis, and decreased psychosocial function [100].

Behavioural and cognitive difficulties due to IUGR continue to become more complicated and severe with age, even manifesting in adulthood. A study in Norway found that at 19-20 years of age, individuals affected by IUGR had lower IQ scores when compared to those who were SGA and controls [110]. Following up with the previous study, young adults (19-20 years) affected by IUGR and born at-term had lower scores on attention, executive, and memory domains; the IUGR young adults also had lower scores on six of 46 measures on neuropsychological tests [111]. Furthermore, IUGR-born adults have an increased risk of epilepsy, schizophrenia, and psychiatric hospitalizations [112].

1.4   Fetal Myelination

In humans, brain development is a dynamic and complex process that occurs rapidly throughout gestation and continues after birth. At birth, the human brain is approximately 25% of its adult weight, 25% of the fetus' total body mass, and utilizes 80% of all consumed energy [113]. By the end of the second trimester, fetal brain growth rate is at its peak, as the brain weighs approximately 130 grams. At this point in the gestational period, myelination begins as most neurons have formed and arrived at their final location.

1.4.1   Myelin

Myelin is a lipid-rich substance that surrounds nerve cell axons. In the human brain, myelin is primarily found in the white matter (WM), making up approximately 50% of its

dry weight and giving WM its distinctive colour. Myelin is also present in grey matter (GM), although in much smaller quantities [114]. Myelination, which is the establishment of the myelin lipid bilayer, is essential for normal brain function and a cornerstone of human neurodevelopment. An accurate assessment of myelin *in utero* is extremely important for a comprehensive understanding of human neurodevelopment and neurodegeneration.

In the central nervous system (CNS), myelin is produced by oligodendrocytes, where one oligodendrocyte can myelinate up to 50 nerve cell axons. Oligodendrocytes are glial cells that ensheath axons to create a multi-layer concentric pattern of myelin, leaving unmyelinated nodes at regular intervals along the axons; these nodes are referred to as the nodes of Ranvier [115]. It is speculated that axons send signals to initiate myelination, such as non-receptor tyrosine kinase Fyn [116]. Once an oligodendrocyte attaches to an axon, architectural changes in the oligodendrocyte membrane occur so that the membrane can be extended and wrap the axons to myelinate them. Following the wrapping of the oligodendrocyte around the axon, myelin grows in thickness and along axons using two coordinated motions: wrapping around the axon on top of the previously deposited membrane and extending the myelin membrane towards the nodes [117]. The communication between the oligodendrocyte and axons ensures the correct spacing of the myelin sheath and that it has achieved the appropriate thickness and compactness to carry out its essential roles. On average, the length of the myelin sheath ranges from 500 to 2000 μm [118].

The dry composition of myelin consists of 70%-85% lipids and 30%-15% proteins [119]. The lipid composition of myelin comprises 40% cholesterol, 40% phospholipids, and 20% glycolipids [120]. As for proteins, the proteolipid protein (PLP) and myelin basic protein (MBP) account for 50% and 30% of the proteins, respectively [121]; other proteins include myelin oligodendrocyte glycoprotein, myelin-associated glycoprotein, and cyclic nucleotide phosphodiesterase.

For the correct functioning of myelin, the lipids and proteins must be placed correctly along the axon. Due to the high lipid/protein ratio, close packing and tight organization of

the myelin sheath are achieved through non-covalent interactions between lipids and myelin proteins [115]. Both PLP and MBP are essential for the compactness of myelin and interact closely with the lipid bilayers. Oligodendrocytes express PLP, which is extremely lipophilic as it has a high affinity for cholesterol [122, 123]. MBP, also expressed by oligodendrocytes, embeds in the membrane to form a barrier to prevent repetitive cytoplasmic and membrane-bound proteins from entering the myelin lamellae [124, 125].

The primary role of myelin is to speed up action potential velocity by acting as an electrical insulator [126]. This increase in velocity is due to action potential transmission only occurring at the nodes of Ranvier. Essentially, an action potential generated at one node of Ranvier results in a current flowing passively along the myelinated axon until the next node of Ranvier is reached. The current flow then generates an action potential in the neighbouring node as the cycle is repeated along the length of the axon. This process is known as saltatory conduction because the action potential "jumps" from one node to another [126]. As a result, the conduction velocity of action potentials is increased to 70-120 m/s along myelinated axons from 0.5-2 m/s along unmyelinated axons [127]. In addition to its primary role, myelin has been suggested to contribute to neuroplasticity, including neuronal functions, and provide metabolic support to axons [128-130]. Thus, myelin is necessary for functioning of the brain (Figure 1.4).
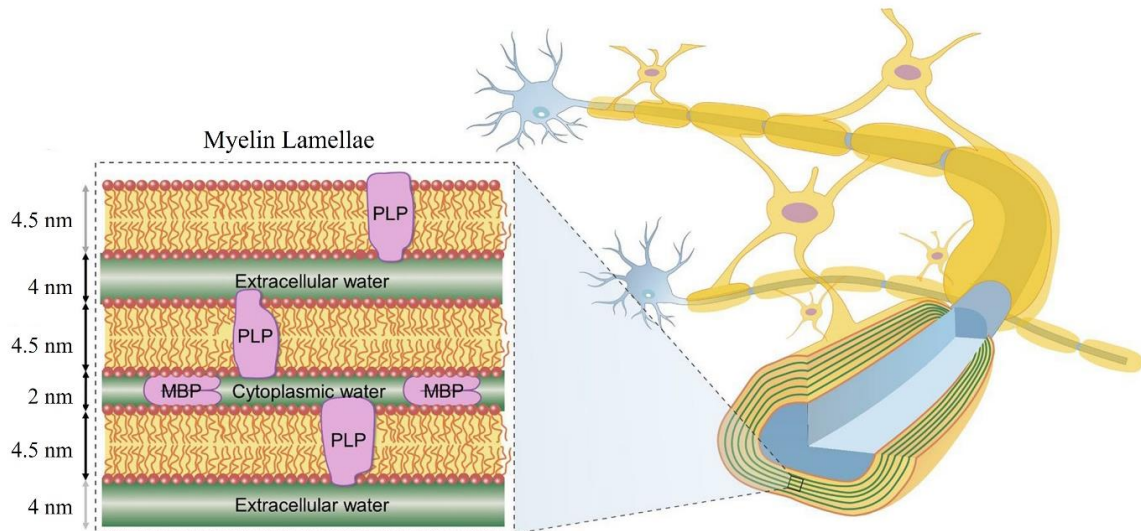
Figure 1.4. A magnified view of the myelin lamella structure with two lipid bilayers. This figure was adapted with permission from Lee *et al.* J Magn Reason Imaging 2020.

In the human brain, myelination begins in the fifth fetal month as the first evidence of the myelin sheath is seen at approximately 18 weeks GA in the thalamus and 21 weeks GA in the internal capsule [7]. Before the initiation of active myelin synthesis, myelin phospholipids appear in the WM and only increase in expression throughout gestation [131]. Furthermore, proteins forming the myelin sheath are first seen in the brain at five weeks GA. Overall, the rate of myelination increases beyond the gestational period and continues into the second decade of life.

1.4.2   Markers for Myelin Development

Luxol fast blue (LFB) is a commonly used stain for myelin under light microscopy. LFB is a copper-phthalocyanine dye attracted to lipoproteins and hydrophobic domains of myelin [132]. It causes the myelin to appear blue as the base of the lipoprotein is replaced by the base of the dye. LFB is a commonly used marker for myelination to validate MRI and PET imaging results throughout gestation [133-136]. One consequence of LFB is that it is a regressive stain where the regression time can vary among samples, making it challenging to acquire accurate and precise quantitative measurements [137].

As previously mentioned, MBP is the second most prevalent protein in the CNS. It comprises approximately 30% of proteins and 10% of the dry weight of the myelin sheath [138]. Often called the 'executive molecule of myelin,' the structural protein is essential in forming the myelin sheath in the CNS as it stabilizes the myelin sheath structure via binding to the cytoplasmic surfaces of the cell membrane [139]. MBP is expressed in precursor oligodendrocytes and then transported to the axon for myelination; it has been observed peripheral to the ependyma at 9-10 weeks and in the anterior and lateral funiculi at 10-12 weeks [140, 141]. The first evidence of immunostaining for MBP in the human brain appears at 30 weeks GA in small amounts, with higher amounts of staining being more apparent at 40 weeks GA in superficial WM areas [142]. Since MBP is essential for both the formation and maturation of the myelin sheath, MBP immunohistochemistry is a common stain that accurately identifies brain myelin *in utero*.

1.4.3   Myelination in IUGR

In addition to the structural neurological consequences of IUGR mentioned in Section 1.2.4, another structural deficit in the brain due to IUGR is a delay and decrease in myelination. Post-mortem studies of newborns showed that those affected by IUGR had decreased brain myelin compared to GA-matched control counterparts [143]. Major consequences of IUGR due to placental insufficiency include chronic hypoxia and oxidative stress, which have been shown to inhibit oligodendrocyte differentiation and, hence, myelination. More specifically, oxidative stress particularly affects oligodendrocyte precursors because of their high iron content, high oxidative metabolism, and low endogenous glutathione levels [144]. Oligodendrocyte differentiation is controlled by a combination of inductive and repressive factors, mainly bone morphogenetic proteins (BMP) [145-147]. Of the 20 BMPs, BMP4 significantly inhibits oligodendrocyte differentiation [147, 148]. Elevated BMP4 signalling has been demonstrated in a rat model of IUGR; furthermore, oligodendrocyte precursor cells from this model retained increased BMP4 expression after being cultured post-natally [149].

1.4.4   Animal Models of IUGR and Placental Insufficiency

Animal models have been successfully used to study IUGR because they can mimic the numerous human conditions that can potentially contribute to IUGR; these conditions include maternal malnutrition, chronic hypoxia, reduction in uterine blood flow and placental size, and endocrine alterations [150]. A technique frequently used to induce IUGR in animal studies is uterine artery ligation (UAL), where the main uterine artery is ligated to reduce blood flow, gases, nutrients, and ions to the fetus while creating a hypoxic environment *in utero* during gestation [60, 91]. Although the effects of UAL on organogenesis are evident within hours [60, 151], this model has numerous limitations, including high maternal mortality during ligation surgery, high abortion rates, and variations in fetal weight [152, 153]. In addition, this technique does not always induce IUGR as collateral blood flow compensates for the reduced blood flow and nutrients from the UAL [154]. A more recent model of IUGR used in studies is spontaneous IUGR where poor intrauterine growth occurs naturally and without artificial interventions. The model minimizes the risks that are associated with inducing IUGR invasively and is similar to humans where IUGR occurs naturally. Furthermore, the model has been employed primarily in guinea pigs where IUGR occurs spontaneously due to litter variations [155-157].

1.4.5   Animal Models of IUGR and Changes in Myelination

The neurological consequences of IUGR, specifically changes in white matter development and myelination, have been demonstrated in multiple animal models. In fetal sheep, MBP immunoreactivity in WM areas of the brain was reduced due to acute and intermittent hypoxia produced by umbilical cord occlusion [158, 159]. A study of UAL-induced IUGR showed a delay in myelination in rats that experienced a moderate degree of IUGR along with WM lesions; this study also showed that the severity and longevity of WM damage positively correlated with the severity of IUGR as rats with severe IUGR experienced WM damage that persisted into adulthood [160]. In a guinea pig model of IUGR, Nitsos and Rees found a reduction in myelination and the number of myelinated fibres in the IUGR population. This study also showed that the myelin sheath's thickness was disproportionately thin compared to the axonal diameter in IUGR fetuses [161]. More recently, Piorkowska *et al.* indicated a decrease in myelination in

IUGR guinea pigs compared to GA-matched control guinea pigs as measured using MBP immunohistochemistry and LFB [162].

1.4.6 Guinea Pig Model of IUGR and Fetal Brain Development

Of the IUGR animal models discussed in the previous section, the guinea pig is a better model for studying neurologic developmental programming. Like humans, but unlike rats and mice, guinea pigs undergo significant brain development *in utero*. Both humans and guinea pigs experience rapid brain growth in the latter half of pregnancy, are born with a full complement of neuronal numbers, and begin brain myelination *in utero* [163-165]. Thus, any *in utero* insult should correspond with critical developmental periods, and the associated long-term outcomes can be more precisely translated to humans.

Along with similarities, differences between the human and guinea pig brain exist that need to be considered. For instance, the guinea pig brain is bigger and more functional at term relative to the human brain. Consequently, guinea pigs' motor, cognitive, and regulatory processes at birth compare to that of a human toddler [166]. Furthermore, human brain growth begins to plateau around two years of age, while the plateau occurs just before birth in guinea pigs [163]. Hence, the impact of *in utero* events resulting in impaired development will likely be amplified in the guinea pig brain. Additionally, the influence of post-natal environmental factors on *in utero* neurodevelopment is limited in the guinea pig brain. Nonetheless, the guinea pig brain's heightened functionality and comparative neuroanatomy are beneficial in assessing IUGR-related neurodevelopmental changes.

In addition to guinea pigs being an excellent model for neurologic development, the guinea pig is also an excellent model for pregnancy and IUGR. The guinea pig has a gestational period of ~68 days, longer than rats and mice but shorter than sheep and primates [167]. Furthermore, the guinea pig is easily bred due to its docile temperament and minimal breeding requirements, allowing significant environmental control [164]. Despite having more offspring in a litter than humans, guinea pigs still have lower offspring than rats and mice – 1-5 v. 8-12 [164]. Like the human placenta, the guinea pig placenta is also haemomonochorial and displays a deep trophoblast invasion [164]. In

addition to the anatomical similarities, the guinea pig has similarities with the human fetal/maternal transport barrier, including the transfer of glucose and amino acids. Thus, the guinea pig is a great model for pregnancy and IUGR, which likely explains its use by numerous IUGR studies [162, 164, 168].

1.5   Magnetic Resonance Imaging

Magnetic resonance imaging (MRI) was first reported in 1973 by Paul Lauterbur, and the first image of a human body part in 1977 by Peter Mansfield and Andrew Maudsley [169, 170]. In 1983, the modality was used to image pregnancy, becoming the latest imaging modality to image the fetus and the placenta [171]. Although the use of *in utero* MRI is limited relative to pediatric and adult MRI, the modality, in conjunction with ultrasound, has since become an indispensable tool for studying fetal tissue development and function [172]. MRI is a non-invasive modality that does not use ionizing radiation, which is crucial when studying a vulnerable population [173]. It provides visualization of the entire uterus in a single volume due to its large field of view, excellent multi-parametric soft tissue contrast, and multiple sources of contrast in a single examination [174, 175]. Thus, MRI can provide valuable insight into the study of overall fetal tissue development, such as fetal brain myelination.

1.5.1   Spin

Nuclear magnetic resonance (NMR) is a phenomenon that describes the behaviour of nuclei in an external magnetic field, and that is subsequently disturbed by a weaker, oscillating magnetic field. Nuclei have a fundamental property referred to as spin, which is primarily determined by the number of unpaired nucleons. Spin is associated with an angular momentum and a nuclear magnetic dipole moment. The nuclear magnetic dipole moment, μ, is equal to:

$$\mu = \gamma \frac{h}{2\pi} I \qquad\qquad \textbf{1.1}$$

Here γ is the gyromagnetic ratio, h is Planck's constant, and I is the spin quantum number. I can have integer-or half-integer values and is ½ for hydrogen (^{1}H), which is the most common nuclei used in NMR and MRI.

In the absence of an external magnetic field, $\vec{B}_0$, the individual nuclear magnetic dipole moment in diamagnetic matter is usually randomly distributed. When an external magnetic field is introduced, it interacts with the magnetic moment of a nucleus. In a simplified view, this process is characterized by energy states aligning either parallel (low-energy) or anti-parallel (high-energy) with $\vec{B}_0$, with a preference for the lower energy state aligned parallel with the external field. The number of nuclei in each energy state is described by the Boltzmann distribution:

$$\frac{N_-}{N_+} = e^{-(\frac{\Delta E}{kT})} \qquad\qquad \textbf{1.2}$$

Here N_- and N_+ are the number of nuclei in the low and high energy states, respectively, ΔE is the energy difference, T is the absolute temperature, and k is the Boltzmann constant (1.38×10^{-23} J/Kelvin). At body temperature, only ~1/100,000 ^{1}H nuclei contribute to the NMR signal at 1.5 T [176]. This small polarization of nuclei produces a mean magnetic moment that aligns parallel with $\vec{B}_0$, known as the net magnetization, $\vec{M}_0$.

When placed in an external magnetic field, the individual dipole moments create a torque as they interact with the magnetic field, inducing the individual dipole moments to precess about the $\vec{B}_0$ at an angular frequency known as the Larmor frequency, ω_0:

$$\omega_0 = \gamma B_0 \qquad\qquad \textbf{1.3}$$

Here γ is the gyromagnetic ratio of the nuclei and B_0 is the magnitude of the external magnetic field strength [177]. As previously mentioned, ^{1}H is often the nucleus of interest due to its large abundance in the human body (99.8%) and presence in most organic compounds, producing the greatest signal [178]. The electrons of ^{1}H do not contribute to magnetic resonance, resulting in ^{1}H being referred to as the proton [177]. The gyromagnetic ratio of ^{1}H is 2.675×10^8 s^{-1}T^{-1} (Figure 1.5).
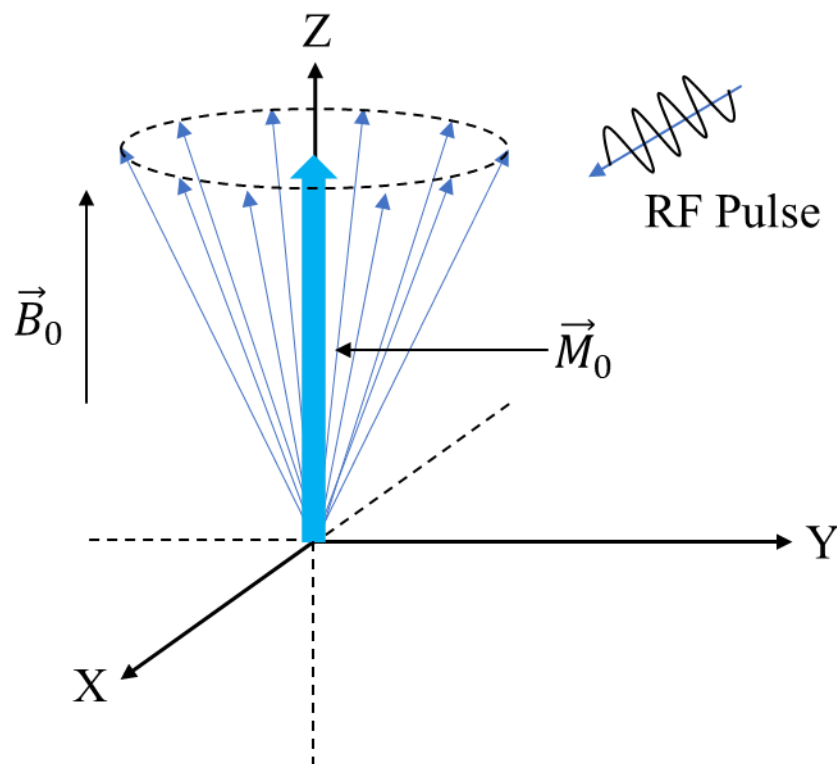
Figure 1.5. A simplified representation of the net magnetization vector, $\vec{M}_0$, in the presence of an external magnetic field, $\vec{B}_0$.

1.5.2 NMR Signal

Although quantum mechanics governs the behaviour of each nucleus, classical mechanics may be used to describe the mean magnetic moment of the nuclei. Since the nuclei composing $\vec{M}_0$ are uniformly distributed around $\vec{B}_0$ and $\vec{M}_0$ is not creating any net flux, it is undetectable when aligned along the same axis as $\vec{B}_0$. Consequently, to make a measurement, the individual nuclei must gain phase coherence as $\vec{M}_0$ is titled away from the main magnetic field by an external pulse referred to as the radiofrequency (RF) pulse, which oscillates at the Larmor frequency of the nuclei of choice. The RF pulse is applied perpendicular to the main magnetic field, producing a weaker magnetic field perpendicular to $\vec{B}_0$ in the rotating frame of reference, which is known as $\vec{B}_1$ [177]. The excitation pulse is called an RF pulse because Larmor frequencies are typically in the MHz range, corresponding to the electromagnetic spectrum's RF range [176]. The RF

pulse also promotes the nuclei to adopt a higher energy state and to align in orientation due to phase coherence [177]. In the presence of the RF pulse, $\vec{M}_0$ is tipped such that a portion of $\vec{M}_0$ is perpendicular to $\vec{B}_0$ in the transverse plane, which is the plane perpendicular to the external magnetic field, and then experiences nutation about the resultant $\vec{B}_1$ field [179]. The tip or flip angle, α of the magnetic moment is determined by the duration and amplitude of the RF pulse [178]. In simple experiments, α is 90° to achieve the maximum value of $\vec{M}_0$ in the transverse plane while an α of 180° would result in the $\vec{M}_0$ to align with $-\vec{B}_0$ [178].

When tipped away from $\vec{B}_0$, the magnetization can be viewed as two separate components: longitudinal and transverse. Longitudinal magnetization describes the magnetization component parallel to $\vec{B}_0$ and is represented as a vector in the z-direction, $\vec{M}_z$ in a Cartesian coordinate system. Transverse magnetization is the magnetization component in the transverse (i.e., x-y) plane and is represented by $\vec{M}_{xy}$ [178]. The following equations describe the longitudinal and transverse components of the net magnetization at equilibrium just prior to the RF pulse, respectively:

$$\vec{M}_z = \vec{M}_0 \cos \alpha \qquad\qquad \textbf{1.4}$$

$$\vec{M}_{xy} = \vec{M}_0 \sin \alpha \, e^{i(\omega_0 t + \phi)} \qquad\qquad \textbf{1.5}$$

Here ϕ describes the phase shift or the initial angular position of the magnetic moment in the transverse plane [178].

When the magnetization is tipped into the transverse plane after the application of the RF pulse, the comprising nuclei radiate electromagnetic energy because of the change in the magnetic field (Faraday's law of induction) [180]. This energy is detected as an induced voltage by receive coils, which is then amplified and used to form the signal [178]. The receive coils only detect signal from $\vec{M}_{xy}$ as it is perpendicular to $\vec{B}_0$. The produced voltage is proportional to the NMR signal and the square of the magnetic field strength of $\vec{B}_0$ [177].

1.5.3 Creating the MR Image

As previously mentioned, the MR signal is a result of Faraday's law, as it is essentially a small electric current that is induced in the receiver coil by the precession of $\vec{M}_0$. The signal is called free induction decay (FID) and is generated by a single RF pulse [177]. The FID can be manipulated to generate an echo, which involves refocusing the nuclei of the net magnetization after the initial RF pulse. There are two types of echoes: spin echo (SE) and gradient recalled echo (GRE).

Discovered by Erwin Hahn in 1949, the spin echo is generated by using two successive RF pulses, usually with an a of 90° and 180°, respectively [181]. The excitation RF pulse, typically 90°, first tips the $\vec{M}_0$ into the transverse plane, generating the FID. Due to differences in the local microscopic field, some nuclei might precess and gain phase faster or slower than others. After a short period of delay where some of the transverse magnetization has been dephased, a refocusing RF pulse, typically 180°, is applied, flipping all the nuclei in the transverse plane. Because of the 'flip,' all the nuclei that were dephased due to the local field inhomogeneities rephase, generating the spin echo (SE).

Unlike the SE, where an RF pulse is used to rephase the magnetization to generate the echo, a gradient is used to refocus the phase of the nuclei to generate the GRE; gradients will be discussed in 1.5.3.1. After applying the RF pulse and generating the FID, a negative gradient lobe is applied immediately to cause a phase dispersion of the nuclei, dephasing the magnetization. This is followed by employing a positive gradient lobe equal in magnitude to refocus the nuclei and generate the GRE. It is important to note that only the nuclei that are initially dephased by the gradient are the ones that are refocused by the gradient reversal.

Both SE and GRE can also consist of spoiling, which is the disruption of any residual transverse magnetization that may persist between RF pulses. In other words, spoiling ensures that the $\vec{M}_0$ has no transverse components before each RF pulse, resulting in no

transverse steady-state being established. Spoiling can be achieved through long TR, RF spoiling, or gradient spoiling [182, 183].

The signal produced by echoes depends on the concentration of nuclei, intrinsic relaxation properties of the tissue being imaged (discussed in 1.5.5), and echo time (TE). TE is the time between the middle of the first RF pulse and the peak of the echo. The time between the application of the two RF pulses is the repetition time (TR) [177, 181].

1.5.3.1 Gradients

First used in 1952 by Herman Carr and further developed by Lauterbur and Mansfield to distinguish signals from different tissues, magnetic field gradients are linear magnetic fields whose strength changes based on position and are often applied along an axis to encode a nuclei's location [176, 178]. Since $\vec{B}_0$ cannot be changed, smaller magnetic fields can be added to perturb the magnetic field, which is accomplished using magnetic gradients. By adding a gradient, nuclei along the axis of the applied gradient experience marginally different magnetic fields based on their position, causing them to precess faster or slower than the Larmor frequency. Gradients can be applied along the x, y, or z-direction and are approximately 1% of the strength of $\vec{B}_0$ at clinical field strengths, resulting in small perturbations. The following equation describes the angular frequency, ω_0, of a nucleus as a function of gradient strength:

$$\omega_0(r) = -\frac{\gamma}{2\pi}\left(\vec{B}_0 + G_r \cdot r\right) \qquad \textbf{1.6}$$

Here G_r is the strength of the gradient, and r is the location of the nuclei as described by x, y, or z.

Three orthogonal, linear gradients are typically needed along the x-, y-, and z-direction to determine the spatial localization of the MR signal [177]. Since gradients are vectors – they have both magnitude and direction – a combination of magnetic field gradients can be applied along any direction [176]. Gradient coils are found inside the scanner's bore and produce gradient fields [177]. The following paragraphs will discuss three necessary

gradients for slice selection and determining the position of selected nuclei in an ideal setting: slice selection, frequency encoding, and phase encoding.

Slice selection is the selective excitation of specific anatomical planes to isolate signals from that particular slice [178]. The slice selection gradient, which can be applied along any direction – axial, coronal, oblique, or sagittal – causes the nuclei along its axis to precess at different frequencies [177]. An RF pulse with a bandwidth of frequencies that correspond to the nuclei within the slice is transmitted. Once the RF is applied and the slice selection gradient removed, only the nuclei within the selected slice experience transverse magnetization, while the nuclei outside the slice remain aligned with $\vec{B}_0$ [176]. Consequently, signal from only that slice is acquired. To avoid signal loss, a refocusing gradient equal and opposite in amplitude to the slice selection gradient is used to bring nuclei back into phase with each other [178]. The slice's width and location depend on the gradient strength and the RF pulse bandwidth [176].

Once a slice has been excited, the next step is to spatially encode the nuclei within the slice in directions that are orthogonal to the direction of the slice select gradient. Spatial encoding can be separated into frequency and phase encoding. According to convention, slice selection is conducted along the z-axis, while frequency and phase encoding is along the x-axis and y-axis, respectively [178].

The frequency encoding gradient, also known as the readout gradient, causes the resonant frequency of the nuclei along the x-axis to vary linearly [177, 178]. The gradient is continuously applied while the MR signal is being collected; hence, the signal is "frequency encoded" in the x-direction [177]. For a single RF pulse, all the spatial frequencies comprising the signal can be collected in real-time as the signal can be decomposed using the Fourier Transform to represent a 1D projection of the sample [177]; the Fourier Transform will be discussed in 1.5.4.

The phase encoding gradient is applied along the y-axis and as indicated by the name, involves manipulating the phase of the nuclei. Unlike frequency encoding, phase encoding does not occur during acquisition but is turned on for a short time to allow the nuclei to accumulate a positionally varying phase shift [177]. In practice, the phase

encoding gradient is turned on first to allow the nuclei to accumulate the change in phase before generating the echo [177]. Once the phase encoding gradient is turned off, the frequency encoding gradient can be turned on, causing the nuclei to precess at the Larmor frequency while retaining their accumulated phase shift; hence, the nuclei are now "phase-encoded" [178].

It is important to note that only the sum of all phase shifts for each frequency is measured from a single excitation; hence, multiple and separate phase encoding gradients must be employed over multiple excitations to distinguish signals along the phase encoding direction. The resultant data points correspond to different strengths of the MR signal over a range of gradient moments. Like with frequency encoding, an inverse Fourier Transform can disentangle individual phase contributions where each phase component corresponds to a different spatial position along the y-axis. The MR sequence must be repeated with a different phase-encoding gradient until all possible spatial frequencies have been sampled; this corresponds to the number of rows of pixels in the image. The total scan time of a sequence equals TR multiplied by the number of signal averages and phase-encoding steps [177]. Signal averaging is done by repeating measurements under similar conditions to increase the signal-to-noise ratio by adding random noise [177]. A pulse sequence diagram of a spoiled GRE is shown in Figure 1.6.
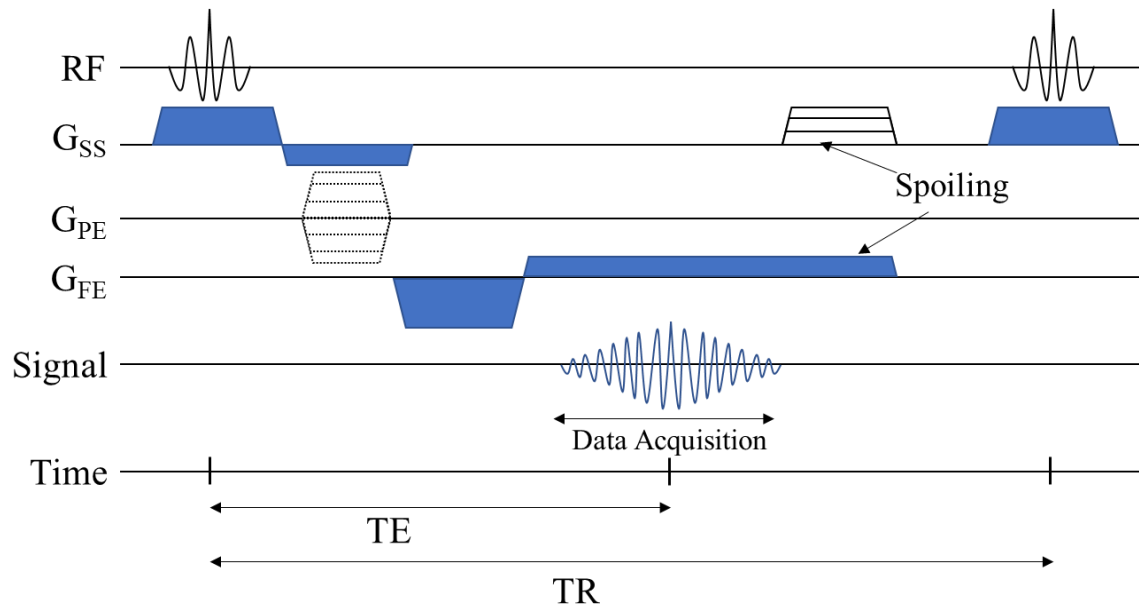
Figure 1.6. An example of a spoiled gradient echo pulse sequence diagram showing the slice selection (G_{SS}), phase encoding (G_{PE}), and frequency encoding (G_{FE}) gradients at work to encode the spatial location of the gradient echo. Spoiling of the transverse magnetization is achieved by G_{SS} and G_{FE} prior to the application of the second radiofrequency pulse.

1.5.4   Fourier Transform

Once the raw data matrix is acquired, it needs to be converted to an image by an inverse Fourier Transform (FT). All signals can be represented as a combination of sinusoidal waves where each sine and cosine wave refers to a particular signal frequency, phase, and amplitude. Thus, the FT is a mathematical tool that decomposes a complicated signal into the frequencies and relative amplitudes of its simple component waves [184].

In the MR context, the complicated signal is the echo that needs to be decomposed because it contains all the necessary frequency- and phase-encoded information required to construct the image. The FT separates the individual frequency and phase contributions, where each frequency and phase contributes to a different spatial position along the x-axis and y-axis, respectively. The signal is then entered into k-space, a 2D Fourier space that organizes spatial frequency and amplitude information. The dominant

method of filling k-space is the Cartesian method, where each line of data in k-space refers to the signal obtained from a single application of the phase-encoding level [185, 186]. The outer rows of the k-space correspond to high-order phase-encodings and high spatial frequencies that contribute to image resolution; the inner rows correspond to low-order phase-encodings and low spatial frequencies that provide information on the general contrast of the image [185, 186]. A 2D inverse FT of the entirety of k-space creates the MR image [187].

The MR raw data is complex and contains real and imaginary components [178]. These components can be reconstructed as real, imaginary, magnitude, and phase images. Clinically, magnitude images can be used for diagnostic purposes, while phase images are generated for flow depiction and identification of regions of $\vec{B}_0$ inhomogeneity [178].

1.5.5　Relaxation

Once the RF pulse is removed, the magnetic moments of the nuclei immediately begin to align parallel with $\vec{B}_0$ as the magnetization recovers to equilibrium [179]. This process is referred to as relaxation and, like $\vec{M}_0$, can be classified into two components: longitudinal and transverse. Longitudinal relaxation, or T_1, describes the re-growth of $\vec{M}_z$ while transverse relaxation, or T_2, describes the loss of phase coherence of $\vec{M}_{xy}$.

1.5.5.1　Longitudinal Relaxation

Longitudinal or T_1 relaxation describes the time it takes $\vec{M}_z$ to recover approximately 63% or $\left(1 - \frac{1}{e}\right)$ of $\vec{M}_0$ following a 90° pulse (Figure 1.7). This relaxation is a result of the nuclei "releasing" the extra energy received from the RF pulse to the surrounding "lattice" or environment as they transition back to their thermal equilibrium and low energy state [178]. This release of energy occurs when the local magnetic field is fluctuated by other nuclei and/or molecules that are fluctuating near the Larmor frequency [188]. Consequently, T_1 is also known as the spin-lattice time constant and is dependent on the proximity of the nuclei to other nuclei and molecules, which varies among tissues and pathological states [177, 178, 188].

Once the RF pulse is removed, $\vec{M}_z$ displays a logarithmic growth process to $\vec{M}_0$:

$$\vec{M}_z = \vec{M}_0 \left(1 - e^{\frac{-t}{T_1}}\right) + \vec{M}_0 \cos \alpha \, e^{\frac{-t}{T_1}} \qquad\qquad \textbf{1.7}$$

where t is the time, and α is the flip angle [178]. For ^{1}H in human tissue, T_1 ranges from hundreds to thousands of milliseconds over the magnetic field strengths of interest [189].
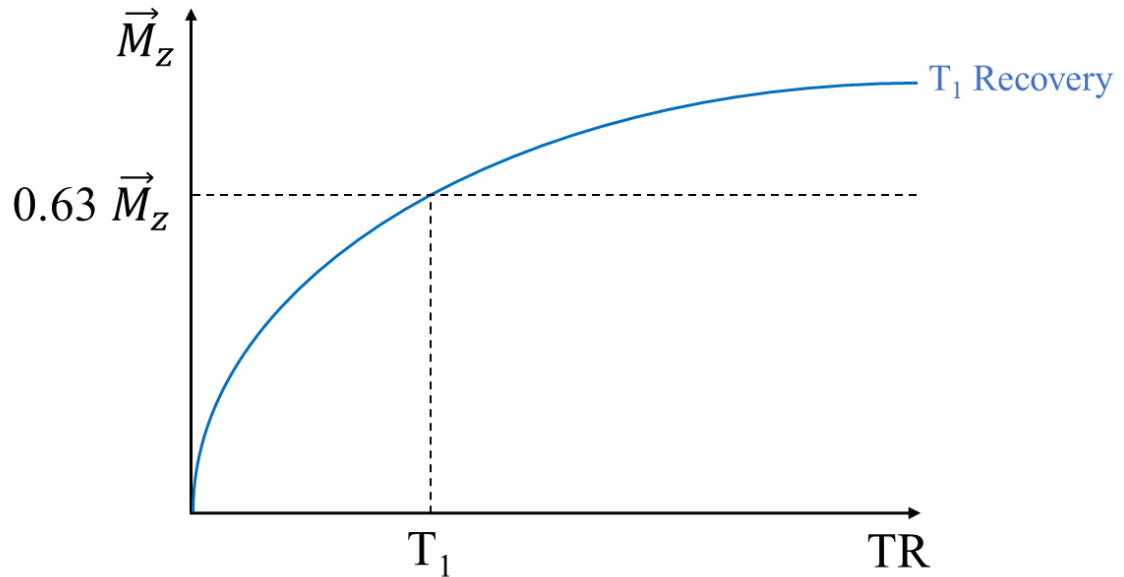
Figure 1.7. A graphical representation of the longitudinal (T_1) relaxation curve. At T_1, the longitudinal magnetization of a tissue reaches approximately 63% of its maximum value.

1.5.5.2 Transverse Relaxation

Transverse or T_2 relaxation describes the time it takes $\vec{M}_{xy}$ to decay to approximately 37% or $\left(\frac{1}{e}\right)$ of $\vec{M}_0$ (Figure 1.8). In other words, T_2 is the signal decay time constant in a homogeneous magnetic field [178]. The nuclei contributing to $\vec{M}_{xy}$ experience local fields, which are combinations of the applied field and their neighbours' fields. Since variations in the local fields lead to different local precession frequencies, the individual nuclei lose phase coherence, resulting $\vec{M}_{xy}$ to exponentially decay to zero [178]. Hence, T_2 is referred to as the spin-spin time constant since it describes the relaxation due to

magnetic fields caused by neighbouring nuclei or "spins" and interactions with other molecules [188].

Once the RF pulse is removed, the transverse magnetization displays an exponential decay process:

$$\vec{M}_{xy} = \vec{M}_0 \sin \alpha e^{i(\omega_0 t + \phi)} \, e^{\frac{-t}{T_2}} \qquad\qquad \textbf{1.8}$$

Here t is the time. T_2 ranges from tens of microseconds to seconds for ^{1}H in human tissue over the magnetic field strengths of interest. Like T_1, T_2 values are short for solids – order of milliseconds – and long for liquids – order of seconds [189].
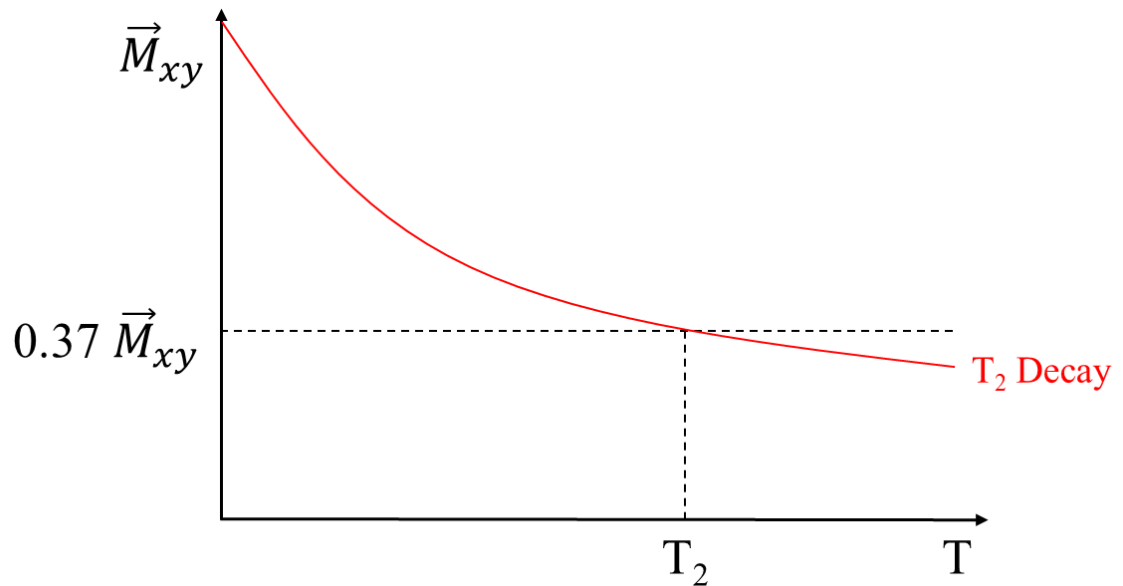
Figure 1.8. A graphical representation of the transverse (T_2) relaxation curve. At T_2, the transverse magnetization of a tissue decays to approximately 37% of its initial value.

Any process that results in T_1 relaxation also results in T_2 relaxation, but not every process that results in T_2 relaxation results in T_1 relaxation. If the energy exchange occurred between a nucleus contributing to $\vec{M}_{xy}$ and its environment, this would result in both T_1 and T_2 relaxation as the nucleus releases energy and dephases. On the other hand, some processes that affect T_2 relaxation are secular in the sense that they do not affect T_1 relaxation, such as nuclei "flip-flops" where a pair of nuclei exchange their longitudinal

angular momentum, causing a loss in T_2 relaxation but no net change in T_1 [188]. Thus, the T_1 relaxation of tissue is always longer or equal to its T_2 relaxation.

1.5.5.3   Apparent Transverse Relaxation

As previously mentioned, T_2 describes the signal decay rate caused by atomic and molecular interactions in a homogenous magnetic field [178]; however, the magnetic field is not always homogenous, and this inhomogeneity can also result in the dephasing of nuclei. This inhomogeneity could be due to intrinsic defects in the magnet itself or from susceptibility-inducing materials within the tissue that distort the magnetic field, such as iron [190]. As a result, the signal decays faster since nuclei experience phase incoherence and transverse relaxation at a faster rate. The observed or apparent transverse relaxation is referred to as $T_2{}^*$ and is described by the following equation:

$$\frac{1}{T_2^*} = \frac{1}{T_2} + \frac{1}{T_2'}$$

1.9

Here T_2' is the relaxation time from the inhomogeneities (Figure 1.9) [190].
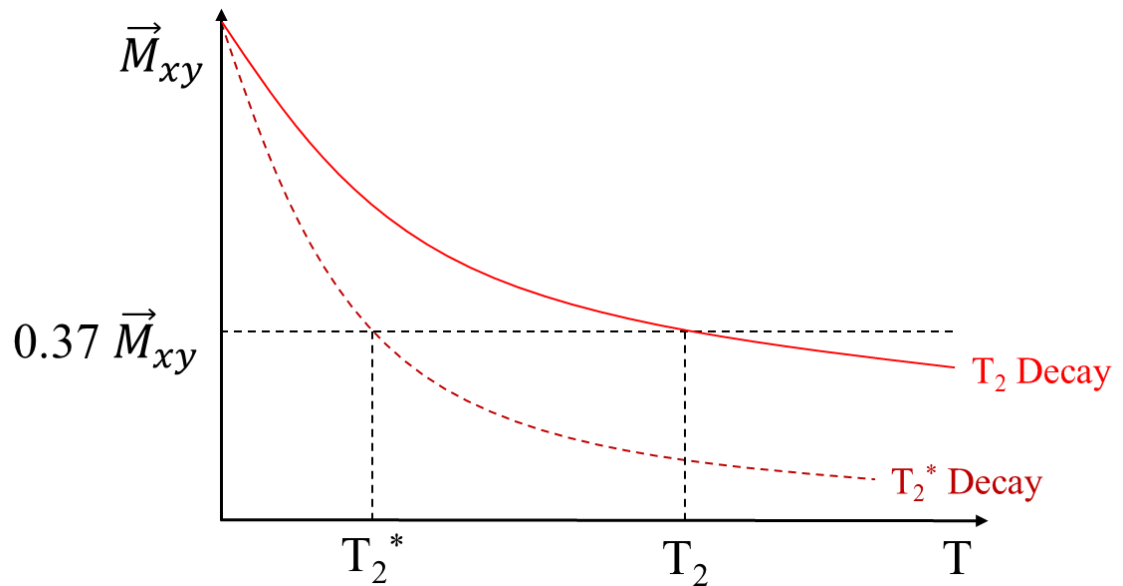
Figure 1.9. A graphical representation of the observed transverse (T_2) and apparent transverse (T_2^*) relaxation curves in light red and dark red, respectively.

1.5.5.4   Biophysical Basis of Relaxation

Relaxation is essentially due to molecular motion, interaction, and energy exchange between molecules and nuclei [188]. Consequently, tissue's T_1 and T_2 relaxations are directly affected by its biophysical structure and biochemical environment. The structural and environmental factors involve tissue water content and mobility, the presence of paramagnetic atoms (e.g., iron), and lipid, protein, and macromolecule composition. Hence, T_1 and T_2 can provide information on tissue structure and environment.

Changes in T_1 and T_2 can also reflect tissue changes due to normal biological processes, such as neurodevelopment, neuroplasticity, and aging [191, 192]. For instance, neurodevelopmental changes such as myelination, axonal growth, and gyrification can alter tissue structure, environment, and, hence, T_1 and T_2. WM has a shorter T_1 and T_2 than GM due to the following composition factors: iron-containing oligodendrocytes, lipid bilayer myelin sheath and associated proteins, glial cells, and reduced free WM content [191]. Similarly, the T_1, T_2, and T_2^* variations observed between deep GM

structures are due to differing iron concentrations [193, 194]. Along with normal biological processes, disease and pathology, such as demyelination, iron accumulation due to beta-amyloid plaques in Alzheimer's disease, tumour infiltration, and edema, can also result in structural and biochemical changes and, hence, T_1, T_2, and T_2^* relaxations [195-199].

1.5.6   Sources of Image Contrast

The different T_1, T_2, and T_2^* relaxation times of tissues can be exploited to generate contrast or weighting [177]. Of these relaxation times, T_1 and T_2 are the most used sources of contrast in conventional MRI, along with proton density (PD), which represents the apparent concentration of ^{1}H in each voxel [200]. T_1-weighted images display high intensity in tissues with short T_1 since T_1 is inversely proportional to signal intensity. On the other hand, T_2- and PD-weighted images display high intensity in tissues with long T_2 and in areas of high proton density, respectively, since both are directly proportional to signal intensity [177]. To generate the desired contrast or weighted image, pulse sequence parameters – TR, TE, and α – need to be manipulated as described in Table 1.1. TR and α control T_1-weighting while TE controls T_2- and T_2^*- weighting (Table 1.1). It is important to note that although the image may have a dominant weighting, the signal in the image is always a mixture of all the underlying tissue-dependent contrasts [177].

Table 1.1. Imaging weighting of spin echo and gradient echo sequences as determined by TR, TE, and α.

Spin Echo	Short TE	Long TE
Short TR	T_1-weighted	N/A
Long TR	PD-weighted	T_2-weighted
Gradient Echo	Short TE	Long TE
Small α	PD-weighted	T_2-weighted
Large α	T_1-weighted	N/A

1.5.7   Relaxometry

Conventional MRI uses T_1- and T_2-weighted images where tissues' T_1 and T_2 relaxation times generate contrast, allowing visualization of differences between tissue anatomy and assessment of anatomy and pathology [172]. Although these images provide clinically useful tissue contrast, comparing these images across time and between subjects and subsequent physiological interpretation of these images can be challenging because the signal values in these images are affected by MR hardware and software [196]. In contrast, T_1 and T_2 relaxation times are quantitative MR parameters that reflect fundamental tissue properties sensitive to the tissue environment, such as water content, magnetization exchange, and paramagnetic content [188]. Since these parameters are independent of imaging protocol, quantifying these parameters allows for comparing these values longitudinally and cross-sectionally.

1.5.7.1   Methods for T_1 and T_2 Mapping

The gold standard approaches for T_1 and T_2 relaxometry are inversion recovery (IR) and multiple echo-time SE, respectively; however, these methods have lengthy acquisition times, making them unsuitable for fetal imaging [197, 201]. Nonetheless, the desire to study tissue development pathology using quantitative T_1 and T_2 values has resulted in the development of multiple rapid mapping approaches.

For T_1 mapping, IR first involves inverting the magnetization by a 180° RF pulse, followed by a conventional SE sequence (90° RF pulse – 180° RF pulse). By initially inverting the magnetization, T_1 relaxation occurs as the magnetization is re-established along $+B_0$ during the time between the first 180° and 90° RF pulses. By the time the SE is generated, the various tissue magnetizations can be distinguished based on their different T_1 relaxation times, allowing the different T_1s to be quantified from the T_1 recovery curve [197]. An alternative to IR and one of the most efficient methods of T_1 mapping is Look and Locker [202]. Instead of fully recovering the magnetization to make a single measurement, the Look-Locker technique continuously samples the recovering magnetization with rapidly applied small-angle RF pulses. Hence, T_1 can be measured from the rate of change of signal amplitudes of the recovery curve [202]. Although faster than IR, Look-Locker does not measure "true" T_1 but rather an apparent T_1 or T_1^* that is shorter due to the method's dependency on various factors, such as pulse sequence, TR, tissue T_2, and field strength [192].

Another T_1 mapping technique is the driven equilibrium single pulse observation of T_1 (DESPOT$_1$) [203]. DESPOT$_1$ involves collecting spoiled gradient recalled echo (SPGR) images at different flip angles while the TR is held constant. Since T_2 effects are limited by spoiling the transverse magnetization, a signal intensity curve characterized only by T_1 and proton density can be generated, from which T_1 can be quantified. Christensen *et al.* first proposed using the method to characterize T_1, which has been subsequently refined and optimized by numerous other groups, most notably by Deoni *et al.* [203-209].

Like the variable flip angle method for T_1, variable flip angle fully balanced steady-state free precession (bSSFP) acquisitions can also allow the calculation of T_2 [210]. With constant TR and TE, the bSSFP signal curve depends on T_1, proton density, and T_2. If T_1 is known, T_2 can be calculated [209]; however, the mixed contribution of T_1 and T_2 to the bSSFP signal also provides an opportunity for their combined calculation. With the addition of an inversion pulse to increase the T_1 dependence, a sequence analogous to the Look-Locker approach is obtained [211, 212]. The signal is then driven back to an altered equilibrium via an apparent T_1, T_1^*, related to the true T_1 and T_2. From the relationship,

both T_1 and T_2 may be estimated; this variable flip angle methodology is known as driven equilibrium single pulse observation of T_2 (DESPOT$_2$) [209].

1.5.7.1.1   DESPOT$_1$

DESPOT$_1$ uses SPGR as the sequence of choice because its major use is to generate T_1-weighted images, as the pulse sequence is specifically designed to disrupt transverse coherences [213]. The measured SPGR signal intensity is dependent on T_1, TR, TE, T_2^*, α, and a factor which is proportional to $\vec{M}_0$:

$$S_{SPGR} \propto \frac{M_0 \left(1 - e^{\frac{-TR}{T_1}} \right) sin\alpha}{1 - e^{\frac{-TR}{T_1}} cos\alpha} e^{\frac{-TE}{T_2^*}} \qquad \textbf{1.10}$$

It is important to note that signal dependence is on T_2^* instead of T_2 because the echo is formed by gradient refocusing of the FID as opposed to the formation of a spin echo [213]. By using a short TE to minimize T_2^* contributions to the signal, the data can be represented in linear form and, hence, resulting in the following linear equation:

$$\frac{S_{SPGR}}{sin\alpha} \propto e^{\frac{-TR}{T_1}} \left(\frac{S_{SPGR}}{tan\alpha} \right) + M_0 \left(1 - e^{\frac{-TR}{T_1}} \right) \qquad \textbf{1.11}$$

By keeping TR constant and changing the flip angle between acquisitions, a signal curve characterized by T_1 is generated. Since the data can be represented in linear form, as shown above, the slope (m) can be determined using linear regression, allowing T_1 to be extracted [209].

$$T_1 = \frac{-TR}{\ln(m)} \qquad \textbf{1.12}$$

1.5.7.1.2   DESPOT$_2$

DESPOT2 uses the bSSFP sequence, which involves the repeated application of excitation pulses with varying flip angles at a TR much less than either T_1 or T_2. The idealized bSSFP signal intensity depends on T_1, T_2, TR, α, and $\vec{M}_0$.

$$S_{bSSFP} \propto \frac{M_0 \left(1 - e^{\frac{-TR}{T_1}} \right) \sin\alpha}{1 - e^{\frac{-TR}{T_1}} e^{\frac{-TR}{T_2}} - (e^{\frac{-TR}{T_1}} - e^{\frac{-TR}{T_2}}) \cos\alpha} \qquad \textbf{1.13}$$

Like the SPGR signal equation, the data can be represented in linear form, resulting in the following linear equation:

$$\frac{S_{bSSFP}}{\sin\alpha} \propto \frac{e^{\frac{-TR}{T_1}} - e^{\frac{-TR}{T_2}}}{1 - e^{\frac{-TR}{T_1}} e^{\frac{-TR}{T_2}}} \left(\frac{S_{SPGR}}{\tan\alpha} \right) + \frac{M_0 \left(1 - e^{\frac{-TR}{T_1}} \right)}{1 - e^{\frac{-TR}{T_1}} e^{\frac{-TR}{T_2}}} \qquad \textbf{1.14}$$

Like DESPOT1, keeping TR constant and changing the flip angle between acquisitions generates a signal curve dependent on both T_1 and T_2. Since T_1 is already known from DESPOT1, the slope (m) can be determined using linear regression, allowing T_2 to be extracted [209].

$$T_2 = \frac{-TR}{\ln \left(\frac{m - e^{\frac{-TR}{T_1}}}{m e^{\frac{-TR}{T_1}} - 1} \right)} \qquad \textbf{1.15}$$

It is important to note that bSSFP is sensitive to local off-resonance frequencies and magnetic field inhomogeneities due to gradient refocusing to preserve the transverse magnetization between TR cycles. As a result, bSSFP images often contain banding artifacts, which are areas of low signal intensity corresponding to specific values of off-resonance frequency. Two bSSFP volumes are acquired for each flip angle to resolve the artifact: one at a phase increment of $0°$ and a second at $180°$. The variation between the two acquisitions produces banding artifacts that are spatially offset, with the difference between the two-phase offsets amounting to an off-resonance map. The off-resonance map is then used to correct the banding artifact between the volumes at varying phase increments [210, 214-216].

1.5.8 Myelin Imaging with MRI

Due to current technological limitations, conventional MRI cannot visualize the rapidly decaying signal from the larger, non-aqueous molecules from the CNS. Hence, conventional MRI cannot directly image myelin because the signal from the non-aqueous components – lipids and proteins – of myelin decays to zero in approximately 50 to 100 µs [133]. A specialized technique known as ultra-short echo-time was developed to directly image the non-aqueous ^{1}H nuclei of the myelin lipid bilayer [217, 218]. This technique involves suppressing the longer signals, usually with an adiabatic inversion pulse, to image the rapidly decaying signals with extremely short TE [219]. Unfortunately, the acquisition times of these sequences are not feasible for fetal imaging.

Another MR-based method for myelin imaging is magnetization transfer (MT), which involves imaging the macromolecular content of the myelin sheath. MT originates from the magnetization and proton exchange between macromolecules and free water, which, in this case, are the myelin lipids and proteins, and the surrounding water, respectively. Although the exchange between myelin and the surrounding water induces a larger MT contrast as the MT effects of myelin are 2-3 times higher, MT-weighted images can be biased by inhomogeneities in the magnetic field and influenced by non-myelin macromolecules [220, 221]. Furthermore, the MT ratio, which is the semi-quantitative measure of MT, is dependent on acquisition parameters, such as shape, frequency offset, amplitude, and duration of the MT pulse, potentially resulting in changes independent of the myelin macromolecular content [222]. Although other advanced MT techniques exist to better assess myelin content, such as quantitative MT and inhomogeneous MT, these measures still have issues, such as imperfect modelling and low myelin sensitivity [223, 224]. Both fractional anisotropy and radial diffusivity of diffusion tensor imaging have also been suggested as markers for myelin; however, there are issues with both. For instance, fractional anisotropy can be influenced by non-myelin origins, such as fiber dispersion, while the myelin-related changes seen in radial diffusivity are likely due to simple fiber geometry seen in animals and not in humans [225-227].

Although the signal from myelin lipid decays rapidly, the MR signal from the aqueous components of myelin decays on the order of milliseconds and, hence, is accessible by MRI [133]. Therefore, myelin structure and pathology can be investigated by studying the MRI-visible water associated with myelin, naming this technique myelin water imaging.

1.5.8.1   Myelin Water Imaging

Myelin water imaging (MWI) is based on the fact that while the entire MR signal is from the protons from the aqueous components of myelin, individual water molecules can experience very different microscopic environments, depending on their physical location. Hence, the signal from the individual aqueous components of myelin can be identified and separated with signal amplitudes proportional to the relative amounts of water in each environment, contingent on the fact that the total MR signal comes from water in different non-exchanging environments. The main aqueous compartments of myelin in the brain are myelin water (MW) and intra-/extra-cellular water (IEW). MW is the protons trapped between the lipid myelin bilayers, while the IEW refers to the protons found in the intra-axonal space and extra-cellular space (interstitial space outside of white matter fibres). Myelin water fraction (MWF) is the quantitative measure of MWI and is defined as the ratio of signal from myelin water protons to the sum signal from all protons from MW and IEW throughout the voxel (Figure 1.10) [114, 228].
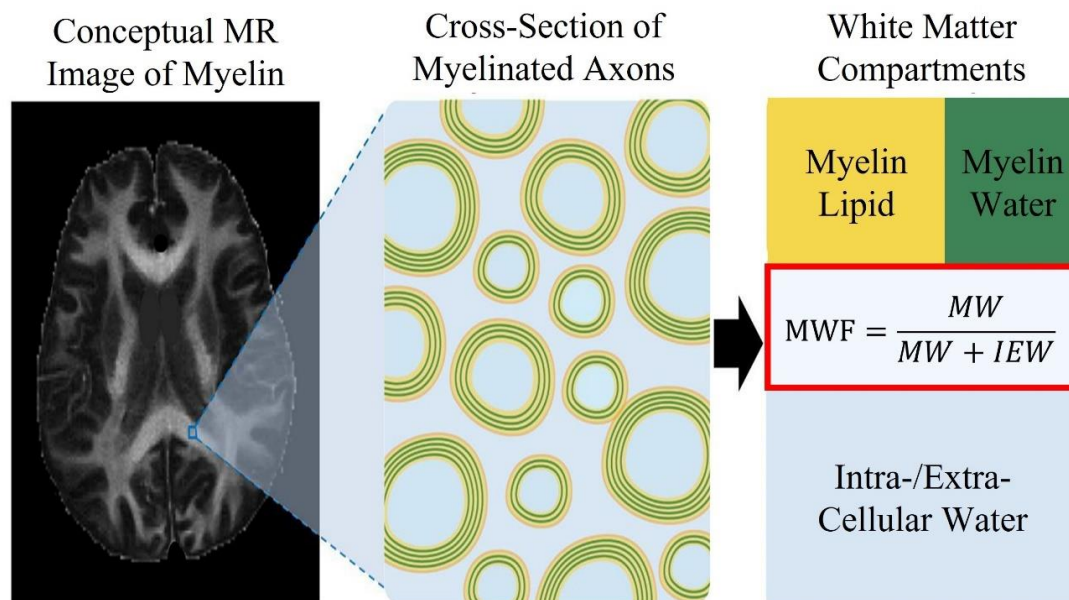
Figure 1.10. Breakdown of the myelin sheath compartments involved in myelin water imaging and the quantification of myelin water fraction. This figure was adapted with permission from Lee *et al.* J Magn Reason Imaging 2020.

An extension of relaxometry, MWI utilizes the different water components' T_1 and T_2 relaxation times individually or together to quantify myelin. There are four approaches to MWI: T_2-based, T_2^*-based, T_1-based, and steady-state-based.

T_2-based MWI is the traditional technique for MWI. This technique uses the short T_2 of myelin water to separate its signal from that of IEW [114]. At 3 T, the T_2 of myelin water is approximately 20 ms, while the T_2 of IEW is approximately 80 ms. This technique acquires a T_2 decay curve with contributions from myelin water and IEW signals to generate a distribution that distinguishes the signal contribution of each T_2 compartment. For data acquisition, a multi-echo SE sequence consisting of a 90° RF pulse followed by a series of 180° RF pulses with signal measures at the interleaved TEs typically measured over 32 echoes is used [114, 229, 230]. To generate a T_2 distribution from the multi-echo data, the fitting of multiple exponential functions with a stimulated echo correction needs to be applied [229, 231]. Since exponential functions are not mathematically orthogonal and cannot be easily distinguished, the fitting is noise-sensitive [229, 231]. The acquisition times of this technique also tend to be long.

T_2^*-based MWI is similar to the T_2 technique in that it exploits the T_2^* difference between myelin water & IEW [232]. The T_2^* model has been revised to improve MWF estimation by including the frequency shift caused by the magnetic susceptibility of myelin. This technique uses a multi-echo GRE sequence to obtain signal decay and frequency shift [233]. This technique has some challenges, such as the high sensitivity of the GRE to $\vec{B}_0$ inhomogeneity and stability, and is not widely available as it is still relatively new [234-236].

Like T_2, T_1-based MWI exploits the difference in T_1 of myelin water and IEW. At 3 T, the T_1 of myelin water is less than 400 ms, while the T_1 of IEW is approximately 800 ms [237]. This technique can use either multiple IR data to generate a T_1 relaxogram, which requires a long scan time, or an inversion RF pulse to suppress non-myelin water signals and, therefore, acquire myelin water signal only [230, 237-239]. The latter has challenges, such as the RF suppression partially suppressing myelin water signal, leading to the MWF acquired from this sequence to be referred to as apparent MWF [240].

The final technique for MWI is steady-state-based and is known as multicomponent driven equilibrium single pulse observation of T_1 and T_2 (mcDESPOT). mcDESPOT involves acquiring multiple steady-state images of varying flip angles, then fitting the data to a multiple-compartment model to estimate each compartment's T_1, T_2, and additional parameters [241]. The total acquisition time for this method is reasonable and has been applied in various applications and demographics, such as adults, children, and neonates [114, 242, 243]. mcDESPOT is a direct and specific method for measuring myelin and was chosen to measure MWF in the fetal brain.

Factors affecting the specificity of MWI include myelin debris, intra-myelinic edema, change in total water content unrelated to myelin, and inter-compartmental water exchange [244-249]. Despite the potential confounds, MWF has been validated to be a strong marker for myelin by MBP immunohistochemistry and LFB (133,244), making MWI a promising tool for quantifying myelin content in both normal and growth-restricted fetuses.

1.5.8.1.1   mcDESPOT

MWI by mcDESPOT combines data from T_1- and T_2-weighted volumes acquired for DESPOT$_1$ and DESPOT$_2$ [241]. The two-compartment model of MW and IEW was used, and exchange between compartments was included in the model. Parameter estimates in each voxel were obtained using a stochastic region contraction approach with four iterations. These steps followed the recommended guidelines in the literature and were used for the MWF fitting throughout the analysis [241].

The signal equations for mcDESPOT assume fast and slow relaxing compartments representing MW and IEW, respectively. The following equation represents the multicompartment signal equation for the SPGR sequence or DESPOT$_1$ [241].

$$M_{SPGR}^{SS} = M_{SPGR}(I - e^{A_{SPGR}TR})sin\alpha \times (1 - e^{A_{SPGR}TR}cos\alpha)^{-1} \qquad \textbf{1.16}$$

where

$$M_{SPGR} = \rho[f_F \quad f_S]^r \qquad \textbf{1.17}$$

and

$$A_{SPGR} = \begin{bmatrix} -\dfrac{1}{T_{1,F}} - k_{FS} & k_{SF} \\ k_{FS} & -\dfrac{1}{T_{1,S}} - k_{SF} \end{bmatrix} \qquad \textbf{1.18}$$

I is a 2x2 identity matrix, ρ is a factor proportional to the equilibrium longitudinal magnetization, f_F and f_S are the volume fractions of fast and slow relaxing compartments, respectively, k_{FS} and k_{SF} are the exchange rates between fast and slow relaxing compartments, respectively, and $T_{1,F}$ and $T_{1,S}$ are the T_1 relaxation times of the fast and slow relaxing compartments, respectively [241].

The following equation represents the multicompartment signal equation for the bSSFP sequence or DESPOT$_2$:

$$M_{bSSFP}^{SS} = (e^{A_{bSSFP}TR} - I)A_{bSSFP}^{-1}C \times [I - e^{A_{bSSFP}TR}R(\alpha)]^{-1} \qquad \textbf{1.19}$$

where

$$A_{bSSFP} = \begin{bmatrix} -\dfrac{1}{T_{2,F}} - k_{FS} & k_{SF} & \Delta\omega_F & 0 & 0 & 0 \\[2mm] k_{FS} & -\dfrac{1}{T_{2,S}} - k_{SF} & 0 & \Delta\omega_S & 0 & 0 \\[2mm] -\Delta\omega_F & 0 & -\dfrac{1}{T_{2,F}} - k_{FS} & k_{SF} & 0 & 0 \\[2mm] 0 & -\Delta\omega_S & k_{FS} & -\dfrac{1}{T_{2,S}} - k_{SF} & 0 & 0 \\[2mm] 0 & 0 & 0 & 0 & -\dfrac{1}{T_{1,F}} - k_{FS} & k_{SF} \\[2mm] 0 & 0 & 0 & 0 & k_{FS} & -\dfrac{1}{T_{1,S}} - k_{SF} \end{bmatrix} \quad \textbf{1.20}$$

and

$$C = \rho \begin{bmatrix} 0 & 0 & 0 & 0 & \dfrac{f_F}{T_{1,F}} & \dfrac{f_S}{T_{1,S}} \end{bmatrix} \qquad \textbf{1.21}$$

I is a 6x6 identity matrix, $R(\alpha)$ is a rotation matrix describing the RF pulse, $\Delta\omega_F$ and $\Delta\omega_S$ are the off-resonance effects of the fast and slow relaxing compartments, respectively, and $T_{2,F}$ and $T_{2,S}$ are the T$_2$ relaxation times of the fast and slow relaxing compartments, respectively. In this formulation, the MWF is equivalent to the volume fraction of the fast-relaxing compartment [241].

1.6 Thesis Overview

The primary motivation of this thesis is the eventual quantification of *in utero* fetal myelination with MR relaxometry. MR relaxometry is first used to quantify the relaxation times of human fetal tissues to assess fetal tissue development in the third trimester in uncomplicated pregnancies. Following the completion of this work, an extension of the technique is investigated to assess and quantify differences in fetal brain myelination in an animal model of spontaneous IUGR. Thus, the main objective of this thesis is to use MR relaxometry to assess fetal tissue development, specifically fetal myelination, *in utero*.

Chapter 2 presents work adapted from an original research manuscript entitled "Quantification of 1.5 T$_1$ and T$_2$* Relaxation Times of Fetal Tissues in Uncomplicated

Pregnancies". The purpose of this pilot study was to demonstrate the feasibility of quantifying T_1 and T_2^* relaxation times of various fetal tissues as a function of GA in uncomplicated human pregnancies at 1.5 T. Looking exclusively at uncomplicated pregnancies from 28- to 38-weeks gestation, the water T_1 of fetal lungs, liver, spleen, kidneys, and muscle, as well as the water and lipid T_1 of fetal adipose tissue, were not found to significantly change with GA. As for T_2^*, only the fetal spleen and muscle changed significantly with GA, while the lungs, liver, spleen, and kidneys did not.

Chapter 3 presents work from an original research manuscript entitled "Feasibility of MRI Quantification of Myelin Water Fraction in the Fetal Guinea Pig Brain." The study aimed to demonstrate the feasibility of MWI to quantify MWF *in utero* in the fetal guinea pig brain late in gestation. MWF maps were successfully generated for all fetal guinea pig brains, with MWF being quantified in the fetal corpus callosum and fornix. Furthermore, preliminary results showed that guinea pigs with IUGR have reduced MWF compared to those without IUGR.

Chapter 4 presents work from an original research manuscript entitled "Quantifying Myelin Water Fraction in a Guinea Pig Model of Spontaneous Intrauterine Growth Restriction." The study continues the work presented in Chapter 3, where we demonstrated the feasibility of MWI in the fetal environment. This study aimed to quantify MWF in a spontaneous IUGR guinea pig model. It was hypothesized that IUGR guinea pigs would have lower MWF than control guinea pigs. In the three analyzed regions– corpus callosum, fornix, and parasagittal white matter – the MWF was reduced in IUGR guinea pigs than in control guinea pigs.

Chapter 5 summarizes the work presented in the thesis, followed by potential avenues for future work related to this thesis.

CHAPTER 2

2 Quantification of 1.5 T_1 and T_2^* Relaxation Times of Fetal Tissues in Uncomplicated Pregnancies

2.1 Introduction

Fetal life is a significant period in human development because organ systems that sustain us throughout life outside the womb begin to develop during this time [4, 5]. MRI is a powerful tool for visualizing fetal anatomy and identifying pathology [171, 250]. In addition, it is an excellent modality that provides a non-invasive *in utero* assessment of tissue composition and function, such as oxygenation, lipid, and iron content, throughout the gestational period [251, 252].

Conventional fetal MRI is comprised of T_1-, T_2-, and T_2^*-weighted images [172]. Although these images provide clinically useful tissue contrast, the signal values of weighted-images are affected by other contrast mechanisms (e.g., proton density) and MR hardware and software, allowing data to be interpreted only qualitatively [196]. In contrast, T_1, T_2, and T_2^* relaxation times are quantitative MR parameters that reflect fundamental tissue properties sensitive to the tissue microenvironment [188]. Hence, their quantification by quantitative relaxometry techniques allows for comparing these values across time and between subjects [196].

Relaxation times are ideally not affected by influences unrelated to tissue properties, such as coil sensitivity and radiofrequency inhomogeneity, so they more directly reflect changes in tissue properties caused by any underlying pathology [188]. For instance, both placental T_1 and T_2^* are lower in pregnancies with intrauterine growth restriction (IUGR) than gestational age (GA)-matched normal pregnancies [251, 253]. Not only do both T_1 and T_2^* have the potential to identify placental dysfunction associated with IUGR, but they also can reflect changes in placental oxygenation as T_1 and T_2^* depend on the presence of dissolved oxygen and deoxyhemoglobin, respectively; quantifying this change would not be possible from either T_1- or T_2^*- weighted images [196].

Quantitative relaxometry also plays an important role in determining biophysical tissue parameters in adults [254]. Similarly, it is possible to use fetal tissue relaxometry to extract clinically useful tissue parameters that can provide insight into fetal development [255, 256]. For instance, changes in placental T_1 are related to changes in the placenta's partial pressure of oxygen [251]. Since the partial pressure of oxygen in the placenta differs between normal and complicated pregnancies, specifically placental insufficiency and fetal growth restriction, placental T_1 values can be used to provide a more direct yet non-invasive assessment of placental oxygenation and, subsequently, placental function [251]. Placental T_2^* changes can also assess placental function through placental blood oxygen saturation changes, which differs in placental dysfunction because it is related to changes in placental deoxyhemoglobin content [251]. Hence, expanding our current knowledge of fetal tissue relaxation times will enable the development of methodologies to quantify additional physiological and pathological tissue parameters.

T_2^* relaxation times of the fetal liver have been previously published at 1.5 T by Morris *et al.* and Goitein *et al*. [257, 258]. Furthermore, T_2^* relaxation times have been quantified for some fetal tissues, such as the brain, heart, and lungs, and were lower in fetuses with low birth weight [259]. It is important to quantify these relaxation times over GA because fetal tissues develop structurally throughout gestation; for instance, the fat fraction of adipose tissue (AT) is known to increase with GA in the third trimester [252]. Since both T_1 and T_2^* are sensitive to tissue microstructure, AT and other fetal organ structural changes may likely cause changes in T_1 and T_2^* throughout gestation [260].

The quantification of fetal tissue relaxation times as a function of GA will provide insight into fetal tissue development, facilitate comparison of images acquired at different GA, and contribute to methodologies with clinical utility. Therefore, the aim of this pilot study is to demonstrate the feasibility of quantifying previously unknown T_1 and T_2^* relaxation times of fetal tissues in uncomplicated pregnancies as a function of GA at 1.5 T.

2.2   Methods

2.2.1   Participant Demographics

This study was approved by the Western University Research Ethics Board (HSREB #103845). Women over 18 years old with singleton pregnancies and GA between 28 and 38 weeks consented to this study. The estimated delivery date was calculated using a first trimester ultrasound or certain last menstrual period following obstetrical guidelines [261]. Women were excluded from the study if they: 1) were pregnant with more than one fetus, 2) had a body habitus that prevented a successful MRI, or 3) had a medical contraindication that prevented them from being safely imaged by a non-contrast MRI. Participants with pregnancies complicated by diabetes or fetal growth restriction were excluded from the analysis to quantify the relaxation times of normal fetal tissues.

2.2.2   Imaging

Participants were imaged in the left lateral decubitus position in a 1.5 T MRI (General Electric Optima 450w, Milwaukee, WI), with a bore diameter of 70 cm and a 32-coil abdominal phased array. Initial T_2-weighted single-shot fast spin-echo (SSFSE) images were acquired to determine the fetal location and orientation. Two 3D water-fat chemical shift encoded (CSE) MRI volumes (specific implementation iterative decomposition of water and fat with echo asymmetry and least-squares estimation (IDEAL-IQ): repetition time (TR)/echo time (TE): 9.3 – 9.8/4.3 – 4.6 ms, Echo Train Length: 6, field of view: 50 cm, 128×128 pixels, slice thickness: 4–5 mm, 42–78 slices, ARC acceleration: 2x phase, 2.5 slice, and 32×32 calibration lines) were acquired axial to the maternal abdomen during two separate maternal breath holds, each with a different flip angle ($6°$ or $20°$); the acquisition time ranged from 12 to 24 seconds per breath hold. Slice thickness, field of view in the phase encoding direction, and resolution were altered between participants as needed to ensure complete acquisition in the maternal breath-hold. Reconstructed images were visually inspected for artifacts and imaging was repeated as necessary. Lipid-only images, water-only images, proton-density fat fraction (PDFF) maps, and R_2^* maps for

each participant were reconstructed using the 3D CSE-MRI method described in Yu *et al*. [262-264].

2.2.3   Fetal Tissue Segmentation

3D Slicer (v4.10.2-2019-5-220) [265-267] was used to segment the following tissues as described below. All segmentations underwent a 4-neighbour erosion to minimize partial volume biases.

Lungs and intraabdominal organ volumes of the liver and kidney cortex were segmented on the water-only images (Figure 2.1A). A 7-mm diameter region of interest (ROI) was placed in the same location of the spleen in the two water-only images.

Muscle volumes were segmented on the water-only images for the upper arms (outer shoulder to cubital and shoulder cut diagonally across armpit to elbow), forearms (cubital to outer wrist and elbow to inner wrist), thighs (along thigh length to inner and outer knee), and lower legs (outer and inner knee to outer and inner ankle, respectively) as well as the paravertebral muscle (along the spinal cord from the upper to lower back) (Figure 2.1B).

AT volumes were segmented on the PDFF maps for the following compartments: cheeks, upper arms, forearms, thorax, abdomen, thighs, and lower legs. A detailed description of how the AT compartments were divided is found in Giza *et al*. [268] (Figure 2.3C).
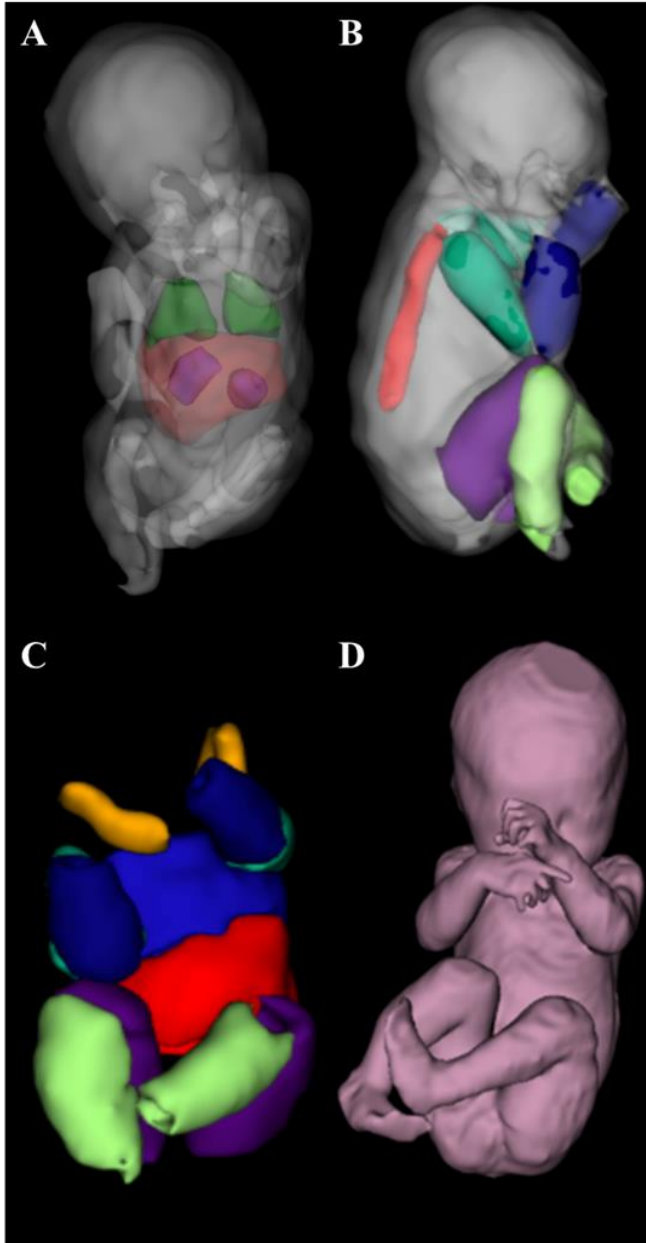
Figure 2.1. (A) The 3D fetal rendering highlighting segmentations of the lungs (green), liver (red), and kidneys (blue) **(B)** as well as segmentations of the fetal muscle of the upper arms (dark green), forearms (dark blue), thighs (purple), lower legs (light green), and the paravertebral (red) conducted using the water-only images. **(C)** Fetal adipose tissue volume segmentations were conducted using the PDFF maps. The cheeks are shown in orange, upper arms in green, forearms in dark blue, thorax in blue, abdomen in red, thighs in purple, and lower legs in light green. **(D)** A 3D fetal surface rendering is shown for reference.

2.2.4 T_1 & T_2^* Quantification

Before quantifying the relaxation times, the segmented volumes' positional changes were assessed between the 6° and 20° acquisitions. The changes were quantified by first locating the same region in a slice between the two acquisitions and then using a digital ruler to measure the change. Mean T_1 relaxation times were quantified using driven equilibrium single pulse observation of T_1 (DESPOT$_1$), as described in Deoni *et al.* [209]. For the lungs, intraabdominal organs, and muscle, the mean signal intensities from the 6° and 20° water-only images were used to determine the mean water T_1 relaxation times. Mean T_2^* relaxation times of the lungs, intraabdominal organs, and muscle were determined by taking the inverse of the signal values of the segmentations on the 6° and 20° R_2^* maps. For AT, the mean signal intensities of the 6° and 20° water-only and lipid-only images were used to determine the mean water and mean lipid T_1 relaxation times, respectively. Due to pulse sequence limitations, the 6° and 20° DESPOT$_1$ acquisitions had different TRs. The two TRs were then used to calculate two mean T_1 relaxation times for each analyzed tissue. The percent difference between the two T_1s of each tissue for each participant was then determined.

2.2.5   Statistical Analysis

Linear regression analysis was conducted for the T_1 and T_2^* relaxation times of each analyzed tissue as a function of GA. F-tests were performed for each tissue to determine if their T_1 and T_2^* slopes as a function of GA were significantly different from zero, indicating that the tissues' relaxation times changed significantly with GA. F-tests were also conducted to determine if the slopes and Y-intercepts of water T_1s and T_2^*s of different muscle locations as a function of GA were significantly different from each other. The same analysis was also performed for the water and lipid T_1s of the AT compartments. The D'Agostino–Pearson test was first performed to test the T_2^* from the 6° and 20° maps for normality. A one-sample t-test was performed on the relaxation time difference values to assess the level of agreement between T_2^* relaxation times derived from the 6° and 20° IDEAL T_2^* maps (6° − 20°). These difference scores were tested against a value of zero, which would indicate the measurements were identical. P-values

less than 0.05 were determined to be statistically significant. All statistics were performed in GraphPad Prism version 8.0.2 for Windows, GraphPad Software, San Diego, California USA, www.graphpad.com.

2.3 Results

Of the 19 imaged participants, data from seven participants were excluded because of fetal growth restriction or maternal diabetes. Three more pregnancies were excluded due to insufficient contrast-to-noise-ratio between adjacent tissues making segmentation impossible, leaving nine fetuses from uncomplicated pregnancies for analysis. Clinical information about the participants, such as maternal age, pre-pregnancy body mass index (BMI) and fetal sex, are summarized in Table 2.1.

Table 2.1. Participant Demographics

Characteristic	N
Maternal Age (years)	
20-29	3 (33%)
30-39	6 (66%)
Maternal Pre-Pregnancy BMI (kg/m^2)	
Underweight ($<$ 18.5)	1 (11%)
Normal (18.5 – 24.9)	4 (44%)
Overweight and Obese (25.0-39.9)	4 (44%)
Sex of Fetus	
Male	7 78%)
Female	2 (22%)

Imaging was repeated for three of the DESPOT$_1$ acquisitions due to significant fetal motion, yielding a complete set of nine DESPOT$_1$ acquisitions with no easily observable motion artifacts to be analyzed. There were positional changes of the segmented volumes between the DESPOT$_1$ acquisitions for all nine participants, but the change was always

less than 2 cm. The percent difference between the two T_1 relaxation times determined using the different TRs was always less than 2.5%.

2.3.1   Lungs and Intraabdominal Organs

The water T_1 relaxation times of the lungs, liver, spleen, and kidneys did not vary significantly with GA (F-test, lungs [$p = 0.89$]; liver [$p = 0.14$]; spleen [$p = 0.59$]; kidneys [$p = 0.97$]). The mean water T_1 relaxation times of the lungs and intraabdominal organs are presented in Figure 2.2 and Table 2.2. Only the T_2^* relaxation times of the spleen decreased significantly with increasing GA (F-test, $p < 0.05$). T_2^* relaxation times of the lungs, liver, and kidneys did not vary significantly with GA [F-test, lungs [$p = 0.67$]; liver [$p = 0.05$]; kidneys [$p = 0.70$]). The mean T_2^* relaxation times of the lungs and intraabdominal organs are presented in Figure 2.3 and Table 2.3. All T_2^* measurements for these organs passed the normality test (D'Agostino–Pearson t-test, lungs: $6°$ [$p = 0.85$], $20°$ [$p = 0.58$]; liver: $6°$ [$p = 0.46$], $20°$ [$p = 0.36$]; spleen: $6°$ [$p = 0.76$], $20°$ [$p = 0.43$]; kidneys: $6°$ [$p = 0.97$], $20°$ [$p = 0.13$]). T_2^* measurements for each of these organs from the $6°$ and $20°$ R_2^* maps were not found to be different (one-sample t-test, lungs [$p = 0.16$]; liver [$p = 0.14$]; spleen [$p = 0.19$]; kidneys [$p = 0.07$]).

2.3.2   Muscle

The slopes and Y-intercepts of the water T_1 values of the different muscle locations were not significantly different from each other (F-test, slope [$p = 0.98$]; Y-intercept [$p = 0.92$]). The muscle water T_1 relaxation times of all the muscle locations combined did not vary significantly with GA (F-test, $p = 0.22$), and their mean ± SD is 800.7 ± 77.1 ms (Figure 2.2 and Table 2.2). The slopes and Y-intercepts of the T_2^* values of the different muscle locations were not significantly different from each other (F-test, slope [$p = 0.06$]; Y-intercept [$p = 0.20$]). The mean T_2^* relaxation times of all the combined muscle locations decreased significantly with gestation (F-test, $p < 0.05$) (Figure 2.3 and Table 2.3). Mean muscle T_2^* measurements from the $6°$ and $20°$ R_2^* maps passed the normality test (D'Agostino–Pearson t-test, $6°$ [$p = 0.57$], $20°$ [$p = 0.49$]). Mean T_2^* measurements from the $6°$ and $20°$ R_2^* maps were not found to be different (one-sample t-test, $p = 0.12$).
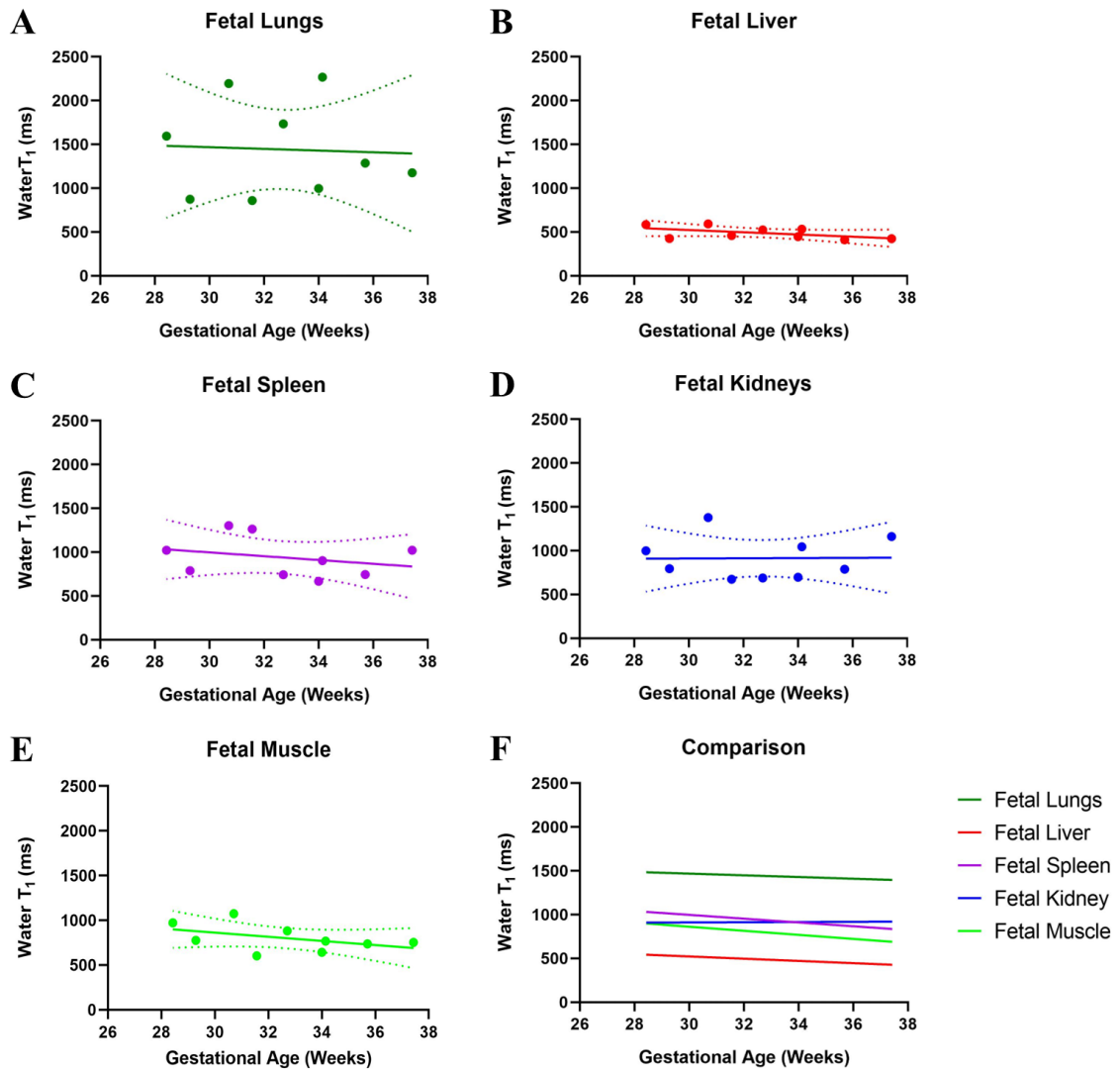
Figure 2.2. Mean water T_1 relaxation times, regression lines, and 95% confidence intervals of the **(A)** fetal lungs, **(B)** fetal liver, **(C)** fetal spleen, **(D)** fetal kidneys, and **(E)** of all fetal muscle locations combined are plotted independently as a function of GA. **(F)** The regression lines of the mean water T_1 relaxation times of all five tissues are plotted together as a function of GA for comparison.
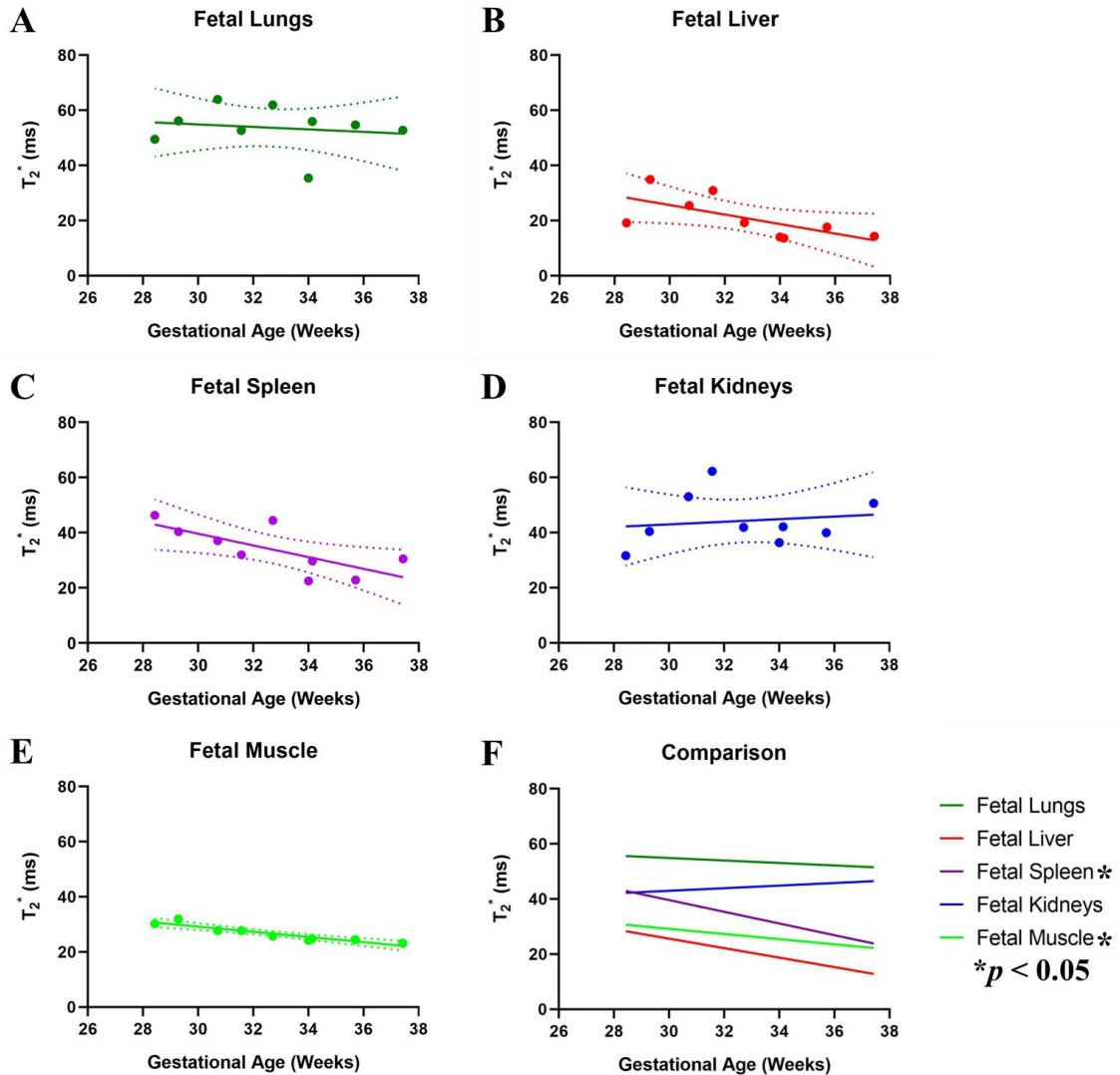
Figure 2.3. Mean water T_2^* relaxation times, regression lines, and 95% confidence intervals of the **(A)** fetal lungs, **(B)** fetal liver, **(C)** fetal spleen, **(D)** fetal kidneys, **(E)** and of all fetal muscle locations combined plotted independently as a function of GA. **(F)** The regression lines of the mean water T_2^* relaxation times of all five tissues are plotted together as a function of GA for comparison. The black asterisk (*) indicates that the slope of the mean T_2^* relaxation time of the tissue as a function of GA is significantly different from zero ($p < 0.05$).

2.3.3 Adipose Tissue

The slopes and Y-intercepts of the water T_1 values of the AT compartments combined were not significantly different from each other (F-test, slope [$p = 0.72$]; Y-intercept [$p = 0.91$]). The mean water T_1 relaxation times of the combined AT compartments did not vary significantly with GA (F-test, $p = 0.36$), and their mean $\pm$ SD is 946.6 $\pm$ 128.2 ms (Figure 2.4 and Table 2.2). The slopes and Y-intercepts of the lipid T_1 values of the AT compartments were not significantly different from each other (F-test, slope [$p = 0.99$]; Y-intercept [$p = 0.48$]). The mean lipid T_1 relaxation times of the combined AT compartments decreased with GA, but not significantly (F-test, $p = 0.14$); their mean $\pm$ SD is 224.9 $\pm$ 41.9 ms (Figure 2.4 and Table 2.2).
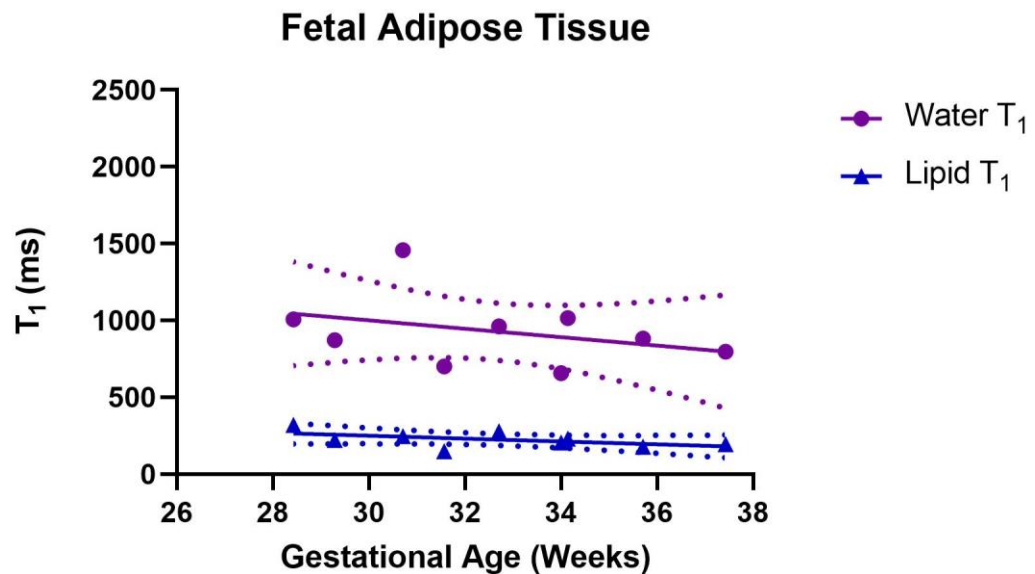
Figure 2.4. Mean water T_1 and mean lipid T_1 relaxation times, regression lines, and 95% confidence intervals of all fetal adipose tissue compartments combined are plotted as a function of gestational age. To facilitate comparison, the y-axis of the graph is the same as the graphs shown in Figure 2.2.

Table 2.2. Mean Water T₁ of Fetal Lungs, Intraabdominal Organs, and Fetal Muscle, and Mean Water and Lipid T₁ of Fetal Adipose Tissue at 1.5 T

Tissue	T$_1$ Relaxation Time (ms) [mean ± SD]	95% Confidence Interval (ms)	*p* value of slope
Fetal Lungs (Water)	1443 ± 102.4	1030 – 1856	0.89
Fetal Liver (Water)	489.1 ± 47.5	435.0 – 543.3	0.14
Fetal Spleen (Water)	939.7 ± 113.0	762.4 – 1117	0.59
Fetal Kidneys (Water)	914.1 ± 62.8	724.6 – 1103	0.97
Fetal Muscle (Water)	800.7 ± 77.1	684.5 – 917.0	0.22
Fetal AT (Water)	946.6 ± 128.2	782.4 – 1111	0.36
Fetal AT (Lipid)	224.9 ± 41.9	184.7 – 265.1	0.14

Table 2.3. Mean T$_2$* of Fetal Lungs, Intraabdominal Organs, and Fetal Muscle at 1.5 T.

Tissue	T$_2$* Relaxation Time (ms) [mean ± SD]	95% Confidence Interval (ms)	*p* value of slope	Slope ± SEM (ms/day)	Y-Intercept ± SEM
Fetal Lungs	53.7 ± 7.9	47.4 – 60.0	0.67		
Fetal Liver	21.0 ± 1.7	15.1 – 27.0	0.05		
Fetal Kidneys	44.3 ± 3.1	37.0 – 51.5	0.70		
Fetal Spleen			<0.05*	-2.1 ± 0.8	103 ± 25.0
Fetal Muscle			<0.05*	-0.94 ± 0.1	57.3 ± 4

Note – The asterisk (*) indicates that the slope of the mean T$_2$* relaxation time of the tissue as a function of GA is significantly different from zero ($p < 0.05$).

2.1 Discussion

Fetal tissue relaxometry provides metrics that enable comparison between subjects imaged on different MRI systems, with different protocols, and at different time points in pregnancy. This pilot study has successfully demonstrated the quantification of the T$_1$ and T$_2$* relaxation times of multiple fetal tissues in third trimester uncomplicated pregnancies as a function of GA. Furthermore, the study found that T$_1$ likely remains relatively stable during the third trimester for most investigated fetal tissues, except AT. Changes in T$_2$* were observed for the spleen, liver, and muscle during the relatively short investigated gestational period. The T$_2$* values of AT compartments of seven participants are previously published, so those data were not included. The study found that the T$_2$* values of the thorax, abdomen, and lower legs AT decreased significantly with GA [268].

This study was conducted in the third trimester because subcutaneous AT undergoes rapid development mid-late gestation, and these changes can be detected by MRI [269]. Nonetheless, many fetal tissues become well-differentiated prior to the third trimester and begin performing the functions they serve after birth, such as the liver producing bile and kidneys producing urine [270, 271]. As a result, the consistency with adult values and the lack of change in T_1 suggest that these tissues have achieved structural maturity at the investigated GA. For instance, the lack of change of T_1 relaxation times of lungs and intraabdominal organs with GA and similarity to the corresponding published adult values correlates to a functional maturity of these tissues, which only need minimal support if the fetus is delivered prematurely in the third trimester [189].

The significant decrease in spleen T_2^* and the nonsignificant decrease in liver T_2^* values are likely associated with fetal extramedullary hematopoiesis [8, 9]. Iron, an essential component of hematopoiesis, is paramagnetic and causes changes to the local magnetic field's uniformity, affecting T_2^* relaxation times [272, 273]. Therefore, the reduction in the T_2^* relaxation times over gestation can be explained by increased tissue iron content due to hematopoiesis. Although the fetal liver is also a hematopoiesis site, hematopoiesis shifts from the liver to the spleen in the third trimester [9]. This shift may explain the lack of a significant T_2^* decrease observed in the liver. Both liver T_2^* and spleen T_2^* values were consistent with their respective previously published values for the same gestational period [257-259].

The T_1 relaxation times of muscle also did not change with GA and were consistent with adult values [189]. The absence of significant change suggests that the structural composition of muscle may not change dramatically during the third trimester. Secondary myogenesis, during which most skeletal muscle fibres are formed, occurs until approximately the seventh month of gestation [274, 275]. The change in the T_2^* relaxation times of the fetal muscle is a possible result of increasing iron concentration due to myoglobin accumulation, the iron-containing protein found in adult muscle [276]. The separation of muscle into its different locations was conducted to assess whether the water T_1 and T_2^* values differed by location. Water T_1 and T_2^* values of the different

muscle locations did not significantly differ, suggesting that muscle microstructure is similar at different fetal locations for a given GA during the investigated period.

Both the water and lipid T_1 relaxation times of AT decreased over gestation and were higher than their published adult values. The fat signal fraction of fetal AT has been found to increase with GA (12% − 37%) but was still lower than the fat fractions of both neonatal and mature adult AT of 77.9% and 90%, respectively [252, 277]. Hence, AT development continuing beyond the investigated period could explain the decrease in both water and lipid T_1 with gestation. Furthermore, the water and lipid T_1 values did not significantly vary between compartments, indicating that water and lipid T_1 of AT as a function of GA does not depend on AT location, respectively.

A novel aspect of this study is that both the water and lipid T_1 of AT were quantified simultaneously to assess the development of adipocytes' lipid and water components separately. A change in either the water or lipid T_1 could tell whether only the lipid-containing vesicles are developing or only the water components. Like the muscle, AT was separated into compartments since fetal fat fraction in AT compartments differs by location in the third trimester [268]. The lipid T_1 relaxation times of AT were not significantly different between compartments, suggesting that each AT location's lipid-containing vesicles' microstructure is similar at a given GA. The absence of water T_1 change suggests a similar interpretation for the water-dominated components of AT compartments.

2.1.1 Limitations

First, the presence of fetal motion between DESPOT$_1$ acquisitions may have affected study results. The changes in fetal position in the receive field of the abdominal array used for data acquisition could have caused changes in signal intensity between the two DESPOT$_1$ acquisitions that were not due to T_1 relaxation; however, we found the positional changes to be relatively small (< 2 cm). Although these fetal movements precluded quantifying T_1 on a pixel-by-pixel basis, they did not significantly alter the segmented volumes' measured signal intensity as the receive field does not change rapidly in space. Therefore, these small movements did not substantially affect the T_1

measurements. Due to limitations of pulse sequence prescription, the TR for the two DESPOT$_1$ acquisitions varied by as much as 0.23 ms; this small difference in TR did not substantially affect the calculated T$_1$ as the percent difference between T$_1$ values calculated with the two TRs was always less than 2.5%. The T$_2^*$ measurements were insensitive to these effects because they were derived from a single image acquisition.

This study had a small sample size and, hence, the limitations of using the data generated from nine women to make definite statements about fetal tissue relaxometry are recognized. The limited GA range investigated, 28–38 weeks, means that caution should be exercised when interpreting linear fits for extrapolation of relaxation times outside the studied gestational period. Due to limited images resolution and resultant difficulties in distinguishing grey and white matter, the T$_1$ and T$_2^*$ relaxation times of both grey and white matter were not quantified. Finally, we could not determine potential sex differences due to the small sample size and unequal proportion of male and female fetuses, although significant differences in individual tissues' composition would be unlikely.

Gold-standard methods to measure T$_1$, such as inversion recovery, were not feasible for this study because they require acquisition times too long to be used for fetal imaging; however, DESPOT$_1$ has been previously used to quantify the T$_1$ relaxation times of a wide variety of organs and tissues [209, 278]; the same statement is also applicable for IDEAL measurement of T$_2^*$ [262, 279]. Given the range of applications for which both methods have been used, applying these methodologies to fetal tissues is appropriate.

One of the benefits of IDEAL-IQ is that we measure both T$_1$ and T$_2^*$ simultaneously. IDEAL-IQ also reconstructs water-only and lipid-only images from the same acquisition; this was particularly useful for AT as both the water and lipid T$_1$ of AT could be quantified simultaneously. The fetal tissue T$_1$ values are consistent with their respective adult values, while the T$_2^*$ of the intraabdominal organs are consistent with previously published values, providing evidence that the measurements are in the appropriate range [189].

T_1 and T_2^* relaxation times can be used directly as markers for pathologies, such as those associated with placental dysfunction and fetal growth restriction, or in other methodologies to identify deviations from normal when assessing processes such as lipid storage, muscle metabolism, and hematopoiesis. This study has successfully shown that it is feasible to quantify the relaxation times of fetal tissues. Although the data require validation due to the small sample size, it expands fetal tissue relaxometry knowledge. This study has shown that it is feasible to quantify fetal relaxation times, and the methodology can now be used in larger studies of normal and abnormal pregnancies. Future work should focus on increasing sample size and improving the resolution of the images used for relaxometry to allow for reliable quantification of the fetal brain gray and white matter's relaxation times. Furthermore, a complete characterization of relaxation times throughout pregnancy requires investigating T_1, T_2^* and T_2 at earlier GA and across gestation.

2.1.2   Conclusion

This study demonstrated the feasibility of quantifying T_1 and T_2^* relaxation times of various fetal tissues in uncomplicated pregnancies between 28- and 38-weeks gestation at 1.5 T. This study's results can be used as a potential metric to assist in comparing MR images at different GA and help to interpret changes in fetal physiology and pathology during gestation.

CHAPTER 3

3 Feasibility of MRI Quantification of Myelin Water Fraction in the Fetal Guinea Pig Brain

3.1 Introduction

The brain is a key organ that begins to develop during the third week of gestation [280]. A process that begins in the brain during fetal life is the development of myelin [4, 5]. Myelin is a lipid-rich substance whose primary role is to insulate nerve cell axons to increase the rate at which action potentials travel along the axon [114]. It is essential for healthy brain development as it facilitates long-range neuronal communications networks to support higher-order cognitive, sensory, and motor functions [127]. Evidence of the myelin sheath is first seen at 18 weeks gestation, followed by an increasing rate of myelination that continues beyond the gestational period [7, 131].

Assessment of fetal myelin content can provide insight into fetal neurodevelopment and improve our understanding of pathologies' impact on the fetal brain. For instance, a post-mortem study showed that a notable difference between control newborn infants and those with intrauterine growth restriction (IUGR) is a decrease in myelin content [143], but we have yet to quantify the difference *in utero*.

Fetal MRI is increasingly used for clinical and research purposes because MRI is non-invasive, does not use ionizing radiation, has a potentially large field of view, and provides excellent soft-tissue contrast [281]. Due to current technological limitations, conventional MRI cannot directly assess myelin lipids and proteins composing the myelin sheath because the signal from these larger, slow tumbling molecules decays to zero in approximately 50 to 100 µs [133]. Although ultra-short echo time sequences can detect T_2^* relaxation times in the targeted range and have been successful in imaging myelin lipid, the current acquisition times of these sequences are long (100 minutes) and not feasible for fetal imaging [218, 282]. Fortunately, the MR signal from the aqueous components of the myelin sheath has MRI-accessible decay times greater than 10 ms

[114]. Thus, myelin structure and pathology can be probed by studying the MRI-visible water associated with myelin [114].

Myelin water imaging (MWI) involves separating signals from individual water compartments with signal amplitudes proportional to the relative amounts of water in each environment [114]. The primary measurement in MWI is the myelin water fraction (MWF), which is defined as the ratio of signal from protons in myelin water to the total signal from all protons in water (myelin water and intra-/extra-cellular water) within the voxel [114]. A previous histological study has shown a strong correlation between MWF and staining for myelin, validating MWF as a strong marker for myelin [283]. Multiple studies have successfully used MWI to quantify MWF in adults, adolescents, children, and neonates [114, 243, 284].

Since guinea pigs have their most rapid phase of myelination initiated in the latter half of pregnancy like humans [164], they are an ideal model of neurologic developmental programming. Thus, the aim of this pilot study was to demonstrate the feasibility of conducting MWI for the quantification of MWF in the fetal brain *in utero* in a pre-clinical guinea pig model of human pregnancy.

3.2   Materials & Methods

All study procedures were reviewed, approved, and monitored by the institution's Animal Care and Ethics Committee. Eleven pregnant, chow-fed female Dunkin-Hartley guinea pigs late in gestation (59–61 days gestation, term = ~68 days) with a total of 38 fetuses were anesthetized using isoflurane (induced with 4.5% isoflurane with two litres/ minute O_2 and maintained via nose cone with a 1.5%–2.5% isoflurane with 2 litres/minute O_2).

3.2.1   Imaging

All imaging was performed with a 3.0 T MRI scanner (Discovery MR750, GE Healthcare, Waukesha, WI) with a 32-element human cardiac coil array (In Vivo Corp., Gainesville, FL). Anatomical 3D T_2-weighted ^1H images of the entire maternal GP, which included the maternal brain and uterus, were acquired with a spin-echo sequence:

repetition time (TR)/echo time (TE): 2000/120 ms, NEX: 2, voxel size: 0.7 x 0.7 x 0.7 mm–0.9 x 0.9 x 0.9 mm; the T_2-weighted acquisition was approximately 6–8 minutes long.

Eight spoiled gradient echo volumes (TR/TE: 4.6 – 5.9 /1.9 – 2.0 ms) for driven equilibrium single pulse observation of T_1 (DESPOT$_1$) were acquired at varying flip angles (α: 2° – 16°, increasing increments of 2°) in one acquisition [209]. Two sets of eight balanced steady-state free precession volumes (TR/TE: 6.4 – 7.4 /3.2 – 3.7 ms) were acquired at varying flip angles (α: 8° – 64°, increasing increments of 8°) and at 0° and 180° phase increments in a separate, single acquisition [209]. The eight DESPOT$_1$ volumes were acquired in approximately 7 – 12 minutes, while the 16 DESPOT$_2$ volumes were acquired in approximately 20 – 40 minutes [209]. All DESPOT$_{1/2}$ acquisitions had the same imaging parameters: field-of-view (FOV): 23 – 24 cm, voxel size: 0.7 x 0.7 x 0.7 mm – 0.9 mm x 0.9 mm x 0.9 mm, acceleration factor: 2x (ASSET [DESPOT$_1$] & ARC [DESPOT$_2$]). The field-of-view and resolution of the DESPOT$_{1/2}$ volumes were matched to the 3D T_2-weighted images. To determine the ideal resolution in a reasonable time frame, two sets of acquisitions with different resolutions were acquired. The first set had a resolution of 0.7 mm^3, while the second set had a varied resolution between 0.75 mm^3 and 0.9 mm^3.

After imaging was finished, the sows were monitored and kept on O_2 until awake. Subsequently, they were transferred to be kept under a heating lamp and monitored until they were fully awake and mobile. The sows were then returned to their cages.

3.2.2   MWF Map Reconstruction and MWF Quantification

A mask of the maternal and fetal guinea pig brains was manually generated from the T_2-weighted images using FSLeyes [285]. Quantitative Imaging Tools (QUIT) [286] was used to generate the T_1 map, T_2 map, and MWF maps for each maternal and fetal guinea pig brain. Multicomponent DESPOT$_{1/2}$ (mcDESPOT) was used to reconstruct each GP brain's MWF map [241]. Using 3D Slicer (4.11.0–2019-12-02) [265-267], approximately six circular regions of interest (ROIs) with a diameter of 1 mm and 0.5 mm and 1–2

pixels were placed in the corpus callosum (CC) and fornix (FOR), respectively, of each maternal brain, and used as an internal control.

Approximately six circular ROIs with a diameter of 0.5 mm and 1-2 pixels were then placed in the CC and FOR of each fetal guinea pig brain. The ROIs were first placed on the T_2-weighted images and then transferred to the MWF maps to quantify the MWF values. Images from Gareau *et al.* were used for reference to identify the CC with the FOR located immediately below the CC [162, 287]. In addition, each fetal brain and liver were manually segmented using the T_2-weighted images to determine the brain-to-liver volume ratio (BLVR) to determine the presence of IUGR (BLVR $\geq$ 0.7) [66, 288].

3.2.3   Animal Collection

The maternal sows were euthanized via CO_2 inhalation 2–3 days after imaging (61–63 days gestation) [289]. All fetuses were removed from the sow, confirmed dead, and weighed immediately. The following tissues were removed and weighed immediately: maternal brain, fetal brain, and fetal liver. Additionally, each fetus' brain-to-liver weight ratio (BLWR) was calculated by dividing the fetal brain weight by the liver weight to confirm normal growth as defined by a BLWR $<$ 0.7 [290, 291]. Following tissue weighting, maternal and fetal brains were coronally sectioned at the optic chiasm through the mamillary bodies, and caudal and rostral brain portions were fixed in 4% paraformaldehyde for 24 hours. Brain tissues were then rinsed three times with phosphate-buffered saline (PBS) for 2-hour intervals and stored in 70% ethanol for later processing.

3.2.4   Tissue Processing and Embedding

All tissue processing and paraffin embedding was performed at the London Regional Cancer Program (London Health Sciences Centre, London, ON). Subsequent sectioning, staining, and image analysis were performed at the Biotron Integrated Microscopy Facility (Biotron Centre for Experimental Climate Change Research, London, ON). Using a Leica RM2455 Rotary Microtome (Leica Biosystems, Nuβlock), 5 μm coronal sections were taken at a plane where the mamillary body of the guinea pig brains was

revealed before being mounted on Superfrost plus slides (Fisher Scientific Canada, Nepean, ON).

3.2.5 MBP Staining

All steps were conducted at room temperature except where specified. Slides containing paraffin sections were dewaxed in three changes of Xylene for 5 minutes and then rehydrated to water in a descending series of ethanol baths—100%, 90%, and 70%—for two changes of 2 minutes each. This procedure was followed by hydration for 5 minutes in running tap water and equilibration in deionized water. Slides were then subjected to a heat-induced epitope retrieval process in 10 mM sodium citrate buffer (EMS, Hatfield, PA) at 90°C in a pressure cooker for 15 minutes. The slides were washed three times in phosphate-buffered saline (PBS), and any endogenous peroxidases were quenched in 3% hydrogen peroxide for 10 minutes; three more PBS washes followed this. Tissues were circled with a hydrophobic pen (Dako, Agilent Technologies, Santa Clara, CA), and all subsequent steps were carried out in a humidified chamber. Non-specific antibody binding was first blocked with Background Sniper (Biocare Medical, Concord, CA) for 10 minutes, followed by a brief rinse in PBS and subsequent incubation with a mouse monoclonal anti-Myelin Basic Protein (MBP) antibody (LSBio, Seattle, WA, cat. B3315) overnight at 4°C [162].

The following day, slides were rinsed three times in PBS before being incubated for 40 minutes with an ImmPress horse anti-mouse horseradish peroxidase (HRP) conjugated secondary antibody (Vector Laboratories, Burlingame, CA) to achieve less non-specific staining. Slides were again rinsed in PBS before applying 3, 30 - diaminobenzidine (Sigma-Millipore, St. Louis, MO) for 5 minutes to detect signals. Slides were rinsed for 5 minutes in tap water and dehydrated through an ascending series of ethanol baths—70%, 90%, and 100%—for two changes of 30 s each. The slides were cleared in three baths of Xylene for 5 min each, then mounted under coverslips using Permount media (Fisher Scientific Canada, Nepean, ON) [162].

3.2.6　MBP Staining Imaging and Data Analysis

Scans of each coronal section of brain tissue were obtained at five times magnification on a Nikon Ti2e microscope system (Mississauga, ON) using the large image stitching method (Nikon's NIS elements, Nikon Canada Inc., Mississauga, ON). Whole-brain slide scans were exported as TIFF images and analyzed using Image Pro Software (Media Cybernetics, Rockwood, MD). The images were first calibrated to convert measurements from intensity to optical density using the full 8-bit depth range of 0–255. A gradient of thresholds spanning the signal optical density range was established and applied to display a colored overlay marking depth of staining for visual qualitative comparison matching the MWF maps. For quantitative data, 6–7 ROIs were drawn within the FOR and CC. A binary threshold for MBP stain intensity was determined by testing on multiple brains before being uniformly applied for quantification within the ROIs.

3.2.7　Statistical Analysis

A simple linear regression analysis (coefficient of determination, R^2) was performed between the MWF and MBP stain intensity for each of the maternal CC, maternal FOR, fetal CC, and fetal FOR. F-tests were also conducted to determine if the slope of MWF of all the analyzed regions versus their MBP stain intensity was significantly different from zero ($\alpha = 0.05$). To compare the MWF and MBP stain intensity measurements of the maternal structures with their fetal counterparts, the CC and FOR values of all fetuses within a litter were averaged so that each litter had one fetal CC and FOR measurement, respectively. The nine averaged fetal CC, and fetal FOR values were then compared to the nine maternal CC and FOR measurements, respectively. A paired t-test was performed to test for significance between the following: maternal CC MWF and fetal CC mean MWF, maternal CC MBP stain intensity and fetal CC mean MBP stain intensity, maternal FOR MWF and fetal FOR mean MWF, and maternal FOR MBP stain intensity and fetal FOR mean MBP stain intensity. Incorporating a linear mixed model to consider litter effects, a one-way analysis of variance (ANOVA) was performed to compare the MWF of the fetal CC, and fetal FOR; the same analysis was done for the MBP stain intensity of the fetal CC and fetal FOR. Litter size was used as a covariate in

the analysis to reduce the effects of the variability within the intrauterine environment experienced by the fetal guinea pig litters from a single pregnancy [166]. Since multiple t-tests were conducted on the same data set, a Bonferroni correction was applied, adjusting the alpha value to 0.0083.

A simple linear regression analysis was performed between the following: BLWR v. fetal CC MBP stain intensity, BLWR v. fetal FOR MBP stain intensity, BLVR v. fetal CC MWF, and BLVR v. fetal FOR MWF. F-tests were also conducted to see if the slopes of BLWR v. MBP stain intensity of the two fetal regions and of BLVR v. MWF of the two fetal regions were significantly different from zero ($\alpha = 0.05$). A simple linear regression was also conducted between BLWR and BLVR and a subsequent F-test to see if the slope of the two ratios was significantly different from zero ($\alpha = 0.05$).

An ANOVA incorporating the linear mixed model was performed using RStudio Team (2020). RStudio: Integrated Development for R. RStudio, PBC, Boston, MA URL http://www. rstudio.com/. The paired t-tests, simple linear regression analysis, and F-tests were performed using GraphPad Prism version 9.3.1 for Windows, GraphPad Software, San Diego, CA, www.graphpad.com.

3.3   Results

No adverse events occurred in the maternal guinea pigs during scanning. MWF maps were successfully generated for each maternal and fetal guinea pig brain. One maternal guinea pig miscarried her pregnancy at 64 days gestation and died during delivery; the sow and her four fetuses were found demised prior to collection. Brains from one maternal guinea pig and her three fetuses did not go to staining as their brains did not fix sufficiently for dissection. Imaging and staining data from nine maternal and 31 fetal guinea pigs were analyzed and compared. Five of the 31 fetal guinea pigs analyzed had both a BLWR and BLVR ≥ 0.7, while the remaining 26 had both a BLWR and BLVR < 0.7 (Table 3.1).

Table 3.1. Characteristics of Fetal Guinea Pigs

Characteristic	Non-IUGR ($N = 26$)	IUGR ($N = 5$)
BLWR (range)	0.42 – 0.69	0.76 – 1.24
BLVR (range)	0.45 – 0.68	0.73 – 1.29
Body Weight (grams)	73.9 - 113.6	65.0 – 89.9
Sex of Fetus		
Male	12	2
Female	14	3
Maternal Guinea Pig		
1	2	0
2	2	2
3	3	1
4	2	2
5	3	0
6	4	0
7	4	0
8	3	0
9	3	0

The mean MWF of the maternal CC and FOR was (mean ± SD) 0.338 ± 0.016 and 0.340 ± 0.017, respectively [Figure 3.1]. The mean MWF of the fetal CC and FOR was (mean ± SD) 0.214 ± 0.016 and 0.305 ± 0.025, respectively [Figure 3.2]. The simple linear regression and F-test results showed that the MWF and MBP stain intensity of all four regions correlated well ($R^2 = 0.81$) [Figure 3.3]. The coefficients of determination of the four regions individually are as follows: maternal CC ($R^2 = 0.26$), maternal FOR ($R^2 = 0.11$), fetal CC ($R^2 = 0.14$), and fetal FOR ($R^2 = 0.27$).
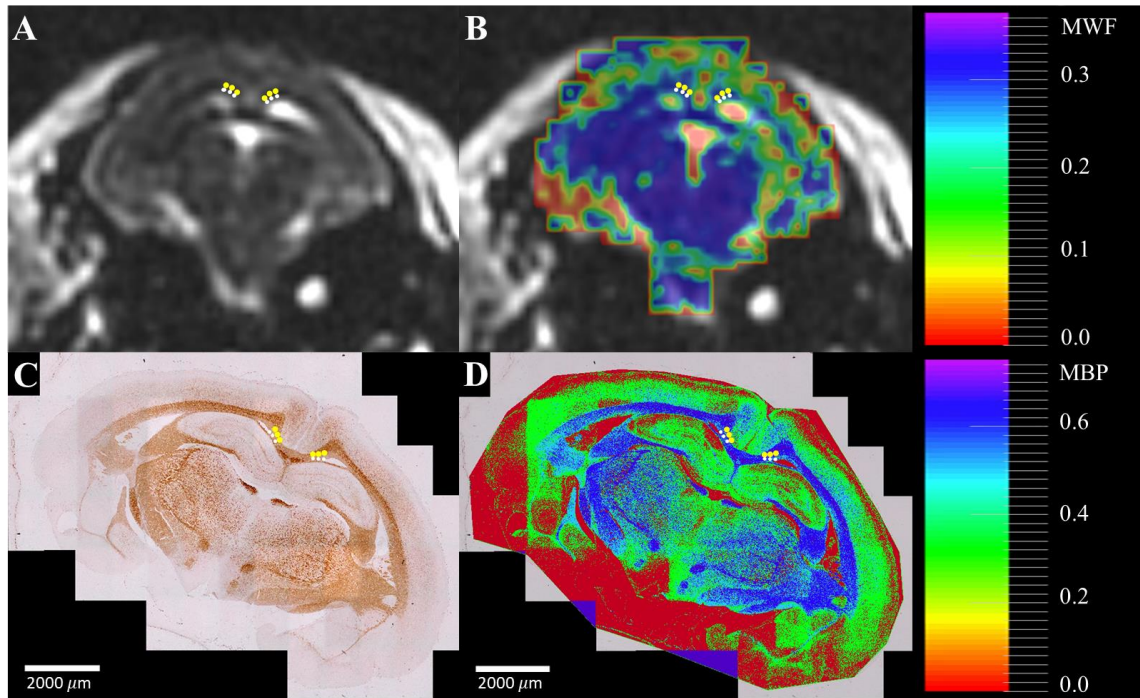
Figure 3.1 (A) Coronal T$_2$-weighted image slice of the maternal guinea pig brain. **(B)** A MWF map of the same guinea pig brain slice overlaid on the anatomical image shown in A. A color scale for the MWF map is shown for reference. **(C)** MBP immunohistochemical (IHC) staining at a similar coronal plane as the maternal guinea pig brain shown in A and B. **(D)** The assignment of colors to the brain section seen in C based on MBP IHC stain intensity (Scale bar = 2000 μm). A color scale for the MBP stain intensity map is shown for reference. In all four figures, regions of interest are placed in the maternal CC (yellow) and FOR (white).
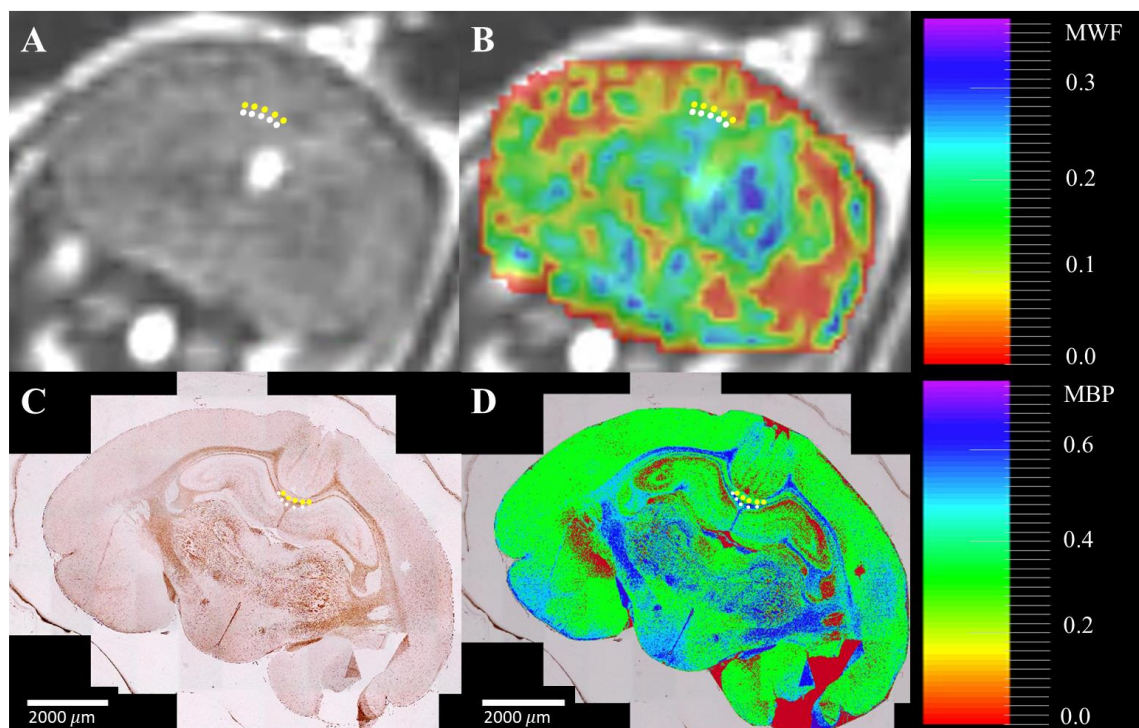
Figure 3.2. (A) Coronal T_2-weighted image slice of the fetal guinea pig brain. **(B)** A MWF map of the same guinea pig brain slice overlaid on the anatomical image shown in A. A color scale for the MWF map is shown for reference. **(C)** MBP IHC staining at a similar coronal plane as the fetal guinea pig brain shown in A and B. **(D)** The assignment of colors to the brain section seen in C based on MBP IHC stain intensity (Scale bar = 2000μm). A color scale for the MBP stain intensity map is shown for reference. In all four figures, regions of interest are placed in the fetal CC (yellow) and FOR (white).

Myelin Water Fraction v. Myelin Basic Protein Stain Intensity: Maternal Corpus Callosum, Maternal Fornix, Fetal Corpus Callosum & Fetal Fornix
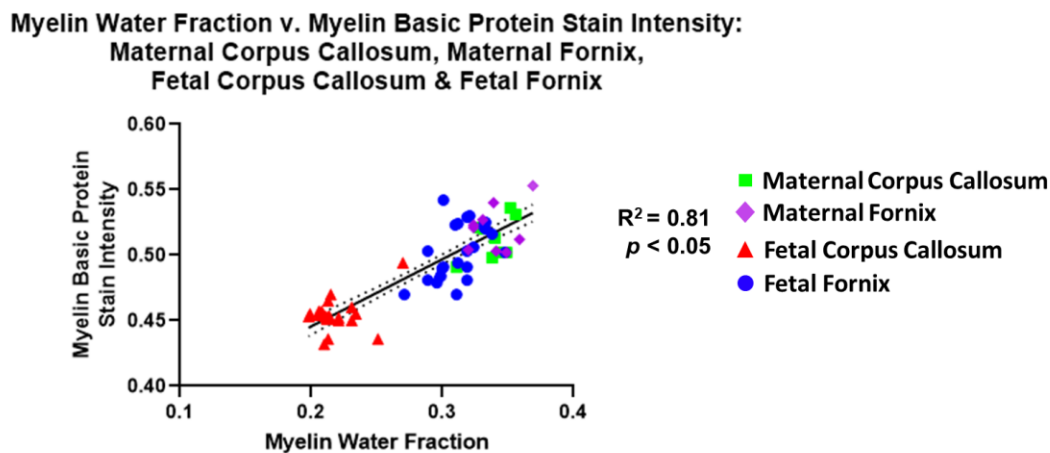
Figure 3.3. Linear regression line and 95% confidence intervals between MWF and MBP stain intensity of the maternal CC (light green squares), maternal FOR (purple diamonds), fetal CC (red triangles), and fetal FOR (blue circles). The mean MWF of the four regions correlates well with their respective region's mean MBP stain intensity (coefficient of determination, $R^2 = 0.81$).

The paired t-test showed significance for the following comparisons ($p < 0.0083$): maternal CC MWF and fetal CC mean MWF, and maternal CC MBP stain intensity and fetal CC mean MBP stain intensity (Figures 3.4A & 3.4B). The paired t-test did not show significance for the following comparisons: maternal FOR MWF and fetal FOR mean MWF, and maternal FOR MBP stain intensity and fetal FOR mean MBP stain intensity (Figures 3.4C & 3.4D). The ANOVA incorporating the linear mixed model showed that the mean MWF and mean MBP stain intensity of the fetal FOR were significantly greater than the mean MWF and mean MBP stain intensity of fetal CC, respectively (Figures 3.4E & 3.4F).

A **Myelin Water Fraction: Maternal Corpus Callosum v. Fetal Corpus Callosum**

B **Myelin Basic Protein Stain Intensity: Maternal Corpus Callosum v. Fetal Corpus Callosum**

C **Myelin Water Fraction: Maternal Fornix v. Fetal Fornix**

D **Myelin Basic Protein Stain Intensity: Maternal Fornix v. Fetal Fornix**

E **Myelin Water Fraction: Fetal Fornix v. Fetal Corpus Callosum**

F **Myelin Basic Protein Stain Intensity: Fetal Fornix v. Fetal Corpus Callosum**

Figure 3.4. Box-and-whisker plot of the **(A)** MWF and **(B)** MBP stain intensity of the maternal CC and fetal CC. The MWF and MBP stain intensity of the maternal CC was significantly higher than the mean MWF and mean MBP stain intensity of the fetal CC, respectively. Box-and-whisker plot of the **(C)** MWF and **(D)** MBP stain intensity of the maternal FOR and fetal FOR. Box-and-whisker plot of the **(E)** MWF and **(F)** MBP stain intensity of the fetal CC and fetal FOR. The MWF and MBP stain intensity of the fetal FOR was significantly higher than the MWF and MBP stain intensity of the fetal CC, respectively. The black asterisk (*) indicates that the *p*-value is less than 0.0083.

The simple linear regression and F-test showed significant associations between the following: BLWR v. fetal CC MBP stain intensity ($R^2 = 0.31$), BLWR v. fetal FOR MBP stain intensity ($R^2 = 0.13$), and BLVR v. fetal FOR MWF and BLVR ($R^2 = 0.41$) [Figures 3.5A & 3.5B]. There was no significant association between fetal CC MWF v. BLVR ($R^2 = 0.07$, $p = 0.15$) [Figure 3.5B]. The simple linear regression and F-test also showed that BLWR and BLVR correlated well ($R^2 = 0.97$).
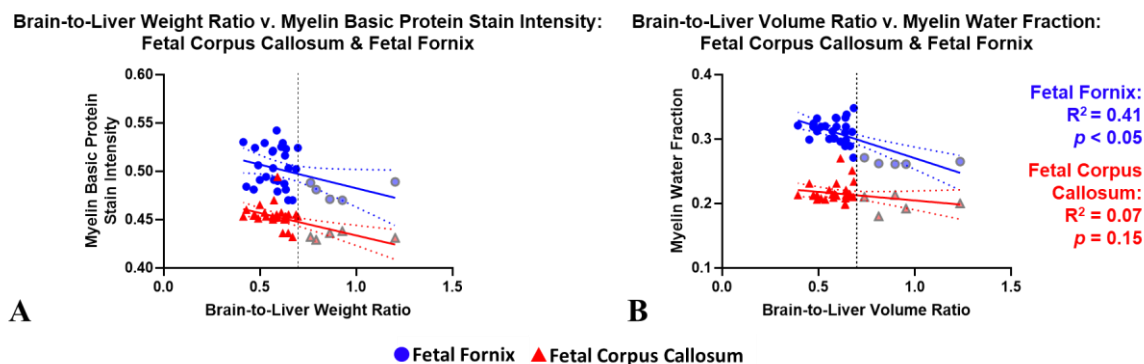
Figure 3.5. (A) Linear regression line and 95% confidence intervals between BLWR and MBP stain intensity of the fetal FOR (blue circles) and fetal CC (red triangles). The blue circles and red triangles that are semi-transparent with a grey outline represent the MBP stain intensity of the fetal FOR and fetal CC, respectively, of fetal guinea pigs with IUGR as determined by a BLWR ≥ 0.7. The coefficient of determination of BLWR with the MBP stain intensity of the two fetal regions are as follows: $R^2 = 0.13$, $p < 0.05$ (FOR) and $R^2 = 0.31$, $p < 0.05$ (CC). **(B)** Linear regression line and 95% confidence intervals between BLVR and MWF of the fetal FOR (blue circles) and fetal CC (red triangles). The blue circles and red triangles that are semi-transparent with a grey outline represent the MWF of the fetal FOR and fetal CC, respectively, of fetal guinea pigs with IUGR as determined by a BLVR ≥ 0.7. The coefficient of determination of BLVR with the MWF of the two fetal regions are as follows: $R^2 = 0.41$, $p < 0.05$ (FOR) and $R^2 = 0.07$, $p = 0.15$ (CC).

3.4   Discussion

This pilot study successfully generated MWF maps for all fetal guinea pig brains, thus, confirming the feasibility of conducting MWI in the fetal environment. We attempted to achieve the smallest voxel size possible within a reasonable time frame for the acquisition and reconstruction of the MWF maps; hence, two sets of acquisitions with different resolutions were acquired: one with 0.7 mm^3 and one with a varied resolution of 0.75 mm^3 – 0.9 mm^3. Ultimately, the DESPOT$_{1/2}$ volumes acquired with a 0.7 mm^3 isotropic resolution were ideal for analysis since the volumes were acquired in approximately 40 minutes and the MWF reconstruction took approximately 1 hour;

consequently, all the data reported was acquired from the 0.7 mm^3 scans. Higher resolution MWF maps were too noisy for analysis since verifying that the ROIs were transferred to the correct location from the T$_2$-weighted images to the MWF maps was challenging.

In addition to analyzing the MWF of fetal guinea pig brains, we also analyzed the MWF of the CC and FOR of the maternal brains for use as an internal control. The mean MWF value of the white matter of the CC of the maternal guinea pig brain was consistent with previously published MWF values of the CC in adult guinea big brains, supporting our fetal MWF results [287].

We chose to isolate and analyze the MWF of the fetal FOR and CC as these regions were the easiest to identify in the MWF maps and are typically associated with pathologies [162, 287]. Furthermore, MBP immunoreactivity in both the fetal FOR and CC in guinea pigs of the same GA have been previously analyzed and published, allowing comparisons to be made [162].

The fetal FOR mean MWF and mean MBP stain intensity were significantly greater than the mean MWF and mean MBP stain intensity of the fetal CC, respectively. Myelination in guinea pigs occurs in the FOR during the first half of gestation and in the CC during the latter half of gestation, suggesting that FOR myelin content should be higher than that of the CC and, hence, supporting these results [166]. These results were also consistent with previously published results from a study conducted by Piorkowska *et al.* where MBP immunohistochemistry in the fetal FOR was significantly greater than the fetal CC of guinea pigs of the same gestational age [162].

The guinea pig is an excellent animal model for neurologic developmental programming. Unlike rats and mice but like humans, guinea pigs are identified as prenatal brain developers since they are precocious developers and undergo rapid brain growth in the latter half of gestation [163, 164]. Furthermore, the most rapid phase of myelination is initiated in the latter half of pregnancy in humans and guinea pigs [165]. Although the guinea pig brain is larger relative to body size and at a more advanced stage of functionality at term than the human brain, intrauterine insults coincide with critical

periods of development, and the associated long-term outcomes can be more accurately extrapolated to humans [292].

Although the most common method to measure MWF is solely T_2-based, we used mcDESPOT since its acquisition times for human imaging are more appropriate for fetal imaging [114, 241]. Furthermore, mcDESPOT was previously used to generate MWF maps to assess the brain myelin content of both children and neonates, which are the two populations closest in age to fetuses [284, 292]. In addition, an assessment of normal fetal brain myelination has been conducted previously with MRI by quantifying the macromolecular proton fraction of different brain regions throughout gestation, suggesting sufficient amounts of myelination are present to be analyzed by MWI [293].

Finally, fetuses with a BLWR and BLVR $\geq$ 0.7 had IUGR as a result of brain sparing, a condition associated with placental dysfunction [294]. Preliminary analysis showed that the MWF and MBP stain intensities were lower in the fetal FOR & CC of the growth-restricted (BLWR and BLVR $\geq$ 0.7) fetuses. Given that IUGR was not the focus of this study and that we did not have the sufficient sample size to achieve the desired power, we did not directly compare the MWF and MBP stain intensity of growth-restricted fetuses with the normally grown fetuses due to the large discrepancy in sample size between the two groups. Nonetheless, multiple groups have also shown via MBP staining that growth-restricted fetal guinea pigs have a reduced myelin content compared to their non-growth-restricted counterparts, supporting our results [162]. Now that we have successfully demonstrated the use of MWI to assess fetal guinea pig brain myelin content and preliminary results have shown that MWF is lower in growth-restricted fetuses, the next step is to use MWI in a growth-restricted fetal guinea pig model for MWF comparison with non-growth-restricted fetal guinea pigs; the sample size should be 60 to achieve a power of 0.9. Furthermore, it was not surprising that BLWR and BLVR were found to correlate well, and both classified the same fetuses as IUGR, providing additional support that tissue volume quantification using MRI can help identify growth restriction *in utero*.

3.4.1 Limitations

Luxol Fast Blue (LFB) is a histological stain commonly used to assess myelin development and validate MWF maps. LFB staining is dependent on an acid-base reaction where the phthalocyanine dye is soluble in alcohol and attracted by bases in the myelin phospholipids [132]. Although LFB is an excellent stain for myelin in adult human and GP brains [133, 162, 283], this stain has shown immense variability when staining for myelin in fetal guinea pig brains. This staining variability is likely due to the fetal brains having a higher water content than adult brains, making the lipid content prone to variable and less stabilizing fixation in formalin [132, 137]. This makes it difficult to conduct "regressive stains," such as LFB, whose regression timing can differ for each type of sample [137]; hence, these stains do not tend to have a single protocol, which is not ideal for quantitative analysis and comparison. On the other hand, MBP immunohistochemistry is not a regressive stain and, hence, has a singular protocol. Since MBP in fetal brains was permanently stabilized via crosslinking, immunostaining produced less variability [137]. Furthermore, MBP immunohistochemistry has previously been used to validate MWF maps and as a marker of myelination in fetal guinea pig brains [162], making it an ideal stain for this study's histological validation.

Partial volume effects limit our MWF measurements. Although we only analyzed the regions that we could accurately identify in the MWF maps, a possibility still exists that the ROI placement extended outside the desired region due to its small size. Another limitation is the lack of assessment of inter-observer reproducibility. Although the guinea pigs were anesthetized, motion may have occurred between the T_2-weighted acquisition used for ROI placement and the $DESPOT_{1/2}$ acquisition used to generate the MWF maps. Hence, the ROIs may not have occupied the same voxels between the T_2-weighted image and the MWF map. In addition, it is possible that the placement of the ROIs on the MWF maps differs from those on the MBP stains. Due to the discrepancy in the slice thickness between the MWF maps and the MBP stains, the small size of the fetal structures, and the limited resolution of the MR images, the priority was to correctly identify the fetal structures, especially in the MWF maps.

The study also looked at a single time point in the gestational period that was chosen late in gestation since the amount of myelin in the brain would be at its highest for the fetal stage to image; the next step would be to image earlier in gestation to assess the development of myelin in different regions as a function of gestational age. Two additional limitations were the long acquisition times and the use of anesthesia for imaging, which will both need to be addressed when transitioning to human application. Since the use of anesthesia would not be an option when imaging pregnant participants, acquisition times for the DESPOT$_{1/2}$ scans would need to be reduced to mitigate both maternal and fetal motion, such as by reducing resolution and acquiring 2D instead of 3D images. Differences in myelination between sexes become noticeable after birth [292]; however, this study omitted sex as a variable in the analysis due to the low number of fetuses and the singular timepoint in gestation.

3.4.2 Conclusion

This study successfully demonstrated that MWI may be used to quantify MWF in the fetal guinea pig brain for assessment of brain myelin content, as validated using an immunohistological stain for MBP. MWF was found to correlate well with the MBP stain intensity of the analyzed regions.

CHAPTER 4

4 Quantifying Myelin Water Fraction in a Guinea Pig Model of Spontaneous Intrauterine Growth Restriction

4.1 Introduction

Intrauterine growth restriction (IUGR) is an obstetrical complication where a fetus exhibits diminished growth below its programmed genetic weight and size potential [51]. According to the World Health Organization, a fetus with IUGR has an estimated weight below the 10th percentile for their gestational age and a cut-off birth weight of 2500 grams at birth [69]. IUGR is a leading cause of perinatal morbidity and mortality, second only to prematurity [53]. The incidence of IUGR is estimated to be approximately 3-10% in the general obstetric population, although the incidence varies depending on the analyzed population, geographic location, and the standard growth curves used as a reference [295]. Most cases of IUGR are due to an inadequate supply of oxygen and nutrients to the fetus due to placental insufficiency [85].

The neurological consequences of IUGR manifest as early as one year of age and persist throughout adolescence into adulthood; these neurological effects range from reduced cognitive skills and learning disabilities to neurological disorders such as autism spectrum disorder and cerebral palsy [99]. The likelihood of the consequence depends on the insult's length, severity, and timing. A significant factor in the pathogenesis of these disabilities is white matter injury characterized by multiple factors, including impaired myelination. For example, a post-mortem study showed a notable decrease in myelin content between control newborn infants and those with IUGR [143].

Magnetic resonance imaging (MRI) is increasingly used for clinical and research purposes to assess fetal neurodevelopment [296]. Myelin water imaging (MWI) is an MRI-based technique that images the aqueous components associated with the myelin sheath, specifically myelin water and intra-/extra-cellular water, to quantify myelin water fraction (MWF) [114]. MWF is the ratio of the signal from myelin water to the signal

from both myelin and intra-/extra-cellular water and is validated as a strong marker for myelin lipid [114]. The feasibility of MWI in the fetal environment has been successfully demonstrated by quantifying MWF in a fetal guinea pig model [2]. The preliminary results from that work suggested that the MWF in the fetal corpus callosum and the fornix was lower in the fetuses with IUGR than in control fetuses [2].

This study builds on the pilot study quantifying the difference in MWF in various brain regions in a guinea pig model of spontaneous IUGR. Guinea pigs are an excellent model of neurologic developmental programming for humans and, like humans, develop spontaneous IUGR due to litter variations [155-157, 163, 165].

This study aims to determine whether MWF in various fetal brain regions differs in fetal guinea pigs with spontaneous IUGR compared to control guinea pigs. We hypothesize that MWF would be lower in the fetuses with IUGR than those without IUGR.

4.2   Materials and Methods

The institution's Animal Care and Ethics Committee reviewed, approved, and monitored the imaging protocol. The sample consisted of twenty-two pregnant, chow-fed female in-house bred Dunkin-Hartley guinea pigs (Charles River Laboratories) late in gestation (59-64 days gestation, term = ~68 days) with a total of 73 fetuses. A spontaneous model of IUGR was used where IUGR occurred naturally without artificial interventions.

4.2.1   Imaging

Before imaging, the guinea pigs were induced with 4.5% isoflurane with 2 litres/minute O_2 and maintained via nose cone with a 1.5-2.5% isoflurane with 2 litres/minute O_2. All imaging was performed with a 3.0 T MRI scanner (Discovery MR750, GE Healthcare, Waukesha, WI) with a 32-element human cardiac coil array (In Vivo Corp., Gainesville, FL). Anatomical T_2-weighted ^1H images of the entire uterus, including all fetal guinea pig brains, were acquired with a 3D spin-echo sequence: repetition time (TR)/echo time (TE): 2002/218 ms, NEX: 2, field of view (FOV): 10-12 cm, voxel size: 0.6 x 0.6 x 0.6 mm; the T_2-weighted acquisition was approximately 10 minutes long.

Eight spoiled gradient echo (SPGR) volumes (TR/TE: 6.50/3.03 ms) for driven equilibrium single pulse observation of T_1 (DESPOT$_1$) were acquired at varying flip angles (α: 2° – 16°, increasing increments of 2°) in one acquisition [209]. Two sets of eight balanced steady-state free precession (bSSFP) volumes (TR/TE: 6.7/3.4 ms) for DESPOT$_2$ were acquired at various flip angles (α: 8° – 64°, increasing increments of 8°) and at 0° and 180° phase increments in a separate, single acquisition [209]. The eight DESPOT$_1$ and 16 DESPOT$_2$ volumes were acquired in approximately 13 and 30 minutes, respectively [209]. All DESPOT$_{1/2}$ acquisitions had the following imaging parameters: NEX: 1, FOV: 10-12 cm, voxel size: 0.6 x 0.6 x 0.6 mm, acceleration factor: 2x [ASSET (DESPOT$_1$) & ARC (DESPOT$_2$)].

After imaging, the sows were monitored and kept on O_2 until awake. The sows were transferred to be kept under a heating lamp and monitored until they were fully awake and mobile. The sows were then returned to their cages.

4.2.2   MWF Map Reconstruction and MWF Quantification

Masks of the fetal guinea pig brains were manually generated from the T_2-weighted images using FSLeyes [285]**.** Using quantitative Imaging Tools [286], multi-component DESPOT$_{1/2}$ (mcDESPOT) was used to reconstruct the MWF maps of each fetal guinea pig's brain [241].

3D Slicer (v. 4.11.0-2019-12-02) [265-267] was used to place four to six regions of interest (ROIs) with a diameter of 0.5 mm and 1-2 pixels in the corpus callosum (CC), fornix (FOR) and parasagittal white matter (PSW) of each fetal guinea pig brain. The ROIs were placed on the T_2-weighted images and then transferred to the MWF maps to quantity the regions' MWF values. Images from Sethi *et al.* and Gareau *et al.* were used for reference to identify the CC with the FOR and PSW located below and above the CC, respectively [2, 287]. The ROIs placements were done blinded and prior to IUGR determination.

4.2.3   Animal Collection

The maternal sows were euthanized via CO_2 inhalation 2-3 days after imaging (61-66 days gestation) [289]. All fetuses were removed from the sow, confirmed dead, and weighed immediately. Fetal brains, fetal livers, and placentae were removed and weighed immediately. The following IUGR weight markers and their IUGR cut-off values are commonly used in literature for IUGR determination: body weight (BW), body weight of each fetus to the average weight of the fetuses within the pregnancy ratio (BPrWR), brain-to-liver weight ratio (BLWR), brain-to-placenta weight ratio (BPlWR), and brain-to-body weight ratio (BBWR) [64, 67-70]. The IUGR cut-off value for each marker is as follows: BW ≤ 85 grams, BPrWR ≤ 0.9, BLWR ≥ 0.6, BPlWR ≥ 0.6, and BBWR ≥ 0.03.

4.2.4   IUGR Determination

Although weight markers are commonly used in animal studies for IUGR determination, this study employed each weight marker's corresponding volume marker instead for human translational purposes. Furthermore, the demonstration of the strong correlation between weight and volume, as determined by MRI in Chapter 3, provided further support for using volume markers. Hence, fetal body, brain, liver, and placental volumes were quantified using the T_2-weighted images. The corresponding five fetal volume markers were quantified for IUGR determination: body volume (BV), body volume of each fetus relative to the average volume of the fetuses within the pregnancy ratio (BPrVR), brain-to-liver volume ratio (BLVR), brain-to-placenta volume ratio (BPlVR), and brain-to-body volume ratio (BBVR).

Linear regression was performed between each volume marker and its respective weight marker to acquire the linear equation describing the correlation between a volume and its respective weight marker, resulting in five different linear equations. The IUGR cut-off value for each volume marker was then calculated using the above-mentioned IUGR cut-off value for its respective weight marker and the respective linear equation. For instance, the BV cut-off value was calculated using the BW cut-off value, i.e., 85 grams, and the linear equation describing the correlation between BW and BV. The calculated IUGR

cut-off values for the volume markers are as follows: BV $\leq$ 37 cm^3, BPrVR $\leq$ 0.9, BLVR $\geq$ 0.6, BPlVR $\geq$ 0.42, and BBVR $\geq$ 0.068. A fetus was determined to have IUGR if it met at least three of the five volume markers.

4.2.5   Statistical Analysis

A simple linear regression analysis was performed between the following for all three regions separately: BV v. MWF, BPrVR v. MWF, BLVR v. MWF, BPlVR v. MWF, and BBVR v. MWF. F-tests were also conducted to determine if the slopes of the above-mentioned comparisons for all three regions were significantly different from zero (α = 0.05). Incorporating a linear mixed model, a one-way analysis of variance (ANOVA) was performed to compare the mean MWF of IUGR and non-IUGR fetuses for all three analyzed regions separately, with the sex of the fetus being a co-variate (α = 0.05). The linear mixed model was incorporated to consider litter effects as fetuses within a litter experience genetic and environmental similarities and, hence, are not independent [297].

The one-way ANOVA analysis incorporating the linear mixed model was performed using RStudio Team (2020). RStudio: Integrated Development for R. RStudio, PBC, Boston, MA URL http://www.rstudio.com/. The simple linear regression analysis and F-tests were performed using GraphPad Prism version 9.3.1 for Windows, GraphPad Software, San Diego, California, USA, www.graphpad.com.

4.3   Results

No adverse events occurred in the maternal guinea pigs during imaging. MWF maps were successfully generated for each fetal guinea pig's brain. Two of the 73 fetal guinea pigs imaged were deceased at collection; data from those two fetuses were excluded. Of the 71 fetal guinea pigs analyzed, 19 were determined to have IUGR as determined by meeting at least three of the five criteria, comprising 27% of the sample (Tables 1 & 2).

Table 4.1. Characteristics of Fetal Guinea Pigs

Characteristic	Non-IUGR ($N = 52$)	IUGR ($N = 19$)
Sex of Fetus		
Male	22	12
Female	30	7
Body Volume		
$\leq 37 \text{ cm}^3$	3	12
$> 37 \text{ cm}^3$	49	7
Body-to-Pregnancy Volume Ratio		
≤ 0.9	1	8
> 0.9	51	11
Brain-to-Liver Volume Ratio		
≥ 0.6	7	19
< 0.6	45	0
Brain-to-Placenta Volume Ratio		
≥ 0.42	11	16
< 0.42	41	3
Brain-to-Body Volume Ratio		
≥ 0.068	4	16
< 0.068	48	3

Table 4.2. Distribution of Fetal Guinea Pigs Within Maternal Guinea Pigs

Maternal Guinea Pig	Non-IUGR ($N = 52$)	IUGR ($N = 19$)
1	1	0
2	1	2
3	3	2
4	3	0
5	2	2
6	2	0
7	3	1
8	2	0
9	1	2
10	2	1
11	3	0
12	1	2
13	3	0
14	4	0
15	4	0
16	3	1
17	4	1
18	3	2
19	3	0
20	0	2
21	2	1
22	2	0

Note. – Maternal guinea pig #22 had two fetuses that were deceased before collection and are not reported in the table.

The one-way ANOVA showed the mean MWF of the IUGR guinea pigs to be significantly lower than the mean MWF of non-IUGR guinea pigs for all three regions ($p < 0.05$) [Figures 1 & 2].
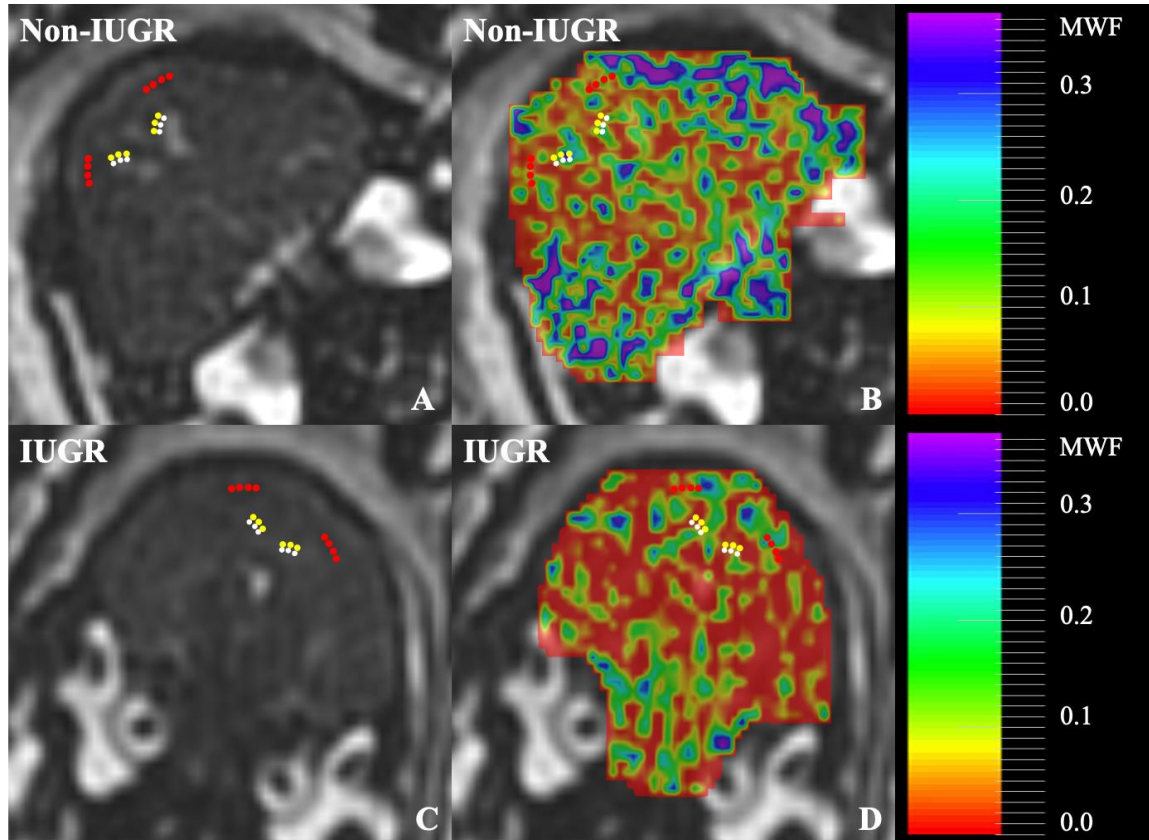
Figure 4.1. (A) Coronal T$_2$-weighted image of a fetal guinea pig brain with no intrauterine growth restriction (IUGR) at 62 days gestation. **(B)** A 50% transparent myelin water fraction (MWF) map of the same guinea pig brain overlaid on the corresponding anatomical image shown in A. The fetus did not meet any of the IUGR criteria. **(C)** Coronal T$_2$-weighted image of a fetal guinea pig brain with IUGR at 61 days gestation. **(D)** A 50% transparent MWF map of the same guinea pig brain overlaid on the corresponding anatomical image in C. The fetus met four of the five IUGR criteria. A colour scale for the MWF maps is shown for reference. In all four figures, regions of interest are placed in the CC (yellow), FOR (white), and PSW (red).
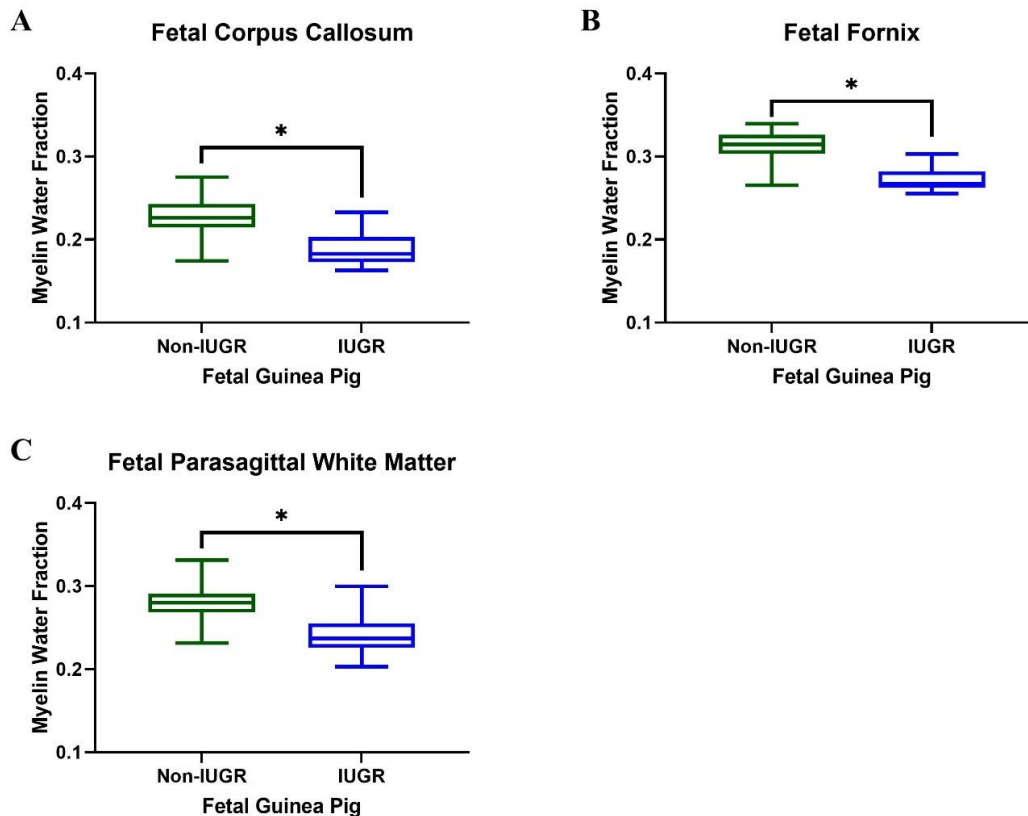
Figure 4.2. Box-and-whisker plot comparing the mean MWF of non-IUGR and IUGR fetal guinea pigs in the **(A)** CC, **(B)** FOR, and **(C)** PSW. The guinea pigs comprising the IUGR group met three or more of the five IUGR criteria. The guinea pigs comprising the non-IUGR group met two, one or zero of the five IUGR criteria. In all three regions, the mean MWF of the IUGR group was significantly lower than the mean MWF of the non-IUGR group, indicated by the black asterisk (*) [$p < 0.05$].

The simple regression results for all three regions between MWF and each IUGR volume marker are shown in the following figures: BV v. MWF (Figure 3), BPrVR v. MWF (Figure 4), BLVR v. MWF (Figure 5), BPlVR v. MWF (Figure 6), and BBVR v. MWF (Figure 7). The F-test results showed that the slope between MWF and each IUGR volume marker for every region analyzed significantly differed from zero ($p < 0.05$).
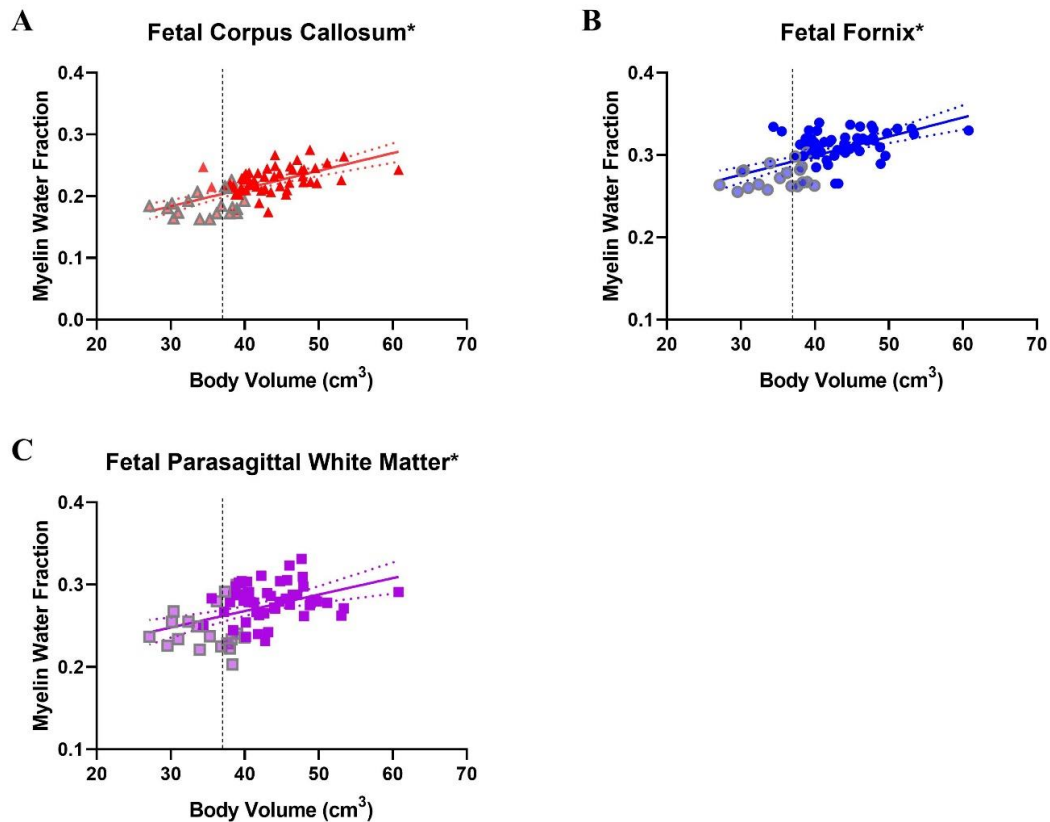
Figure 4.3. Linear regression line and 95% confidence intervals between BV and MWF of fetal guinea pigs' **(A)** CC (red triangles), **(B)** FOR (blue circles), and **(C)** PSW (purple squares). The black dotted vertical line in all three graphs indicates the cut-off point for IUGR classification of a BV ≤ 37 cm^3. The red triangles, blue circles, and purple squares that are semi-transparent with a grey outline represent the MWF of the CC, FOR, and PSW, respectively, of the fetal guinea pigs with IUGR as determined by the IUGR criterion. The coefficient of determination (R^2) of BV with MWF of the three fetal regions are as follows: 0.42 (CC), 0.35 (FOR), and 0.20 (PSW). A black asterisk (*) indicates that the slope of the line is significantly different from zero as determined by an F-test ($p < 0.05$).
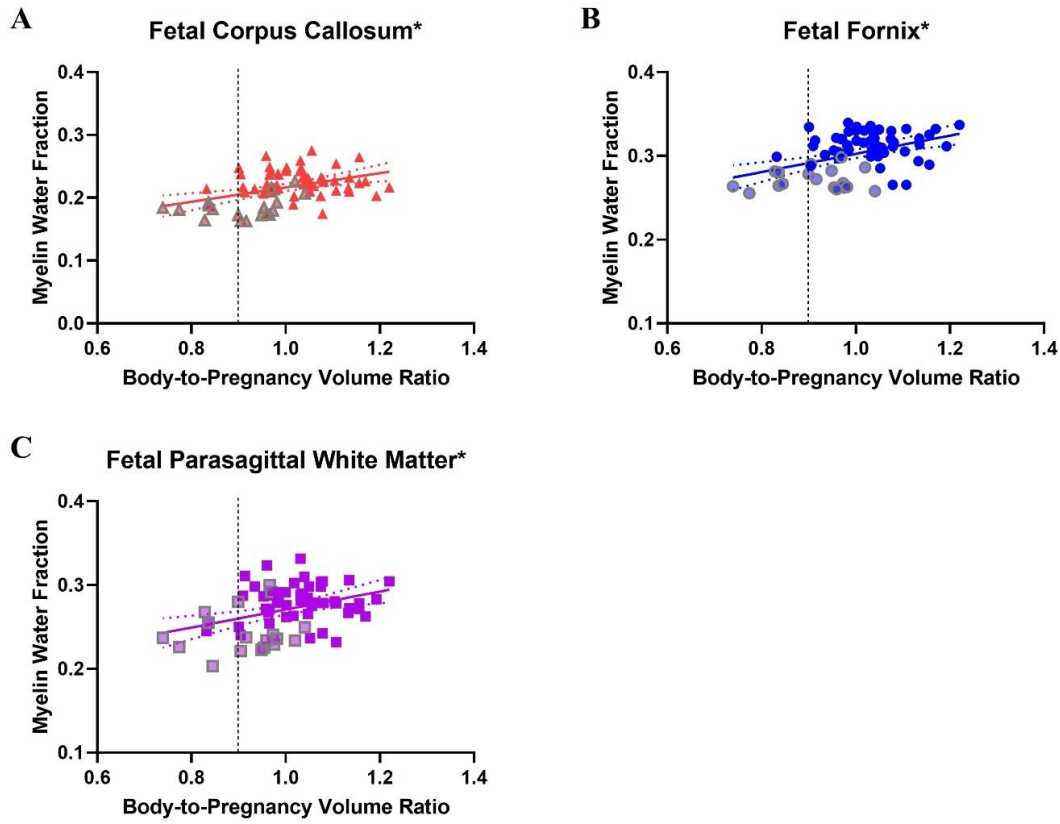
Figure 4.4. Linear regression line and 95% confidence intervals between BV and MWF of fetal guinea pigs' **(A)** CC (red triangles), **(B)** FOR (blue circles), and **(C)** PSW (purple squares). The black dotted vertical line in all three panels indicates the cut-off point for IUGR classification. of a BPrVR ≤ 0.9. The red triangles, blue circles, and purple squares that are semi-transparent with a grey outline represent the MWF of the CC, FOR, and PSW, respectively, of the fetal guinea pigs with IUGR as determined by a set criterion. The coefficient of determination (R^2) of MWF of the three fetal regions with BPrVR are as follows: 0.17 (CC), 0.20 (FOR), and 0.14 (PSW). A black asterisk (*) indicates that the slope of the line is significantly different from zero as determined by an F-test ($p < 0.05$).
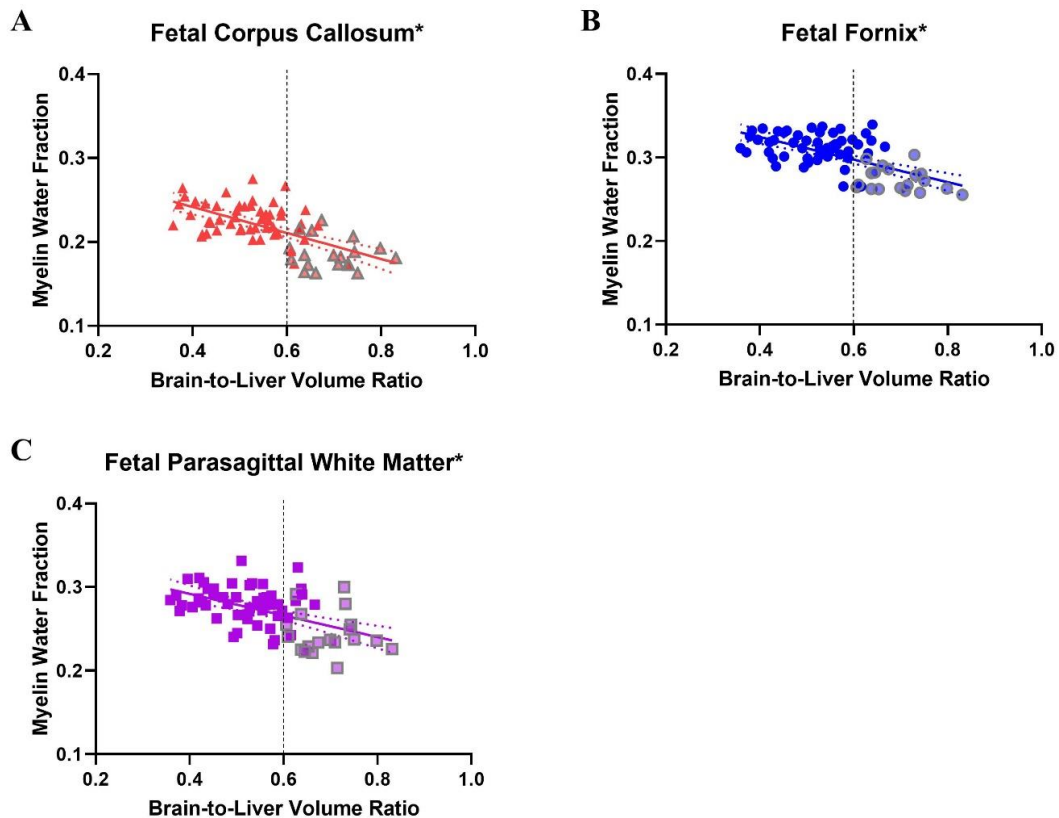
Figure 4.5. Linear regression line and 95% confidence intervals between BLVR and MWF of fetal guinea pigs' **(A)** CC (red triangles), **(B)** FOR (purple squares), and **(C)** PSW (blue circles). The black dotted vertical line in all three panels indicates the cut-off point for IUGR of a BLVR $\geq$ 0.6. The red triangles, purple squares, and blue circles that are semi-transparent with a grey outline represent the MWF of the CC, FOR, and PSW, respectively, of the fetal guinea pigs with IUGR as determined by a set criterion. The coefficient of determination (R^2) of MWF of the three fetal regions with BLVR are as follows: 0.40 (CC), 0.38 (FOR), and 0.27 (PSW). A black asterisk (*) indicates that the slope of the line is significantly different from zero as determined by an F-test ($p < 0.05$).
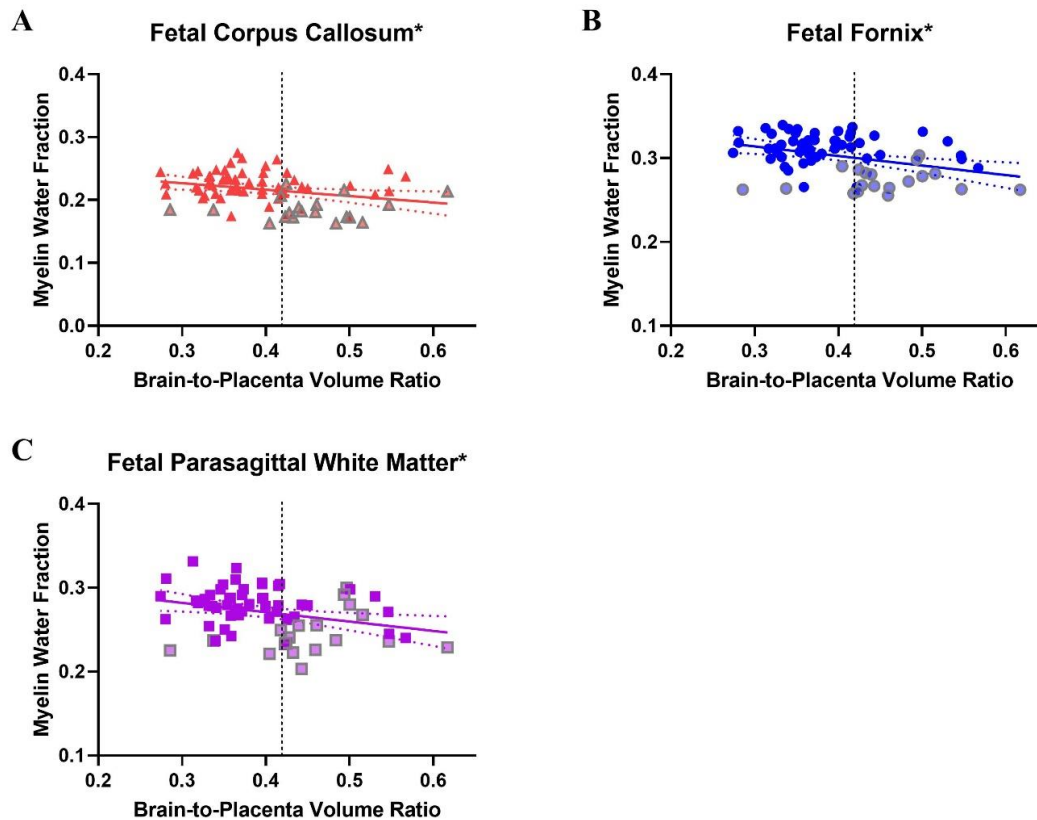
Figure 4.6. Linear regression line and 95% confidence intervals between BPlVR and MWF of fetal guinea pigs' **(A)** CC (red triangles), **(B)** FOR (blue circles), and **(C)** PSW (purple circles). The black dotted vertical line in all three panels indicates the cut-off point for IUGR) classification of a BPlVR ≥ 0.42. The red triangles, blue circles, and purple circles that are semi-transparent with a grey outline represent MWF of the CC, FOR, and PSW, respectively, of the fetal guinea pigs with IUGR as determined by a set criterion. The coefficient of determination (R^2) of MWF of the three fetal regions with BPlVR are as follows: 0.08 (CC), 0.13 (FOR), and 0.09 (PSW). A black asterisk (*) indicates that the slope of the line is significantly different from zero as determined by an F-test ($p < 0.05$).
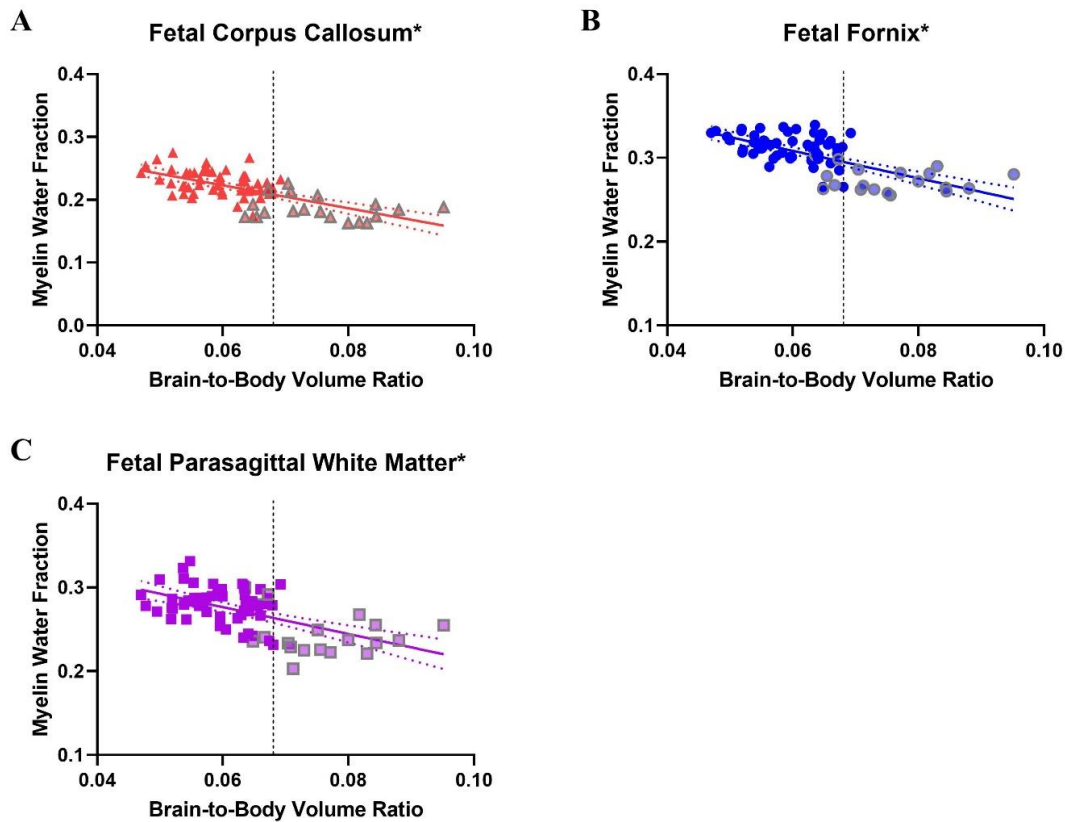
Figure 4.7. Linear regression line and 95% confidence intervals between BBVR and MWF of fetal guinea pigs' **(A)** CC (red triangles), **(B)** FOR (blue circles), and **(C)** PSW (purple squares). The black dotted vertical line in all three panels indicates the cut-off point for IUGR classification of a BBVR ≥ 0.068. The red triangles, blue circles, and purple squares that are semi-transparent with a grey outline represent MWF of the CC, FOR, and PSW, respectively, of the fetal guinea pigs with IUGR as determined by a set criterion. The coefficient of determination (R^2) of MWF of the three fetal regions with BBVR are as follows: 0.45 (CC), 0.47 (FOR), and 0.34 (PSW). A black asterisk (*) indicates that the slope of the line is significantly different from zero as determined by an F-test ($p < 0.05$).

4.4   Discussion

This study quantified and compared MWF in the brains of fetal guinea pigs with and without IUGR. In all three regions analyzed – CC, FOR, and PSW – the MWF was significantly lower in the guinea pigs with IUGR. This study also determined the correlation between the MWF of all three regions with the IUGR markers of BV, BPrVR, BLVR, BPlVR, and BBVR. All three regions were found to have the highest correlations with BBVR, and all had the lowest correlations with BPlVR.

Among the non-IUGR and IUGR fetuses, the FOR had the highest MWF, with the PSW being second and the CC having the least. These results are consistent with previously published results where MBP staining was the highest in the FOR, second in the PSW, and the lowest in the CC in guinea pigs of the same gestational age, supporting our results [162]. In guinea pigs, myelination begins in the first half of gestation in the FOR and the second half in the CC [166]. The largest difference in mean MWF between non-IUGR and IUGR guinea pigs was in the CC, followed by the PSW and then the FOR.

Like the feasibility study, this study employed mcDESPOT as the technique for MWI. Hence, this study's imaging protocol was based on the protocol in the feasibility study, with the main difference being a decrease in voxel size to 0.6 mm^3 from 0.7 mm^2 [2]. Since this study looked at fetal and not maternal brains, the decrease in the field of view to only the uterus allowed increased resolution and improved identification of fetal brain structures. Consequently, we could identify and include the analysis for the PSW, whose myelin content is affected by IUGR as validated by histology, instead of just analyzing the CC and FOR, which was the case in the feasibility study [2]. Since MWI was already conducted in fetal guinea pigs, this study continued to use this animal model, especially since the decrease in brain myelin content from IUGR was previously demonstrated in fetal guinea pigs of the same gestational age [2, 162].

In previous animal studies, IUGR was found to be induced using models of maternal malnutrition, chronic hypoxia, and endocrine alterations to mimic the human conditions that can induce IUGR [150]. A common technique to induce IUGR is uterine artery

ligation (UAL) [298]. Although its effects are evident within hours of the procedure, this surgery has numerous limitations and is not guaranteed to induce IUGR as collateral blood flow can compensate to meet the fetus' growth requirements [152-154]. Guinea pigs can also demonstrate spontaneous IUGR due to their large litter sizes, and this model has been successfully used in other studies [155-157]. Hence, this study opted for the spontaneously occurring IUGR model, with cases of placental insufficiency occurring naturally in the population similar to humans.

BW, BPrWR, BLWR, BPlWR, and BBWR have all been previously used in clinical and animal studies as markers for IUGR [64, 67-70]. Instead of using weight markers, the study employed the volume equivalent of these markers for clinical translation purposes. Since IUGR fetuses weigh below the 10th percentile, BV is used as a marker for IUGR. BPrVR is also used because, in the majority of pregnancies with IUGR fetuses in our sample, not every fetus within the pregnancy has IUGR. Among the remaining three volume markers, the common denominator is the brain. IUGR fetuses have a higher value for these markers than non-IUGR fetuses due to a phenomenon called brain sparing. In situations of hypoxia and nutrient deprivation, such as in the case of IUGR, the fetus redistributes its cardiac output to maximize oxygen and nutrient supply to the brain [294]. The fetus does this by vasoconstricting the peripheral vascular beds and vasodilating the cerebral arteries so that the cardiac output favours the left ventricle. Since the left ventricle supplies blood to the upper body and brain, blood supply towards the brain is enhanced while supply to the organs in the lower half, such as the liver, is reduced due to the constriction of the peripheral vascular beds [299, 300]. Consequently, the brain is proportionally larger than other organs in IUGR fetuses than in non-IUGR fetuses. Since most cases of IUGR are due to placental insufficiency, the placenta is likely to be proportionally smaller in volume, along with impaired function [61, 85].

As previously mentioned, the MWF of guinea pigs with IUGR was significantly lower than control guinea pigs in all three regions. Similar results have been observed in humans and guinea pigs, as validated by histology [143, 162]. The mechanism behind the IUGR-related myelin reduction is likely due to the chronic hypoxia and oxidative stress of IUGR [301]. Both effects are known to inhibit oligodendrocyte differentiation and,

hence, myelination. Oligodendrocyte differentiation is controlled by a combination of inductive and repressive factors, with the main one being bone morphogenetic proteins (BMPs) [145-147]. Of the 20 BMPs, BMP4 has the most significant role in inhibiting oligodendrocyte differentiation, especially as oligodendrocyte precursors are particularly vulnerable to oxidative stress due to their low endogenous glutathione levels, high iron content, and high oxidative metabolism [144, 147, 148]. Elevated BMP4 signalling has been demonstrated in multiple animal models of IUGR. Thus, it is likely that increased BMP4 signalling due to the hypoxic environment of IUGR leads to a decrease in oligodendrocyte differentiation and, hence, myelination.

Although the weight and volume markers for IUGR are used clinically, they are not always perfect in identifying growth-restricted fetuses. IUGR often manifests in small for gestational age fetuses that weigh below the 10th percentile; however, some fetuses are genetically programmed to be small and, hence, are just small for gestational age but not growth-restricted. Conversely, some fetuses above the 10th percentile for weight are not growing to their prescribed genetic potential and are growth-restricted. Although not meeting the classical definition of IUGR, this group is still negatively impacted neurologically, as evidenced in Burger *et al.* where birth weight was found to positively correlate with educational performance at 12 years of age [108]. The ratios involving the brain are better identifiers for IUGR than just weight and/or volume alone due to brain sparing, but they are also not perfect markers for IUGR. One of the benefits of using MWF as a marker for IUGR is that it is a functional marker. As previously mentioned, one of the neurological consequences of IUGR is a reduction in brain myelin content. Since myelin content is independent of size, myelin content should be reduced in IUGR fetuses whether the fetal weight falls below the 10th percentile. The use of MRI, in conjunction with ultrasound, to assess fetal development is increasing in frequency, allowing the IUGR-related reduction in myelin content to be quantified along with the already established weight markers. In short, the established size markers for IUGR are easily accessible and work well. However, we can use functional markers like MWF alongside size markers to better identify true IUGR fetuses.

4.4.1   Limitations

The study had multiple limitations, with the first being partial volume affecting our MWF measurements. Due to the small features of the analyzed regions, a possibility exists that the ROI placement extended outside the desired region due to its small size. Although the number of ROIs placed in each region varied between animals to ensure the ROIs were only being placed in the desired region, the limitation was likely not completely avoided. Furthermore, this study lacked inter-rater reliability as only one individual conducted the ROI placement and the tissue segmentations. Another limitation is motion between the T_2-weighted acquisition used for ROI placement and the DESPOT$_{1/2}$ acquisitions used to generate the MWF maps. Hence, the ROI may not have occupied the same voxels between the T_2-weighted image and the MWF map. The study only looked at the development of myelin in IUGR late in gestation; the next step would be to image earlier in gestation and determine whether IUGR-related reductions can be identified and assessed earlier in gestation. Although the acquisition time for the DESPOT$_{1/2}$ volumes was reduced compared to the feasibility study [2], the acquisition times are still substantially long. They must be dramatically reduced when transitioning to human fetal imaging, especially since using anaesthesia for human imaging would not be an option.

4.4.2   Conclusion

This study showed that MWF is reduced in the CC, FOR, and PSW in fetal guinea pigs with IUGR compared to non-IUGR fetuses. The correlations between each IUGR marker and MWF was significant in all three regions as BBVR and BPlVR had the strongest and weakest correlations, respectively.

CHAPTER 5

5 Conclusions

5.1 Thesis Summary

The thesis demonstrates the successful use of MR relaxometry and MWI, an extension of MR relaxometry, in the fetal environment. Relaxometry isolates the contributions of individual contrast mechanisms and generates maps, which have a physical interpretation often expressed in absolute units. Now that fetal tissue relaxation times are quantified, they can provide an unbiased metric for comparing MR images and use the relationships between the contrast mechanisms and physiology to provide an *in utero* surrogate for biopsy and histology. The successful use of MR relaxometry to quantify T_1 and T_2^* relaxation parameters of various fetal tissues as a function of GA in the third trimester was first made in Chapter 2. In addition to demonstrating the feasibility of MR relaxometry in the fetal environment, the study showed that the T_1 relaxation times of the analyzed tissues do not vary with GA, while only the T_2^* of the fetal spleen, liver and muscle vary in the third trimester. It is important to note that the relaxation times were quantified as a function of GA, which is an important variable to consider in fetal research, as fetal development is a dynamic process. Although the relaxation times did not significantly vary in the third trimester, they will likely change earlier in the gestational period when tissues differentiate and develop.

As opposed to solely quantifying fetal tissue relaxation times, relaxometry can also be used to quantify biological parameters, such as myelin content. Myelination is integral to the normal functioning of the human brain and begins in the fetal stage. Fetal myelination has always been an area of interest not only for analyzing fetal neurodevelopment but also to understand the effect of pathology on the fetal brain, including IUGR. Although ultrasound is the standard imaging modality for assessing fetal development, it cannot visualize fetal myelin. Fortunately, we can visualize and quantify myelin content with MRI and relaxometry. In Chapter 3, MR relaxometry was taken a step further in MWI, where the T_1 and T_2 relaxation times of both myelin and intra-/extra-cellular water were

used to quantify MWF to assess myelin brain content in a guinea pig model late in gestation. The work presented in Chapter 3 is likely the first-recorded successful demonstration of MWI in the fetal environment. Following the successful completion of the work in Chapter 3, MWI was applied in an IUGR guinea pig model to show that IUGR-related reduction in brain myelin *in utero* for the first time, as demonstrated in Chapter 4.

IUGR has numerous consequences on fetal neurodevelopment, including impaired fetal myelination, and MRI is an excellent modality to assess this impairment non-invasively *in utero,* as demonstrated in Chapter 4. Although the primary focus of Chapter 3 was to demonstrate the feasibility of MWI in the fetal environment, preliminary results from the study showed decreased brain MWF in fetal guinea pigs with IUGR. Following these promising results, a study designated to assess and quantify differences in brain MWF between non-IUGR and IUGR guinea pigs was designed. The results of this study show that MWF is reduced in various brain regions in IUGR guinea pigs when compared to non-IUGR guinea pigs, which is presented in Chapter 4. This is especially important for assessing the utility of MWF as a functional marker for IUGR.

Overall, this thesis demonstrates the use of *in utero* MR relaxometry for fetal tissue development late in gestation. Relaxometry was first used to provide insight into fetal tissue development in uncomplicated pregnancies late in gestation. Following the successful completion of this work, an extension of relaxometry – MWI – was used to quantify MWF in the fetal brain to assess myelin content in first a control and then a growth-restricted population. Although MRI was first used to visualize the pregnant anatomy in 1983 and is being increasingly used to image the fetal environment, its applications to fetal development in a clinical environment are still limited due to its high cost and low accessibility; however, the presented work shows MRI's, particularly MR relaxometry's, capability to provide structural and functional information about fetal tissue development non-invasively.

5.2 Thesis Significance and Impact

The work described in Chapter 2 showed the quantification of various fetal tissues' T_1 and T_2^* relaxation times as a function of GA in uncomplicated pregnancies in the third trimester at 1.5 T. To our knowledge, this work was the first demonstration of quantifying fetal tissue relaxation times as a function of GA. These tissues can provide insight into fetal tissue development by providing information related to tissue microstructure and how they potentially can change throughout late gestation. Furthermore, quantifying tissue relaxation times can improve the comparison of fetal MR images longitudinally and between individuals to make better-informed decisions when choosing parameters for fetal imaging.

Chapter 3 demonstrates, for the first time, the conduction of MWI in the fetal environment. Since human myelination begins during fetal development, assessing myelin *in utero* can provide insight into fetal neurodevelopment and the changes in myelination due to pathology. Furthermore, the successful completion of this work further highlights the benefits of MRI in assessing fetal neurodevelopment, specifically fetal myelination.

The findings presented in Chapter 4 further show that myelination is reduced in fetuses with IUGR. Although this finding has already been published in humans and guinea pigs, it has been determined and validated only through post-mortem histology and staining [143, 162]. On the other hand, the work in Chapter 4 has not only shown the difference in myelin content but also quantified the difference non-invasively *in utero*. This work will especially be useful in identifying fetuses impaired by placental insufficiency but do not meet the conventional makers for IUGR. The ideal next step of this work is to potentially determine a cut-off value and further investigate the utility of MWF as a functional marker for IUGR.

In summary, the work presented in this thesis demonstrates the benefits of using MR relaxometry to assess fetal tissue development throughout late gestation. MR relaxometry was first used to quantify fetal tissue relaxation times before assessing fetal myelination

in an IUGR model. Hopefully, this work inspires further use of MR relaxometry and MWI in the fetal environment.

5.3   Future Directions

5.3.1   Studies at Different Time Points in Pregnancy

As detailed in the introductory chapter of the thesis, fetal development is a significant period of human tissue development that prepares the fetus to survive outside the uterus. Due to this period of rapid development, it is important to conduct the studies at different points in pregnancy. The work presented in Chapters 2, 3, and 4 was conducted late in pregnancy for different reasons. Chapter 2 looked at the third trimester because subcutaneous AT undergoes rapid development mid-late gestation, and these changes can be detected by MRI [269]. The relaxation times of the remaining analyzed tissues did not vary during the studied gestational period as these tissues became well-differentiated before the third trimester. Hence, it is important to quantify their relaxation times earlier in pregnancy to acquire more information about their structural and functional development. Furthermore, all the reasons for quantifying fetal tissue relaxation times, including longitudinal and cross-sectional comparison, improving imaging parameters, and identifying pathology, are valid for all time points in pregnancy and not just the third trimester.

As indicated in Chapters 3 and 4, MWF was quantified late in gestation in guinea pigs because we wanted to maximize the chances of acquiring sufficient SNR to image myelin as myelin content would be the greatest at that time point in pregnancy. Furthermore, differences in myelination due to IUGR would be most evident late in gestation due to the prolonged duration of the insult; however, if myelin is to be used as a functional marker of IUGR, it is important to quantify myelin earlier in gestation to determine at what point the IUGR-related reduction in myelin first becomes evident and potentially determine a cut-off point for IUGR. Hopefully, with this information, clinicians can determine the appropriate prognosis for the affected fetus.

5.3.2   Translation to Human Studies

The population in Chapter 2 was pregnant women with uncomplicated pregnancies in their third trimester. Although the intention is to conduct MWI in humans eventually, there were some reasons why an animal model was used instead for the work presented in Chapters 3 and 4. Firstly, the protocol has a prolonged acquisition time, which is not feasible for fetal imaging as it is not ideal to have pregnant women be scanned for long periods. Furthermore, anesthesia is not an option for pregnant women, making fetal motion a challenge. The protocol in Chapter 2 consisted of two 16-20 second breath-hold acquisitions. Even so, a few acquisitions had to be repeated due to motion from the mother or the fetus. Hence, running a protocol that takes 40-50 minutes without anesthesia will be extremely challenging, making an animal model ideal.

In addition to the challenges with human fetal imaging as described above, there are numerous benefits of using the guinea pig as the animal model, which were discussed in the introductory chapter; however, there are also disadvantages of using a guinea pig model, such as a smaller brain relative to humans. Although the guinea pig is a great model for studying neurologic developmental programming because they are intelligent developers and undergo rapid myelination in the latter half of gestation like humans [163-165], there are some physiological differences compared to humans. For instance, guinea pigs tend to carry multiple fetuses per pregnancy, while humans typically have one fetus per pregnancy, which may result in differences in the allocation of nutrients and oxygen during gestation [168]. Also, the guinea pig brain is at a more advanced stage of functionality at term than the human brain, making the outcomes of intrauterine insults more pronounced in guinea pigs than in humans [292]. Guinea pig and human placentas share similarities, such as a discoidal, haemomonochorial structure and fetal/maternal transport barrier; however, despite these similarities between the two placental structures, there are differences, such as the guinea pig's labyrinthine structure that facilitates more effective oxygen and nutrient exchange compared to the human placenta [164, 168].

The eventual goal of this work is to apply MWI in humans to acquire more accurate information on human *in utero* myelination and to use myelin as a potential identifier of

fetuses with IUGR. The animal experiments discussed in Chapters 3 and 4 were performed using a commercial clinical 3.0 T MRI, simplifying translation to humans. MWI has also been successfully conducted in clinical studies to assess and quantify MWF in adults, young adults, children, and neonates, showcasing the methodology's potential to be used in the fetal environment [114, 242, 243]. It is important to note that the current acquisition time of ~40 minutes presents an obvious challenge to translating the work presented in Chapters 3 and 4 to humans; however, the protocol can be altered by reducing the acquisition time, incorporating free-breathing approaches, or compensating for both maternal and fetal motion to make the protocol feasible for human imaging. Hence, translation of this technique to clinical studies is possible and may enable us to learn more about changes in fetal myelination and potentially lead to improvements in the treatment of IUGR pregnancies.

5.3.3   Improve Identification for IUGR

The markers used for IUGR identification in Chapter 4 are all dependent on the size of the fetus. Although these markers are clinically used for IUGR identification, the markers alone or combined are not always perfect in identifying growth-restricted fetuses [64, 67-70]. For the majority, IUGR manifests in fetuses being SGA, placing them in the 10th percentile for weight; however, some fetuses are genetically programmed to be small, causing them to be SGA but not growth-restricted. On the other hand, some fetuses are above the 10th percentile for weight but are not growing to their genetic potential, making them growth-restricted despite their size. Although the volume ratios involving the brain are better identifiers for IUGR than body volume alone due to brain sparing, they are not perfect identifiers for IUGR.

One of the benefits of using MWF as an IUGR marker is that it is a functional marker. Since myelin content is independent of size, it should be reduced in IUGR fetuses compared to GA-matched non-IUGR fetuses, regardless of whether the fetal weight falls below the 10th percentile. As the use of MRI, in conjunction with ultrasound, to assess fetal development is increasing in frequency, the use of fetal myelin content along with the established size and other functional markers, such as PI of the MCA, can improve

the identification of IUGR [302]. The established size markers for IUGR are easily accessible and work well; however, we can use functional markers like MWF to complement the size markers to better identify true IUGR fetuses.

References

1.   Sethi, S., et al., *Quantification of 1.5 T T1 and T2* Relaxation Times of Fetal Tissues in Uncomplicated Pregnancies.* J. Magn. Reson. Imaging, 2021. **54**(1): p. 113-121.

2.   Sethi, S., et al., *Feasibility of MRI Quantification of Myelin Water Fraction in the Fetal Guinea Pig Brain.* J. Magn. Reson. Imaging, 2022.

3.   Moore, K., T. Persaud, and M. Torchia, *The Developing Human: Clinically Oriented Embryology.* 10th ed. 2016, Philadelphia, Pennsylvania: Elsevier.

4.   Mayer, C. and K. Joseph, *Fetal growth: a review of terms, concepts and issues relevant to obstetrics.* Ultrasound Obstet. Gynecol., 2013. **41**(2): p. 136-145.

5.   Harding, R. and A. Bocking, *Fetal growth and development.* 2001, Cambridge, England: Cambridge University Press.

6.   Buckingham, M., S. Meilhac, and S. Zaffran, *Building the mammalian heart from two sources of myocardial cells.* Nat Rev Genet, 2005. **6**(11): p. 826-835.

7.   Jakovcevski, I. and N. Zecevic, *Sequence of oligodendrocyte development in the human fetal telencephalon.* Glia, 2005. **49**(4): p. 480-491.

8.   Mikkola, H.K. and S.H. Orkin, *The journey of developing hematopoietic stem cells.* Development, 2006. **133**(19): p. 3733-3744.

9.   Wynn R, B.R., Monagle P., *Normal Hematopoiesis and the Physiology of Blood.* Pediatric Hematology: A Practical Guide. 2017, Cambridge, England: Cambridge University Press.

10.   Obregon, M.J., et al., *Ontogenesis of thyroid function and interactions with maternal function.* Endocr Dev, 2007. **10**: p. 86-98.

11.   Nakagawa, M. and K.D. Setchell, *Bile acid metabolism in early life: studies of amniotic fluid.* J Lipid Res, 1990. **31**(6): p. 1089-1098.

12.   Colombo, C., et al., *Correlation between fetal and maternal serum bile acid concentrations.* Pediatr. Res., 1985. **19**(2): p. 227-231.

13.   Fowden, A.L. and D.J. Hill, *Intra-uterine programming of the endocrine pancreas.* Br. Med. Bull., 2001. **60**(1): p. 123-142.

14.   Ezuruike, U., et al., *Quantification of Fetal Renal Function Using Fetal Urine Production Rate and Its Reflection on the Amniotic and Fetal Creatinine Levels During Pregnancy.* Front Pediatr, 2022. **10**: p. 841495.

15. O'Rahilly, R., *The timing and sequence of events in the development of the human reproductive system during the embryonic period proper.* Anat Embryol (Berl), 1983. **166**(2): p. 247-261.

16. Poissonnet, C.M., A.R. Burdi, and S.M. Garn, *The chronology of adipose tissue appearance and distribution in the human fetus.* Early Hum Dev, 1984. **10**(1-2): p. 1-11.

17. Poulos, S.P., D.B. Hausman, and G.J. Hausman, *The development and endocrine functions of adipose tissue.* Mol Cell Endocrinol, 2010. **323**(1): p. 20-34.

18. Ghaben, A.L. and P.E. Scherer, *Adipogenesis and metabolic health.* Nat Rev Mol Cell Biol, 2019. **20**(4): p. 242-258.

19. Desoye, G. and E. Herrera, *Adipose tissue development and lipid metabolism in the human fetus: The 2020 perspective focusing on maternal diabetes and obesity.* Prog Lipid Res, 2021. **81**: p. 101082.

20. Schittny, J.C., *Development of the lung.* Cell Tissue Res, 2017. **367**(3): p. 427-444.

21. Rehman, S. and D. Bacha. *Embryology, Pulmonary*. [Internet] 2022 August 8, 2022 [cited 2022 November 18]; Available from: https://www.ncbi.nlm.nih.gov/books/NBK544372/.

22. Pujol, R. and M. Lavigne-Rebillard, *Development of neurosensory structures in the human cochlea.* Acta Otolaryngol, 1992. **112**(2): p. 259-264.

23. Graven, S.N. and J.V. Browne, *Auditory Development in the Fetus and Infant.* Newborn and Infant Nursing Reviews, 2008. **8**(4): p. 187-193.

24. Hall, J.W., 3rd, *Development of the ear and hearing.* J Perinatol, 2000. **20**(8 Pt 2): p. S12-20.

25. Tanaka, S., T. Mito, and S. Takashima, *Progress of myelination in the human fetal spinal nerve roots, spinal cord and brainstem with myelin basic protein immunohistochemistry.* Early Hum Dev, 1995. **41**(1): p. 49-59.

26. Hijazi, A., *Effects of Prenatal Exposure to Bisphenol A on Fetal Lung Development*. 2016, University of Western Ontario: London, ON, Canada.

27. C.H, R., *The Liver: Morphology, Biochemistry, Physiology*. 1963, New York, NY, USA: Academic Press.

28. Breborowicz, G.H., *Limits of fetal viability and its enhancement.* Early Pregnancy (Cherry Hill), 2001. **5**(1): p. 49-50.

29.   Toi, A., W.S. Lister, and K.W. Fong, *How early are fetal cerebral sulci visible at prenatal ultrasound and what is the normal pattern of early fetal sulcal development?* Ultrasound Obstet Gynecol, 2004. **24**(7): p. 706-715.

30.   W, B., *Uber die Anlage und Entwicklung des Fettgewebes beim Menschen.* Z Morphol. Anthropol., 1911. **45**: p. 305-342.

31.   Kramer, M.S., et al., *A new and improved population-based Canadian reference for birth weight for gestational age.* Pediatrics, 2001. **108**(2): p. E35.

32.   H.I., K., *Development of liver and biliary duct (in Japanese) Shusanki Igaku.* Vol. 13. 1983.

33.   Spong, C.Y., *Defining "term" pregnancy: Recommendations from the defining "term" pregnancy workgroup.* JAMA, 2013. **309**(23): p. 2445-2446.

34.   Jamshed, S., et al., *Frequency of Normal Birth Length and Its Determinants: A Cross-Sectional Study in Newborns.* Cureus, 2020. **12**(9): p. e10556.

35.   Herrera, E. and H. Ortega-Senovilla, *Implications of Lipids in Neonatal Body Weight and Fat Mass in Gestational Diabetic Mothers and Non-Diabetic Controls.* Curr Diab Rep, 2018. **18**(2): p. 7.

36.   Enzi, G., et al., *Intrauterine growth and adipose tissue development.* Am J Clin Nutr, 1981. **34**(9): p. 1785-1790.

37.   Dunlop, M. and J.M. Court, *Lipogenesis in developing human adipose tissue.* Early Hum Dev, 1978. **2**(2): p. 123-130.

38.   Burton, G.J. and A.L. Fowden, *The placenta: a multifaceted, transient organ.* Philos Trans R Soc Lond B Biol Sci, 2015. **370**(1663): p. 20140066.

39.   Moser, G., et al., *Maternal Platelets—Friend or Foe of the Human Placenta?* Int J Mol Sci, 2019. **20**(22): p. 5639.

40.   Jauniaux, E., A. Bhide, and G.J. Burton, *The placenta*, in *Oxford Textbook of Obstetrics and Gynaecology*, S. Arulkumaran, et al., Editors. 2020, Oxford University Press.

41.   Spiliopoulos, M., et al., *Characterizing placental stiffness using ultrasound shear-wave elastography in healthy and preeclamptic pregnancies.* Arch Gynecol Obstet, 2020. **302**(5): p. 1103-1112.

42.   Stenhouse, C., et al., *Insights into the Regulation of Implantation and Placentation in Humans, Rodents, Sheep, and Pigs.* Adv Exp Med Biol, 2022. **1354**: p. 25-48.

43.   Wang, Y. and S. Zhao, *Chapter 2, Placental Blood Circulation*, in *Vascular Biology of the Placenta*. 2010, Morgan & Claypool Life Sciences: San Rafael, California.

44.   Enders, A.C., *A comparative study of the fine structure of the trophoblast in several hemochorial placentas.* Am J Anat, 1965. **116**(1): p. 29-67.

45.   Cunningham, F., et al., *Chapter 3. Implantation, embryogenesis, and placental development*, in *Williams Obstetrics*. 2005, McGraw-Hill: New York. p. 39-90.

46.   Wang, Y. and S. Zhao, *Chapter 3, Structure of the Placenta*, in *Vascular Biology of the Placenta*. 2010, Morgan & Claypool Life Sciences: San Rafael, California.

47.   Gowland, P.A., et al., *In vivo perfusion measurements in the human placenta using echo planar imaging at 0.5 T.* Magn Reson Med, 1998. **40**(3): p. 467-473.

48.   Bowman, C.E., Z. Arany, and M.J. Wolfgang, *Regulation of maternal-fetal metabolic communication.* Cell Mol Life Sci, 2021. **78**(4): p. 1455-1486.

49.   Jones, C.T., *Fetal metabolism and fetal growth.* J Reprod Fertil., 1976. **47**(1): p. 189-201.

50.   Díaz, P., T.L. Powell, and T. Jansson, *The role of placental nutrient sensing in maternal-fetal resource allocation.* Biol Reprod, 2014. **91**(4): p. 82.

51.   Lausman, A. and J. Kingdom, *Intrauterine growth restriction: screening, diagnosis, and management.* J Obstet Gynaecol Can, 2013. **35**(8): p. 741-748.

52.   Macdonald, P.C., et al., *Fetal growth restriction*, in *Williams Obstetrics*, F.G. Cunningham, Editor. 1997, Appleton & Lange: Stamford, Connecticut. p. 839-854.

53.   Tesfa, D., et al., *Intrauterine growth restriction and its associated factors in South Gondar zone hospitals, Northwest Ethiopia, 2019.* Arch Public Health, 2020. **78**: p. 89.

54.   Bjarnegård, N., et al., *Cardiovascular function in adulthood following intrauterine growth restriction with abnormal fetal blood flow.* Ultrasound Obstet Gynecol, 2013. **41**(2): p. 177-184.

55.   Longo, S., et al., *Short-term and long-term sequelae in intrauterine growth retardation (IUGR).* J Matern Fetal Neonatal Med, 2013. **26**(3): p. 222-225.

56.   Daskalakis, G.J., et al., *The EBCOG Postgraduate Textbook of Obstetrics & Gynaecology: Obstetrics & Maternal-Fetal Medicine* 2021, Cambridge University Press: Cambridge, England. p. 158-166.

57.   Riyami, N.A., et al., *Utility of head/abdomen circumference ratio in the evaluation of severe early-onset intrauterine growth restriction.* J Obstet Gynaecol Can, 2011. **33**(7): p. 715-719.

58.   Halliday, H.L., *Neonatal management and long-term sequelae.* Best Pract Res Clin Obstet Gynaecol, 2009. **23**(6): p. 871-880.

59.   Campbell, S. and A. Thoms, *Ultrasound measurement of the fetal head to abdomen circumference ratio in the assessment of growth retardation.* Br J Obstet Gynaecol, 1977. **84**(3): p. 165-174.

60.   Jones, C.T. and J.T. Parer, *The effect of alterations in placental blood flow on the growth of and nutrient supply to the fetal guinea-pig.* J Physiol, 1983. **343**: p. 525-537.

61.   Pollack, R.N. and M.Y. Divon, *Intrauterine growth retardation: definition, classification, and etiology.* Clin Obstet Gynecol, 1992. **35**(1): p. 99-107.

62.   Villar, J., et al., *The differential neonatal morbidity of the intrauterine growth retardation syndrome.* Am J Obstet Gynecol, 1990. **163**(1 Pt 1): p. 151-157.

63.   Pallotto, E.K. and H.W. Kilbride, *Perinatal outcome and later implications of intrauterine growth restriction.* Clin Obstet Gynecol, 2006. **49**(2): p. 257-269.

64.   Mitchell, M.L., *Fetal brain to liver weight ratio as a measure of intrauterine growth retardation: analysis of 182 stillborn autopsies.* Mod Pathol, 2001. **14**(1): p. 14-19.

65.   Boito, S., et al., *Fetal brain/liver volume ratio and umbilical volume flow parameters relative to normal and abnormal human development.* Ultrasound Obstet Gynecol, 2003. **21**(3): p. 256-261.

66.   Li, K., et al., *Measurement of the Brain Volume/Liver Volume Ratio by Three-Dimensional MRI in Appropriate-for-Gestational Age Fetuses and Those With Fetal Growth Restriction.* J Magn Reson Imaging, 2021. **54**(6): p. 1796-1801.

67.   Salavati, N., et al., *Birth weight to placenta weight ratio and its relationship to ultrasonic measurements, maternal and neonatal morbidity: A prospective cohort study of nulliparous women.* Placenta, 2018. **63**: p. 45-52.

68.   Harel, S., et al., *The cephalization index: a screening device for brain maturity and vulnerability in normal and intrauterine growth retarded newborns.* Brain Dev, 1985. **7**(6): p. 580-584.

69.   Sharma, D., S. Shastri, and P. Sharma, *Intrauterine Growth Restriction: Antenatal and Postnatal Aspects.* Clin Med Insights Pediatr, 2016. **10**: p. 67-83.

70.   Wigglesworth, J., *Perinatal Pathology*, in *Perinatal Pathology*. 1996. p. 399.

71. Malik, R. and A. Saxena, *Role of Colour Doppler Indices in the Diagnosis of Intrauterine Growth Retardation in High-Risk Pregnancies.* J Obstet Gynaecol India, 2013. **63**(1): p. 37-44.

72. Lee, S. and S.P. Walker, *The role of ultrasound in the diagnosis and management of the growth restricted fetus.* Australas J Ultrasound Med, 2010. **13**(3): p. 31-36.

73. Alfirevic, Z., T. Stampalija, and T. Dowswell, *Fetal and umbilical Doppler ultrasound in high-risk pregnancies.* Cochrane Database Syst Rev, 2017. **6**(6): p. CD007529.

74. Berghella, V., *Prevention of recurrent fetal growth restriction.* Obstet Gynecol, 2007. **110**(4): p. 904-912.

75. Hernandez-Andrade, E., et al., *Changes in regional fetal cerebral blood flow perfusion in relation to hemodynamic deterioration in severely growth-restricted fetuses.* Ultrasound Obstet Gynecol, 2008. **32**(1): p. 71-76.

76. Fleiss, B., et al., *Knowledge Gaps and Emerging Research Areas in Intrauterine Growth Restriction-Associated Brain Injury.* Front Endocrinol (Lausanne), 2019. **10**: p. 188.

77. Baschat, A.A., et al., *Predictors of neonatal outcome in early-onset placental dysfunction.* Obstet Gynecol, 2007. **109**(2 Pt 1): p. 253-261.

78. Murki, S. and D. Sharma, *Intrauterine growth retardation–a review article.* J Neonatal Biol, 2014. **3**(135).

79. Mandruzzato, G., et al., *Intrauterine restriction (IUGR).* Journal of perinatal medicine, 2008. **36**(4): p. 277-281.

80. Figueras, F., et al., *Customised birthweight standards accurately predict perinatal morbidity.* Arch Dis Child Fetal Neonatal Ed, 2007. **92**(4): p. F277-F280.

81. Vijayaselvi, R. and A.G. Cherian, *Risk assessment of intrauterine growth restriction.* Current Medical Issues, 2017. **15**(4): p. 262-266.

82. Sharma, D., et al., *Intrauterine growth restriction – part 1.* J Matern Fetal Neonatal Med, 2016. **29**(24): p. 3977-3987.

83. Gaccioli, F. and S. Lager, *Placental Nutrient Transport and Intrauterine Growth Restriction.* Front Physiol, 2016. **7**: p. 40.

84. Gardosi, J. and A. Francis, *A customized standard to assess fetal growth in a US population.* Am J Obstet Gynecol, 2009. **201**(1): p. 25.e1-25.e7.

85. Ghidini, A., *Idiopathic fetal growth restriction: a pathophysiologic approach.* Obstet Gynecol Surv, 1996. **51**(6): p. 376-382.

86. Chaddha, V., et al., *Developmental biology of the placenta and the origins of placental insufficiency.* Semin Fetal Neonatal Med, 2004. **9**(5): p. 357-369.

87. Jackson, M.R., et al., *Reduced placental villous tree elaboration in small-for-gestational-age pregnancies: relationship with umbilical artery Doppler waveforms.* Am J Obstet Gynecol, 1995. **172**(2 Pt 1): p. 518-525.

88. Trudinger, B.J., et al., *Fetal umbilical artery flow velocity waveforms and placental resistance: clinical significance.* Br J Obstet Gynaecol, 1985. **92**(1): p. 23-30.

89. Hemberger, M., et al., *Differential expression of angiogenic and vasodilatory factors by invasive trophoblast giant cells depending on depth of invasion.* Dev Dyn, 2003. **227**(2): p. 185-191.

90. Kingdom, J., et al., *Development of the placental villous tree and its consequences for fetal growth.* Eur J Obstet Gynecol Reprod Biol, 2000. **92**(1): p. 35-43.

91. Jansson, T. and E. Persson, *Placental transfer of glucose and amino acids in intrauterine growth retardation: studies with substrate analogs in the awake guinea pig.* Pediatr Res, 1990. **28**(3): p. 203-208.

92. Sparks, J.W., et al., *Growth of fetal guinea pig: physical and chemical characteristics.* Am J Physiol, 1985. **248**(1 Pt 1): p. E132-E139.

93. Myatt, L., *Placental adaptive responses and fetal programming.* J Physiol, 2006. **572**(Pt 1): p. 25-30.

94. Mahendran, D., et al., *Amino acid (system A) transporter activity in microvillous membrane vesicles from the placentas of appropriate and small for gestational age babies.* Pediatr Res, 1993. **34**(5): p. 661-665.

95. Tolsa, C.B., et al., *Early alteration of structural and functional brain development in premature infants born with intrauterine growth restriction.* Pediatr Res, 2004. **56**(1): p. 132-138.

96. Padilla, N., et al., *Twelve-month neurodevelopmental outcome in preterm infants with and without intrauterine growth restriction.* Acta Paediatr, 2010. **99**(10): p. 1498-1503.

97. Businelli, C., et al., *Ultrasound evaluation of cortical brain development in fetuses with intrauterine growth restriction.* J Matern Fetal Neonatal Med, 2015. **28**(11): p. 1302-1307.

98. Samuelsen, G.B., et al., *Severe cell reduction in the future brain cortex in human growth-restricted fetuses and infants.* Am J Obstet Gynecol, 2007. **197**(1): p. 56.e1-56.e7.

99.   Miller, S.L., P.S. Huppi, and C. Mallard, *The consequences of fetal growth restriction on brain structure and neurodevelopmental outcome.* J Physiol, 2016. **594**(4): p. 807-823.

100.   Indredavik, M.S., et al., *Perinatal risk and psychiatric outcome in adolescents born preterm with very low birth weight or term small for gestational age.* J Dev Behav Pediatr, 2010. **31**(4): p. 286-294.

101.   Walker, D.M. and N. Marlow, *Neurocognitive outcome following fetal growth restriction.* Arch Dis Child Fetal Neonatal Ed, 2008. **93**(4): p. F322-F325.

102.   Synnes, A.R., et al., *School entry age outcomes for infants with birth weight ≤ 800 grams.* J. Pediatr., 2010. **157**(6): p. 989-994.e1.

103.   Geva, R., et al., *Verbal short-term memory span in children: long-term modality dependent effects of intrauterine growth restriction.* J Child Psychol Psychiatry, 2008. **49**(12): p. 1321-1330.

104.   Leitner, Y., et al., *Six-year follow-up of children with intrauterine growth retardation: long-term, prospective study.* J Child Neurol, 2000. **15**(12): p. 781-786.

105.   Eixarch, E., et al., *Neurodevelopmental outcome in 2-year-old infants who were small-for-gestational age term fetuses with cerebral blood flow redistribution.* Ultrasound Obstet Gynecol, 2008. **32**(7): p. 894-899.

106.   Murray, E., et al., *Differential effect of intrauterine growth restriction on childhood neurodevelopment: a systematic review.* BLOG, 2015. **122**(8): p. 1062-1072.

107.   Hollo, O., et al., *Academic Achievement of Small-for-Gestational-Age Children at Age 10 Years.* Arch Pediatr Adolesc Med, 2002. **156**(2): p. 179-187.

108.   Burger, R.J., et al., *Birth-weight centile at term and school performance at 12 years of age: linked cohort study.* Ultrasound Obstet Gynecol, 2023. **61**(4): p. 458-465.

109.   Isaacs, E.B., et al., *Hippocampal volume and everyday memory in children of very low birth weight.* Pediatr Res, 2000. **47**(6): p. 713-720.

110.   Løhaugen, G.C., et al., *Small for gestational age and intrauterine growth restriction decreases cognitive function in young adults.* J Pediatr, 2013. **163**(2): p. 447-453.

111.   Østgård, H.F., et al., *Neuropsychological deficits in young adults born small-for-gestational age (SGA) at term.* J Int Neuropsychol Soc, 2014. **20**(3): p. 313-323.

112.   Cannon, T.D., et al., *Early and late neurodevelopmental influences in the prodrome to schizophrenia: contributions of genes, environment, and their interactions.* Schizophr Bull, 2003. **29**(4): p. 653-669.

113.   Gilles, F.H., *The developing human brain: what the emerging pediatric neurologist needs to know.* Semin Pediatr Neurol, 2011. **18**(2): p. 124-127.

114.   MacKay, A., et al., *In vivo visualization of myelin water in brain by magnetic resonance.* Magn Reson Med, 1994. **31**(6): p. 673-677.

115.   Min, Y., et al., *Interaction forces and adhesion of supported myelin lipid bilayers modulated by myelin basic protein.* Proc Natl Acad Sci U S A, 2009. **106**(9): p. 3154-9.

116.   Umemori, H., et al., *Initial events of myelination involve Fyn tyrosine kinase signalling.* Nature, 1994. **367**(6463): p. 572-576.

117.   Simons, M. and K.A. Nave, *Oligodendrocytes: Myelination and Axonal Support.* Cold Spring Harb Perspect Biol, 2015. **8**(1): p. a020479.

118.   Akaishi, T., *Nerve conduction models in myelinated and unmyelinated nerves based on three-dimensional electrostatic interaction.* Neural Regen Res, 2018. **13**(5): p. 779-785.

119.   Brady, S., *Basic Neurochemistry: Molecular, Cellular and Medical Aspects.* 2005, Amsterdam, Netherlands: Elsevier.

120.   O'Brien, J.S., *Stability of the Myelin Membrane.* Science, 1965. **147**(3662): p. 1099-1107.

121.   Hemmings, H.C. and T.D. Egan, *Pharmacology and Physiology for Anesthesia: Foundations and Clinical Application.* 2013, Elsevier: Philadelphia, Pennsylvania. p. 102-122.

122.   Weimbs, T. and W. Stoffel, *Proteolipid protein (PLP) of CNS myelin: positions of free, disulfide-bonded, and fatty acid thioester-linked cysteine residues and implications for the membrane topology of PLP.* Biochemistry, 1992. **31**(49): p. 12289-12296.

123.   Werner, H.B., et al., *A critical role for the cholesterol-associated proteolipids PLP and M6B in myelination of the central nervous system.* Glia, 2013. **61**(4): p. 567-586.

124.   Aggarwal, S., et al., *A size barrier limits protein diffusion at the cell surface to generate lipid-rich myelin-membrane sheets.* Dev Cell, 2011. **21**(3): p. 445-456.

125.   Readhead, C. and L. Hood, *The dysmyelinating mouse mutations shiverer (shi) and myelin deficient (shi mld).* Behav Genet, 1990. **20**: p. 213-234.

126. Purves D, A.G., Fitzpatrick D, et al.,, *Increased Conduction Velocity as a Result of Myelination*, in *Neuroscience*. 2001, Sinauer Associates: Sunderland, Massachusetts.

127. Susuki, K., *Myelin: A specialized membrane for cell communication.* Nature Edu, 2010. **3**(9): p. 59.

128. Saab, A.S., I.D. Tzvetanova, and K.A. Nave, *The role of myelin and oligodendrocytes in axonal energy metabolism.* Curr Opin Neurobiol, 2013. **23**(6): p. 1065-1072.

129. Chang, K.J., S.A. Redmond, and J.R. Chan, *Remodeling myelination: implications for mechanisms of neural plasticity.* Nat Neurosci, 2016. **19**(2): p. 190-197.

130. McKenzie, I.A., et al., *Motor skill learning requires active central myelination.* Science, 2014. **346**(6207): p. 318-322.

131. Kinney, H.C., et al., *Myelination in the developing human brain: biochemical correlates.* Neurochem Res, 1994. **19**(8): p. 983-996.

132. Clasen, R.A., et al., *A chemical basis for the staining of myelin sheaths by luxol dye techniques; further observations.* J Neuropathol Exp Neurol, 1967. **26**(1): p. 153-154.

133. Laule, C., et al., *Myelin water imaging in multiple sclerosis: quantitative correlations with histopathology.* Mult Scler, 2006. **12**(6): p. 747-753.

134. Brody, B.A., et al., *Sequence of central nervous system myelination in human infancy. I. An autopsy study of myelination.* J Neuropathol Exp Neurol, 1987. **46**(3): p. 283-301.

135. Kinney, H.C., et al., *Sequence of central nervous system myelination in human infancy. II. Patterns of myelination in autopsied infants.* J Neuropathol Exp Neurol, 1988. **47**(3): p. 217-234.

136. Wu, C., et al., *A novel PET marker for in vivo quantification of myelination.* Bioorg Med Chem, 2010. **18**(24): p. 8592-8599.

137. van Dijk, M.C., et al., *Fetal and Perinatal Brain Autopsy: Useful Macroscopic Techniques Including Agar In-situ and Pre-Embedding Methods.* Pediatr Dev Pathol, 2021. **24**(4): p. 299-308.

138. Moscarello, M.A., *Cell Biology and Pathology of Myelin: Evolving Biological Concepts and Therapeutic Approaches*. 1997, Springer: New York, New York. p. 13-25.

139. Harauz, G., et al., *Myelin basic protein-diverse conformational states of an intrinsically unstructured protein and its roles in myelin assembly and multiple sclerosis.* Micron, 2004. **35**(7): p. 503-542.

140. Pedraza, L., et al., *The active transport of myelin basic protein into the nucleus suggests a regulatory role in myelination.* Neuron, 1997. **18**(4): p. 579-589.

141. Weidenheim, K.M., et al., *Neuroanatomical localization of myelin basic protein in the late first and early second trimester human foetal spinal cord and brainstem.* J Neurocytol, 1993. **22**(7): p. 507-516.

142. Back, S.A., et al., *Late oligodendrocyte progenitors coincide with the developmental window of vulnerability for human perinatal white matter injury.* J Neurosci, 2001. **21**(4): p. 1302-1312.

143. Chase, H.P., et al., *Alterations in human brain biochemistry following intrauterine growth retardation.* Pediatrics, 1972. **50**(3): p. 403-411.

144. Folkerth, R.D., et al., *Developmental lag in superoxide dismutases relative to other antioxidant enzymes in premyelinated human telencephalic white matter.* J Neuropathol Exp Neurol, 2004. **63**(9): p. 990-999.

145. Grinspan, J.B., et al., *Stage-specific effects of bone morphogenetic proteins on the oligodendrocyte lineage.* J Neurobiol, 2000. **43**(1): p. 1-17.

146. See, J., et al., *Oligodendrocyte maturation is inhibited by bone morphogenetic protein.* Mol Cell Neurosci, 2004. **26**(4): p. 481-492.

147. Gomes, W.A., M.F. Mehler, and J.A. Kessler, *Transgenic overexpression of BMP4 increases astroglial and decreases oligodendroglial lineage commitment.* Dev Biol, 2003. **255**(1): p. 164-177.

148. Grinspan, J.B., *Bone morphogenetic proteins: inhibitors of myelination in development and disease.* Vitam Horm, 2015. **99**: p. 195-222.

149. Reid, M.V., et al., *Delayed myelination in an intrauterine growth retardation model is mediated by oxidative stress upregulating bone morphogenetic protein 4.* J Neuropathol Exp Neurol, 2012. **71**(7): p. 640-653.

150. Han, V.K., *Pathophysiology, cellular and molecular mechanisms of foetal growth retardation.* Equine Vet J Suppl, 1993(14): p. 12-6.

151. Lafeber, H.N., T.P. Rolph, and C.T. Jones, *Studies on the growth of the fetal guinea pig. The effects of ligation of the uterine artery on organ growth and development.* J Dev Physiol, 1984. **6**(6): p. 441-459.

152. Hayashi, T.T. and M.E. Dorko, *A rat model for the study of intrauterine growth retardation.* Am J Obstet Gynecol, 1988. **158**(5): p. 1203-1207.

153. Huizinga, C.T., et al., *Effects of intrauterine and early postnatal growth restriction on hypothalamic somatostatin gene expression in the rat.* Pediatr Res, 2000. **48**(6): p. 815-820.

154. Schreuder, M.F., J.A. van Wijk, and H.A. Delemarre-van de Waal, *Intrauterine growth restriction increases blood pressure and central pulse pressure measured with telemetry in aging rats.* J Hypertens, 2006. **24**(7): p. 1337-1343.

155. Mattern, J., et al., *Oral pyrroloquinoline quinone (PQQ) during pregnancy increases cardiomyocyte endowment in spontaneous IUGR guinea pigs.* J Dev Orig Health Dis, 2023: p. 1-4.

156. Horton, D.M., et al., *Sex-specific programming of adult insulin resistance in guinea pigs by variable perinatal growth induced by spontaneous variation in litter size.* Am J Physiol Regul Integr Comp Physiol, 2019. **316**(4): p. R352-R361.

157. Horton, D.M., et al., *Spontaneous intrauterine growth restriction due to increased litter size in the guinea pig programmes postnatal growth, appetite and adult body composition.* J Dev Orig Health Dis, 2016. **7**(5): p. 548-562.

158. Rocha, E., et al., *Structural proteins during brain development in the preterm and near-term ovine fetus and the effect of intermittent umbilical cord occlusion.* Am J Obstet Gynecol, 2004. **191**(2): p. 497-506.

159. Mallard, E.C., et al., *Effects of chronic placental insufficiency on brain development in fetal sheep.* Pediatr Res, 1998. **43**(2): p. 262-270.

160. Olivier, P., et al., *Moderate growth restriction: deleterious and protective effects on white matter damage.* Neurobiol Dis, 2007. **26**(1): p. 253-263.

161. Nitsos, I. and S. Rees, *The effects of intrauterine growth retardation on the development of neuroglia in fetal guinea pigs. An immunohistochemical and an ultrastructural study.* Int J Dev Neurosci, 1990. **8**(3): p. 233-244.

162. Piorkowska, K., et al., *Synaptic development and neuronal myelination are altered with growth restriction in fetal guinea pigs.* Dev Neurosci, 2014. **36**(6): p. 465-476.

163. Dobbing, J. and J. Sands, *Growth and development of the brain and spinal cord of the guinea pig.* Brain Res, 1970. **17**(1): p. 115-123.

164. Morrison, J.L., et al., *Guinea pig models for translation of the developmental origins of health and disease hypothesis into the clinic.* J Physiol, 2018. **596**(23): p. 5535-5569.

165. Lennon, A.M., et al., *Rat, mouse, and guinea pig brain development and microtubule assembly.* J Neurochem, 1980. **35**(4): p. 804-813.

166. Clancy, B., et al., *Web-based method for translating neurodevelopment from laboratory species to humans.* Neuroinformatics, 2007. **5**(1): p. 79-94.

167. Carter, A.M., *Animal models of human placentation--a review.* Placenta, 2007. **28 Suppl A**: p. S41-S47.

168. Kaufmann, P., *Guinea Pig (Cavia porcellus)*, in *Comparative Placentation*. 2004, San Diego Zoo Institute for Conservation Research Escondido, CA, USA.

169. Lauterbur, P.C., *Image Formation by Induced Local Interactions: Examples Employing Nuclear Magnetic Resonance.* Nature, 1973. **242**(5394): p. 190–191.

170. Mansfield, P. and A.A. Maudsley, *Medical imaging by NMR.* Br J Radiol, 1977. **50**(591): p. 188-194.

171. Smith, F.W., A.H. Adam, and W.D. Phillips, *NMR imaging in pregnancy.* Lancet, 1983. **1**(8314-5): p. 61-62.

172. Prayer, D. and P.C. Brugger, *Investigation of normal organ development with fetal MRI.* Eur Radiol, 2007. **17**(10): p. 2458-2471.

173. Stecco, A., A. Saponaro, and A. Carriero, *Patient safety issues in magnetic resonance imaging: state of the art.* Radiol Med, 2007. **112**(4): p. 491-508.

174. Frates, M.C., et al., *Fetal anomalies: comparison of MR imaging and US for diagnosis.* Radiology, 2004. **232**(2): p. 398-404.

175. Meyer-Wittkopf, M., et al., *Evaluation of three-dimensional ultrasonography and magnetic resonance imaging in assessment of congenital heart anomalies in fetal cardiac specimens.* Ultrasound Obstet Gynecol, 1996. **8**(5): p. 303-308.

176. Plewes, D.B. and W. Kucharczyk, *Physics of MRI: a primer.* J Magn Reson Imaging, 2012. **35**(5): p. 1038-1054.

177. McRobbie, D.W., et al., *MRI from Picture to Proton*. 2003, Cambridge, England: Cambridge University Press.

178. Constantinides, C., *Magnetic resonance imaging: the basics*. 2016: CRC press.

179. Brown, R.W., et al., *Magnetic Resonance Imaging: Physical Principles and Sequence Design*. 2014: John Wiley & Sons, Inc.

180. Eom, H.J., *Faraday's Law of Induction*, in *Primary Theory of Electromagnetics*. 2013, Springer Dordrecht: New York, New York. p. 95-111.

181. Hahn, E.L., *Spin echoes.* Phys Rev, 1950. **80**(4): p. 580.

182. Zur, Y., M.L. Wood, and L.J. Neuringer, *Spoiling of transverse magnetization in steady-state sequences.* Magn Reson Med, 1991. **21**(2): p. 251-263.

183. Epstein, F.H., J.P. Mugler, 3rd, and J.R. Brookeman, *Spoiling of transverse magnetization in gradient-echo (GRE) imaging during the approach to steady state.* Magn Reson Med, 1996. **35**(2): p. 237-245.

184. James, J.F., *A Student's Guide to Fourier Transforms With Applications in Physics and Engineering*. 2nd ed. 2002, Cambridge, England: Cambridge University Press.

185. Mezrich, R., *A perspective on K-space.* Radiology, 1995. **195**(2): p. 297-315.

186. Twieg, D.B., *The k-trajectory formulation of the NMR imaging process with applications in analysis and synthesis of imaging methods.* Med Phys, 1983. **10**(5): p. 610-621.

187. Gallagher, T.A., A.J. Nemeth, and L. Hacein-Bey, *An introduction to the Fourier transform: relationship to MRI.* AJR Am J Roentgenol, 2008. **190**(5): p. 1396-1405.

188. Bloch, F., *Nuclear Induction.* Phys. Rev., 1946. **70**: p. 460-474.

189. de Bazelaire, C.M., et al., *MR imaging relaxation times of abdominal and pelvic tissues measured in vivo at 3.0 T: preliminary results.* Radiology, 2004. **230**(3): p. 652-659.

190. Chavhan, G.B., et al., *Principles, techniques, and applications of T2*-based MR imaging and its special applications.* Radiographics, 2009. **29**(5): p. 1433-1449.

191. Paus, T., et al., *Maturation of white matter in the human brain: a review of magnetic resonance studies.* Brain Res Bull, 2001. **54**(3): p. 255-266.

192. Deoni, S.C., *Quantitative relaxometry of the brain.* Top Magn Reson Imaging, 2010. **21**(2): p. 101-113.

193. Gelman, N., et al., *Interregional variation of longitudinal relaxation rates in human brain at 3.0 T: relation to estimated iron and water contents.* Magn Reson Med, 2001. **45**(1): p. 71-79.

194. Gelman, N., et al., *MR imaging of human brain at 3.0 T: preliminary report on transverse relaxation rates and relation to estimated iron content.* Radiology, 1999. **210**(3): p. 759-767.

195. Li, Y., et al., *Comparison of T(1) and T(2) metabolite relaxation times in glioma and normal brain at 3T.* J Magn Reson Imaging, 2008. **28**(2): p. 342-350.

196. Cheng, H.L., et al., *Practical medical applications of quantitative MR relaxometry.* J Magn Reson Imaging, 2012. **36**(4): p. 805-824.

197. Bydder, G.M. and I.R. Young, *MR imaging: clinical use of the inversion recovery sequence.* J Comput Assist Tomogr, 1985. **9**(4): p. 659-675.

198. Manfredonia, F., et al., *Normal-appearing brain t1 relaxation time predicts disability in early primary progressive multiple sclerosis.* Arch. Neurol., 2007. **64**(3): p. 411-415.

199. Jack Jr., C.R., et al., *In vivo magnetic resonance microimaging of individual amyloid plaques in Alzheimer's transgenic mice.* J. Neurosci., 2005. **25**(43): p. 10041-10048.

200. Mezer, A., et al., *Evaluating quantitative proton-density-mapping methods.* Hum. Brain Mapp., 2016. **37**(10): p. 3623-3635.

201. Liney, G.P., et al., *Comparison of conventional single echo and multi-echo sequences with a fast spin-echo sequence for quantitative T2 mapping: application to the prostate.* J. Magn. Reson. Imaging, 1996. **6**(4): p. 603-607.

202. Look, D.C. and L. D.R., *Time Saving in Measurement of NMR and EPR Relaxation Times.* Rev. Sci. Instrum., 1970. **41**(2): p. 250-251.

203. Christensen, K.A., et al., *Optimal Determination of Relaxation Times of Fourier Transform Nuclear Magnetic Resonance. Determination of Spin-Lattive Relaxation Times in Chemically Polarized Species.* J. Phys. Chem, 1974. **78**(19): p. 1971-1977.

204. Homer, J. and M.S. Beevers, *Driven-equilibrium single-pulse observation of T1 relaxation. A reevaluation of a rapid "new" method for determining NMR spin-lattice relaxation times.* J. Magn. Reson., 1985. **63**(2): p. 287-297.

205. Homer, J. and J.K. Roberts, *Routine evaluation of M0 ratios and T1 values from driven-equilibrium NMR spectra.* J. Magn. Reson., 1990. **87**(2): p. 265-272.

206. Wang, H.Z., S.J. Riederer, and J.N. Lee, *Optimizing the Precision in T1 Relaxation Estimation using Limited Flip Angles.* Magn. Reson. Med., 1987. **5**(5): p. 399-416.

207. Chang, L.C., et al., *Linear least-squares method for unbiased estimation of T1 from SPGR signals.* Magn. Reson. Med., 2008. **60**(2): p. 496-501.

208. Deoni, S.C., T.M. Peters, and B.K. Rutt, *Determination of optimal angles for variable nutation proton magnetic spin-lattice, T1, and spin-spin, T2, relaxation times measurement.* Magn. Reson. Med., 2004. **51**(1): p. 194-199.

209. Deoni, S.C., B.K. Rutt, and T.M. Peters, *Rapid combined T1 and T2 mapping using gradient recalled acquisition in the steady state.* Magn. Reson. Med., 2003. **49**(3): p. 515-526.

210. Carr, H.Y., *Steady-State Free Precession in Nuclear Magnetic Resonance.* Phys. Rev., 1958. **112**: p. 1693-1701.

211. Schmitt, P., et al., *Inversion recovery TrueFISP: quantification of T(1), T(2), and spin density.* Magn. Reson. Med., 2004. **51**(4): p. 661-667.

212. Scheffler, K. and J. Hennig, *T(1) quantification with inversion recovery TrueFISP.* Magn. Reson. Med., 2001. **45**(4): p. 720-723.

213. Elster, A.D., *Gradient-echo MR imaging: techniques and acronyms.* Radiology, 1993. **186**(1): p. 1-8.

214. Scheffler, K. and S. Lehnhardt, *Principles and applications of balanced SSFP techniques.* Eur. Radiol., 2003. **13**(11): p. 2409-2418.

215. Miller, K.L., *FMRI using balanced steady-state free precession (SSFP).* Neuroimage, 2012. **62**(2): p. 713-719.

216. Zur, Y., S. Stokar, and P. Bendel, *An analysis of fast imaging sequences with steady-state transverse magnetization refocusing.* Magn. Reson. Med., 1988. **6**(2): p. 175-193.

217. Du, J., et al., *Ultrashort echo time (UTE) magnetic resonance imaging of the short T2 components in white matter of the brain using a clinical 3T scanner.* Neuroimage, 2014. **87**: p. 32-41.

218. Sheth, V., et al., *Magnetic resonance imaging of myelin using ultrashort Echo time (UTE) pulse sequences: Phantom, specimen, volunteer and multiple sclerosis patient studies.* Neuroimage, 2016. **136**: p. 37-44.

219. Bernstein, M.A., K.F. King, and X.J. Zhou, *Handbook of MRI pulse sequences*. 2004, Cambridge, Massachusetts: Academic Press.

220. Vavasour, I.M., et al., *Different magnetization transfer effects exhibited by the short and long T(2) components in human brain.* Magn. Reson. Med., 2000. **44**(6): p. 860-866.

221. Vavasour, I.M., et al., *Is the magnetization transfer ratio a marker for myelin in multiple sclerosis?* J. Magn. Reson. Imaging, 2011. **33**(3): p. 713-718.

222. Ulmer, J.L., et al., *Magnetization transfer or spin-lock? An investigation of off-resonance saturation pulse imaging with varying frequency offsets.* AJNR Am. J. Neuroradiol., 1996. **17**(5): p. 805-819.

223. Prevost, V., et al., *Optimization of inhomogeneous magnetization transfer (ihMT) MRI contrast for preclinical studies using dipolar relaxation time (T1D) filtering.* NMR Biomed., 2017. **30**(6): p. e3706.

224. Hertanu, A., et al., *T1D -weighted ihMT imaging - Part II. Investigating the long- and short-T1D components correlation with myelin content. Comparison with R1 and the macromolecular proton fraction.* Mag. Reson. Med., 2022. **87**(5): p. 2329-2346.

225. Song, S.K., et al., *Dysmyelination revealed through MRI as increased radial (but unchanged axial) diffusion of water.* Neuroimage, 2002. **17**(3): p. 1429-36.

226. Wang, X., et al., *Diffusion basis spectrum imaging detects and distinguishes coexisting subclinical inflammation, demyelination and axonal injury in experimental autoimmune encephalomyelitis mice.* NMR Biomed, 2014. **27**(7): p. 843-52.

227. Beaulieu, C., *The basis of anisotropic water diffusion in the nervous system - a technical review.* NMR Biomed, 2002. **15**(7-8): p. 435-55.

228. MacKay, A.L. and C. Laule, *Magnetic Resonance of Myelin Water: An in vivo Marker for Myelin.* Brain Plast, 2016. **2**(1): p. 71-91.

229. Prasloski, T., et al., *Rapid whole cerebrum myelin water imaging using a 3D GRASE sequence.* Neuroimage, 2012. **63**(1): p. 533-539.

230. Travis, A.R. and M.D. Does, *Selective excitation of myelin water using inversion-recovery-based preparations.* Magn. Reson. Med., 2005. **54**(3): p. 743-747.

231. Whittall, K.P., et al., *In vivo measurement of T2 distributions and water contents in normal human brain.* Magn. Reson. Med., 1997. **37**(1): p. 34-43.

232. Du, Y.P., et al., *Fast multislice mapping of the myelin water fraction using multicompartment analysis of T2* decay at 3T: a preliminary postmortem study.* Magn. Reson. Med., 2007. **58**(5): p. 865-870.

233. van Gelderen, P., et al., *Nonexponential T_2 decay in white matter.* Magn. Reson. Med., 2012. **67**(1): p. 110-117.

234. Lee, D., et al., *Single-scan z-shim method for reducing susceptibility artifacts in gradient echo myelin water imaging.* Magn. Reson. Med., 2018. **80**(3): p. 1101-1109.

235. Lee, H., et al., *Improved three-dimensional multi-echo gradient echo based myelin water fraction mapping with phase related artifact correction.* Neuroimage, 2018. **169**: p. 1-10.

236. Alonso-Ortiz, E., et al., *Field inhomogeneity correction for gradient echo myelin water fraction imaging.* Magn. Reson. Med., 2017. **78**(1): p. 49-57.

237. Labadie, C., et al., *Myelin water mapping by spatially regularized longitudinal relaxographic imaging at high magnetic fields.* Magn. Reson. Med., 2014. **71**(1): p. 375-387.

238. Andrews, T.J., M.T. Osborne, and M.D. Does, *Diffusion of myelin water.* Magn. Reson. Med., 2006. **56**(2): p. 381-385.

239. Oh, S.H., et al., *Direct visualization of short transverse relaxation time component (ViSTa).* Neuroimage, 2013. **83**: p. 485-492.

240. Choi, J.Y., et al., *Evaluation of Normal-Appearing White Matter in Multiple Sclerosis Using Direct Visualization of Short Transverse Relaxation Time Component (ViSTa) Myelin Water Imaging and Gradient Echo and Spin Echo (GRASE) Myelin Water Imaging.* J. Magn. Reson. Imaging, 2019. **49**(4): p. 1091-1098.

241. Deoni, S.C., et al., *Gleaning multicomponent T1 and T2 information from steady-state imaging data.* Magn. Reson. Med., 2008. **60**(6): p. 1372-1387.

242. Deoni, S.C., *Correction of main and transmit magnetic field (B0 and B1) inhomogeneity effects in multicomponent-driven equilibrium single-pulse observation of T1 and T2.* Magn. Reson. Med., 2011. **65**(4): p. 1021-1035.

243. Faizy, T.D., et al., *The Myelin Water Fraction Serves as a Marker for Age-Related Myelin Alterations in the Cerebral White Matter - A Multiparametric MRI Aging Study.* Front Neurosci,, 2020. **14**: p. 136.

244. Harkins, K.D., A.N. Dula, and M.D. Does, *Effect of intercompartmental water exchange on the apparent myelin water fraction in multiexponential T2 measurements of rat spinal cord.* Magn. Reson. Med., 2012. **67**(3): p. 793-800.

245. McCreary, C.R., et al., *Multiexponential T2 and magnetization transfer MRI of demyelination and remyelination in murine spinal cord.* Neuroimage, 2009. **45**(4): p. 1173-1182.

246. Kozlowski, P., et al., *Characterizing white matter damage in rat spinal cord with quantitative MRI and histology.* J Neurotrauma, 2008. **25**(6): p. 653-676.

247. Webb, S., et al., *Is multicomponent T2 a good measure of myelin content in peripheral nerve?* Magn. Reson. Med., 2003. **49**(4): p. 638-645.

248. Laule, C., et al., *Water content and myelin water fraction in multiple sclerosis. A T2 relaxation study.* J. Neurol., 2004. **251**(3): p. 284-293.

249. Harkins, K.D., et al., *In-vivo multi-exponential T2, magnetization transfer and quantitative histology in a rat model of intramyelinic edema.* Neuroimage Clin., 2013. **2**: p. 810-817.

250. McCarthy, S.M., et al., *Obstetrical magnetic resonance imaging: fetal anatomy.* Radiology, 1985. **154**(2): p. 427-432.

251. Ingram, E., et al., *MR Imaging Measurements of Altered Placental Oxygenation in Pregnancies Complicated by Fetal Growth Restriction.* Radiology, 2017. **285**(3): p. 953-960.

252. Giza, S.A., et al., *Measuring fetal adipose tissue using 3D water-fat magnetic resonance imaging: a feasibility study.* J Matern Fetal Neonatal Med, 2020. **33**(5): p. 831-837.

253. Sinding, M., et al., *Placental magnetic resonance imaging T2* measurements in normal pregnancies and in those complicated by fetal growth restriction.* Ultrasound Obstet Gynecol, 2016. **47**(6): p. 748-754.

254. Schwenzer, N.F., et al., *T2* relaxometry in liver, pancreas, and spleen in a healthy cohort of one hundred twenty-nine subjects-correlation with age, gender, and serum ferritin.* Invest Radiol, 2008. **43**(12): p. 854-860.

255. Semple, S.I., et al., *The measurement of fetal liver T(*)(2) in utero before and after maternal oxygen breathing: progress towards a non-invasive measurement of fetal oxygenation and placental function.* Magn Reson Imaging, 2001. **19**(7): p. 921-928.

256. Derwig, I., et al., *Association of placental T2 relaxation times and uterine artery Doppler ultrasound measures of placental blood flow.* Placenta, 2013. **34**(6): p. 474-479.

257. Morris, D.M., et al., *Changes in foetal liver T2* measurements by MRI in response to maternal oxygen breathing: application to diagnosing foetal growth restriction.* Physiol Meas, 2010. **31**(9): p. 1137-1146.

258. Goitein, O., et al., *Fetal liver T2* values: defining a standardized scale.* J Magn Reson Imaging, 2013. **38**(6): p. 1342-1345.

259. Baadsgaard, K.H., *Assessment of T2* MRI in Selected Fetal Organs and the Association with Low Birth Weight*, in *Clinical Medicine Obstetrics and Gynecology*. 2019, Aalborg University: Denmark. p. 18.

260. N, B., P. EM, and P. RV, *Relaxation Effects in Nuclear Magnetic Resonance Absorption.* Physical Review, 1948. **73**: p. 679-715.

261. Butt, K. and K.I. Lim, *Guideline No. 388-Determination of Gestational Age by Ultrasound.* J Obstet Gynaecol Can, 2019. **41**(10): p. 1497-1507.

262. Yu, H., et al., *Multiecho reconstruction for simultaneous water-fat decomposition and T2* estimation.* J Magn Reson Imaging, 2007. **26**(4): p. 1153-1161.

263. Yu, H., et al., *Combination of complex-based and magnitude-based multiecho water-fat separation for accurate quantification of fat-fraction.* Magn Reson Med, 2011. **66**(1): p. 199-206.

264. Yu, H., et al., *Multiecho water-fat separation and simultaneous R2* estimation with multifrequency fat spectrum modeling.* Magn Reson Med, 2008. **60**(5): p. 1122-1134.

265. Fedorov, A., et al., *3D Slicer as an image computing platform for the Quantitative Imaging Network.* Magn Reson Imaging, 2012. **30**(9): p. 1323-1341.

266. Kikinis R., Pieper S.D., and V. K., *3D Slicer: a platform for subject-specific image analysis, visualization, and clinical support., in Intraoperative Imaging Image-Guided Therapy,.* F.A. Jolesz, Editor. Springer: New York, NY., 2014.

267. *3D Slicer. Volume 2016.* 2017.

268. Giza, S.A., et al., *Water-fat magnetic resonance imaging of adipose tissue compartments in the normal third trimester fetus.* Pediatr. Radiol., 2021. **51**(7): p. 1214-1222.

269. Giza, S.A., et al., *Water-Fat MRI of Adipose Tissue Compartments in the Normal, Third Trimester.* Pediatr Radiol, 2020.

270. Beath, S.V., *Hepatic function and physiology in the newborn.* Semin Neonatol, 2003. **8**(5): p. 337-346.

271. Rosenblum, S., A. Pal, and K. Reidy, *Renal development in the fetus and premature infant.* Semin Fetal Neonatal Med, 2017. **22**(2): p. 58-66.

272. Muckenthaler, M.U., et al., *A Red Carpet for Iron Metabolism.* Cell, 2017. **168**(3): p. 344-361.

273. Barzin, M., et al., *Correlation of cardiac MRI T2* with echocardiography in thalassemia major.* Eur Rev Med Pharmacol Sci, 2012. **16**(2): p. 254-260.

274. Du, M., et al., *Fetal programming of skeletal muscle development in ruminant animals.* J Anim Sci, 2010. **88**(13 Suppl): p. E51-60.

275. Du, M., et al., *Maternal obesity, inflammation, and fetal skeletal muscle development.* Biol Reprod, 2010. **82**(1): p. 4-12.

276. Kendrew, J.C., et al., *The species specificity of myoglobin.* Nature, 1954. **174**(4438): p. 946-949.

277. Hu, H.H., et al., *Comparison of brown and white adipose tissues in infants and children with chemical-shift-encoded water-fat MRI.* J Magn Reson Imaging, 2013. **38**(4): p. 885-896.

278. Deoni, S.C., T.M. Peters, and B.K. Rutt, *High-resolution T1 and T2 mapping of the brain in a clinically acceptable time with DESPOT1 and DESPOT2.* Magn Reson Med, 2005. **53**(1): p. 237-241.

279. Hernando, D., et al., *R2* estimation using "in-phase" echoes in the presence of fat: the effects of complex spectrum of fat.* J Magn Reson Imaging, 2013. **37**(3): p. 717-726.

280. Stiles, J. and T.L. Jernigan, *The basics of brain development.* Neuropsychol Rev, 2010. **20**(4): p. 327-348.

281. Bulas, D. and A. Egloff, *Benefits and risks of MRI in pregnancy.* Semin Perinatol, 2013. **37**(5): p. 301-304.

282. Ma, Y.J., et al., *Ultrashort echo time (UTE) magnetic resonance imaging of myelin: technical developments and challenges.* Quant Imaging Med Surg, 2020. **10**(6): p. 1186-1203.

283. Laule, C., et al., *Myelin water imaging of multiple sclerosis at 7 T: correlations with histopathology.* Neuroimage, 2008. **40**(4): p. 1575-1580.

284. Deoni, S.C., et al., *Mapping infant brain myelination with magnetic resonance imaging.* J Neurosci, 2011. **31**(2): p. 784-791.

285. Smith, S.M., et al., *Advances in functional and structural MR image analysis and implementation as FSL.* Neuroimage, 2004. **23 Suppl 1**: p. S208-S219.

286. Wood, T.C., *QUIT: QUantitative Imaging Tools.* The Journal of Open Source Software, 2018. **3**(26): p. 656.

287. Gareau, P.J., et al., *Magnetization transfer and multicomponent T2 relaxation measurements with histopathologic correlation in an experimental model of MS.* J Magn Reson Imaging, 2000. **11**(6): p. 586-595.

288. Sinclair, K.J., et al., *Quantification of fetal organ volume and fat deposition following in utero exposure to maternal Western Diet using MRI.* PLoS One, 2018. **13**(2): p. e0192900.

289. Greulich, S., et al., *Secretory products of guinea pig epicardial fat induce insulin resistance and impair primary adult rat cardiomyocyte function.* J Cell Mol Med, 2011. **15**(11): p. 2399-2410.

290. Herrera, E.A., et al., *Assessment of in vivo fetal growth and placental vascular function in a novel intrauterine growth restriction model of progressive uterine artery occlusion in guinea pigs.* J Physiol, 2016. **594**(6): p. 1553-1561.

291. Kuo, A.H., et al., *Intrauterine growth restriction results in persistent vascular mismatch in adulthood.* J Physiol, 2018. **596**(23): p. 5777-5790.

292. O'Muircheartaigh, J., et al., *White matter development and early cognition in babies and toddlers.* Hum. Brain Mapp., 2014. **35**(9): p. 4475-4487.

293. Yarnykh, V.L., et al., *Quantitative Assessment of Normal Fetal Brain Myelination Using Fast Macromolecular Proton Fraction Mapping.* AJNR Am J Neuroradiol, 2018. **39**(7): p. 1341-1348.

294. Cohen, E., W. Baerts, and F. van Bel, *Brain-Sparing in Intrauterine Growth Restriction: Considerations for the Neonatologist.* Neonatology, 2015. **108**(4): p. 269-276.

295. Pryor, J., *The identification and long term effects of fetal growth restriction.* BJOG: an International Journal of Obstetrics & Gynaecology, 1997. **104**(10).

296. Prayer, D., et al., *MRI of normal fetal brain development.* Eur J Radiol, 2006. **57**(2): p. 199-216.

297. Lazic, S.E. and L. Essioux, *Improving basic and translational science by accounting for litter-to-litter variation in animal models.* BMC Neurosci, 2013. **14**: p. 37.

298. Janot, M., et al., *Bilateral uterine vessel ligation as a model of intrauterine growth restriction in mice.* Reprod Biol Endocrinol, 2014. **12**: p. 62.

299. Spinillo, A., et al., *Cerebroplacental Doppler ratio and placental histopathological features in pregnancies complicated by fetal growth restriction.* J Perinat Med, 2014. **42**(3): p. 321-328.

300. Severi, F.M., et al., *Intrauterine growth retardation and fetal cardiac function.* Fetal Diagn Ther, 2000. **15**(1): p. 8-19.

301. Hagberg, H., D. Peebles, and C. Mallard, *Models of white matter injury: comparison of infectious, hypoxic-ischemic, and excitotoxic insults.* Ment Retard Dev Disabil Res Rev, 2002. **8**(1): p. 30-38.

302. Mari, G. and R.L. Deter, *Middle cerebral artery flow velocity waveforms in normal and small-for-gestational-age fetuses.* Am. J. Obstet. Gynecol., 1992. **166**(4): p. 1262-1270.

Appendices

Appendix A. Ethics Approvals

Western Research

Research Ethics

Use of Human Participants - Ethics Approval Notice

Principal Investigator: Dr. Barbra de Vrijer
File Number: 103845
Review Level: Full Board
Approved Local Adult Participants: 120
Approved Local Minor Participants: 0
Protocol Title: Development of Magnetic Resonance Imaging for Quantitative Assessment of Fetal Liver Fat
Department & Institution: Schulich School of Medicine and Dentistry\Obstetrics & Gynaecology, Western University
Sponsor:
Ethics Approval Date: September 03, 2013
Ethics Expiry Date: March 31, 2018

Documents Reviewed & Approved & Documents Received for Information:

Document Name	Comments	Version Date
Western University Protocol		
Letter of Information & Consent	study group	2013/07/24
Letter of Information & Consent	control group	2013/07/24

This is to notify you that the University of Western Ontario Health Sciences Research Ethics Board (HSREB) which is organized and operates according to the Tri-Council Policy Statement: Ethical Conduct of Research Involving Humans and the Health Canada/ICH Good Clinical Practice Practices: Consolidated Guidelines; and the applicable laws and regulations of Ontario has reviewed and granted approval to the above referenced study on the approval date noted above. The membership of this HSREB also complies with the membership requirements for REB's as defined in Division 5 of the Food and Drug Regulations.

The ethics approval for this study shall remain valid until the expiry date noted above assuming timely and acceptable responses to the HSREB's periodic requests for surveillance and monitoring information. If you require an updated approval notice prior to that time you must request it using the University of Western Ontario Updated Approval Request form.

Member of the HSREB that are named as investigators in research studies, or declare a conflict of interest, do not participate in discussions related to, nor vote on, such studies when they are presented to the HSREB.

The Chair of the HSREB is Dr. Joseph Gilbert. The HSREB is registered with the U.S. Department of Health & Human Services under the IRB registration number IRB 00000940.

Ethics Officer to Contact for Further Information

Erika Basile	Grace Kelly	Vikki Tran

This is an official document. Please retain the original in your files.

Western University, Research

Fw: eSirius3G Notification -- 2020-139 Annual Renewal Approved

Lanette Friesen-Waldner
Wed 2023-03-08 12:32 PM
To: Simran Sethi

From: eSirius3GWebServer
Sent: April 1, 2022 2:39 PM
To: Lanette Friesen-Waldner   Timothy Regnault   acc
Cc: Jennifer McInnis
Subject: eSirius3G Notification -- 2020-139 Annual Renewal Approved

Western

2020-139:2:
AUP Number: 2020-139
AUP Title: A pilot study investigating the Feasibility of Quantification of Fetal Myelin Water Fraction in Guinea Pigs Using MRI - Pilot
Yearly Renewal Date: 04/01/2023
The **annual renewal** to Animal Use Protocol (AUP) 2020-139 has been approved by the Animal Care Committee (ACC), and will be approved through to the above review date. Please at this time review your AUP with your research team to ensure full understanding by everyone listed within this AUP.
As per your declaration within this approved AUP, you are obligated to ensure that:

1. This Animal Use Protocol is in compliance with:
    ○ Western's Senate MAPP 7.12 [PDF]; and
    ○ Applicable Animal Care Committee policies and procedures.
2. Prior to initiating any study-related activities—as per institutional OH&S policies—all individuals listed within this AUP who will be using or potentially exposed to hazardous materials will have:
    ○ Completed the appropriate institutional OH&S training;
    ○ Completed the appropriate facility-level training; and
    ○ Reviewed related (M)SDS Sheets.

Submitted by: McInnis, Jennifer on behalf of the Animal Care Committee
ACC Chair Signature
Dr. Rob Gros,
Animal Care Committee Chair

Animal Care Commitee
The University of Western Ontario

*** THIS IS AN EMAIL NOTIFICATION ONLY. PLEASE DO NOT REPLY ***

Fw: eSirius3G Notification -- 2020-139 Annual Renewal Approved

Lanette Friesen-Waldner
Wed 2023-03-08 12:32 PM
To: Simran Sethi

From: eSirius3GWebServer
Sent: April 1, 2022 2:39 PM
To: Lanette Friesen-Waldner   Timothy Regnault   acc
Cc: Jennifer McInnis
Subject: eSirius3G Notification -- 2020-139 Annual Renewal Approved

Western 🛡️

2020-139:2:
AUP Number: 2020-139
AUP Title: A pilot study investigating the Feasibility of Quantification of Fetal Myelin Water Fraction in Guinea Pigs Using MRI - Pilot
Yearly Renewal Date: 04/01/2023
The **annual renewal** to Animal Use Protocol (AUP) 2020-139 has been approved by the Animal Care Committee (ACC), and will be approved through to the above review date. Please at this time review your AUP with your research team to ensure full understanding by everyone listed within this AUP.
As per your declaration within this approved AUP, you are obligated to ensure that:

1. This Animal Use Protocol is in compliance with:
   ○ Western's Senate MAPP 7.12 [PDF]; and
   ○ Applicable Animal Care Committee policies and procedures.
2. Prior to initiating any study-related activities—as per institutional OH&S policies—all individuals listed within this AUP who will be using or potentially exposed to hazardous materials will have:
   ○ Completed the appropriate institutional OH&S training;
   ○ Completed the appropriate facility-level training; and
   ○ Reviewed related (M)SDS Sheets.

Submitted by: McInnis, Jennifer on behalf of the Animal Care Committee
ACC Chair Signature
Dr. Rob Gros,
Animal Care Committee Chair

Animal Care Commitee
The University of Western Ontario

*** THIS IS AN EMAIL NOTIFICATION ONLY. PLEASE DO NOT REPLY ***

eSirius3G Notification -- 2021-022 New Protocol Approved

eSirius3GWebServer
Thu 2021-11-18 1:38 PM

To: Lanette Friesen-Waldner   Timothy Regnault   **acc**

Cc: ACC Office   Mgrsmtg
UWO Logo

AUP Number: 2021-022
PI Name: Regnault, Timothy
AUP Title: Hyperpolarised 13C MRI of Placental Metabolism in IUGR
Approval Date: 11/01/2021

Official Notice of Animal Care Committee (ACC) Approval:

Your new Animal Use Protocol (AUP) 2021-022:1: entitled " Hyperpolarised 13C MRI of Placental Metabolism in IUGR" has been APPROVED by the Animal Care Committee of the University Council on Animal Care. This approval, although valid for up to four years, is subject to annual Protocol Renewal.

Prior to commencing animal work, please review your AUP with your research team to ensure full understanding by everyone listed within this AUP.

As per your declaration within this approved AUP, you are obligated to ensure that:

1. This Animal Use Protocol is in compliance with:
    ○ Western's Senate MAPP 7.12 [PDF]; and
    ○ Applicable Animal Care Committee policies and procedures.
2. Prior to initiating any study-related activities—as per institutional OH&S policies—all individuals listed within this AUP who will be using or potentially exposed to hazardous materials will have:
    ○ Completed the appropriate institutional OH&S training;
    ○ Completed the appropriate facility-level training; and
    ○ Reviewed related (M)SDS Sheets.

Submitted by: Copeman, Laura on behalf of the Animal Care Committee

ACC Chair Signature

Dr. Rob Gros,
Animal Care Committee Chair

_____

Animal Care Commitee
The University of Western Ontario

Appendix B. Copyright Permissions

JOHN WILEY AND SONS LICENSE
TERMS AND CONDITIONS

Mar 03, 2023

This Agreement between Ms. Simran Sethi ("You") and John Wiley and Sons ("John Wiley and Sons") consists of your license details and the terms and conditions provided by John Wiley and Sons and Copyright Clearance Center.

License Number	5501370663737
License date	Mar 03, 2023
Licensed Content Publisher	John Wiley and Sons
Licensed Content Publication	Journal of Magnetic Resonance Imaging
Licensed Content Title	Quantification of 1.5 T T1 and T2* Relaxation Times of Fetal Tissues in Uncomplicated Pregnancies
Licensed Content Author	Simran Sethi, Stephanie A. Giza, Estee Goldberg, et al
Licensed Content Date	Feb 15, 2021
Licensed Content Volume	54
Licensed Content Issue	1
Licensed Content Pages	9
Type of use	Dissertation/Thesis

JOHN WILEY AND SONS LICENSE
TERMS AND CONDITIONS

Mar 03, 2023

This Agreement between Ms. Simran Sethi ("You") and John Wiley and Sons ("John Wiley and Sons") consists of your license details and the terms and conditions provided by John Wiley and Sons and Copyright Clearance Center.

License Number	5501371145536
License date	Mar 03, 2023
Licensed Content Publisher	John Wiley and Sons
Licensed Content Publication	Journal of Magnetic Resonance Imaging
Licensed Content Title	Feasibility of MRI Quantification of Myelin Water Fraction in the Fetal Guinea Pig Brain
Licensed Content Author	Charles A. McKenzie, Timothy R.H. Regnault, Brian Sutherland, et al
Licensed Content Date	Oct 14, 2022
Licensed Content Volume	0
Licensed Content Issue	0
Licensed Content Pages	9
Type of use	Dissertation/Thesis

JOHN WILEY AND SONS LICENSE
TERMS AND CONDITIONS

Mar 03, 2023

This Agreement between Ms. Simran Sethi ("You") and John Wiley and Sons ("John Wiley and Sons") consists of your license details and the terms and conditions provided by John Wiley and Sons and Copyright Clearance Center.

License Number	5501390363908
License date	Mar 03, 2023
Licensed Content Publisher	John Wiley and Sons
Licensed Content Publication	Journal of Magnetic Resonance Imaging
Licensed Content Title	So You Want to Image Myelin Using MRI: An Overview and Practical Guide for Myelin Water Imaging
Licensed Content Author	Jongho Lee, Jae-Won Hyun, Jieun Lee, et al
Licensed Content Date	Feb 3, 2020
Licensed Content Volume	53
Licensed Content Issue	2
Licensed Content Pages	14
Type of use	Dissertation/Thesis
Requestor type	University/Academic

RE: Copyright Permission for Figure

christiane.albrecht
Fri 2023-03-03 4:59 PM
To: Simran Sethi

You don't often get email from   Learn why this is important

Dear Simran Sethi,
thank you for asking. I am happy that you like our figure, feel free to use it in your thesis.
Good luck and best wishes
Christiane

From: Simran Sethi
Sent: 03 March 2023 16:24
To: Albrecht, Christiane (IBMM)
Subject: Copyright Permission for Figure

Hello Dr. Albrecht,

My name is SImran Sethi, and I am a Ph.D. Candidate at Western University in London, Ontario, Canada. I am currently writing my dissertation entitled "*In Vivo* MR Relaxometry for Fetal Tissue Development". M
and would like to use one of your figures in my dissertation. The figure I would like to use is Figure 1 in Elad *et al., Have We Neglected the Role of Fetal Endothelium in Transplacental Transport.* Traffic Interchange in 2014. I've attached the figure and paper for reference.

My thesis will be available in full-text on the internet for reference, study, and/or copy. Except in situations where a thesis is under a delay of publication or restriction, the electronic version will be accessible through the Western Libraries web pages, the Library's web catalogue, and also through web search engines. I will also be granting Library and Archives Canada and ProQuest/UMI a non-exclusive license to reproduce, loan, distribute, or sell single copies of my thesis by any means and in any form or format. These rights will in no way restrict the republication of the material in any other form by you or by others authorized by you.

Since all rights and permission of the figure are owned by you, I am writing to formally request your permission to use the figure in my dissertation. If there is a form I need to complete or submit the request elsewhere as well, please let me know.

Thank you so much for your time and consideration, and I look forward to hearing from you.

Best Regards,

Simran Sethi

Curriculum Vitae

Name:	Simran Sethi

Post-secondary Education and Degrees:

The University of Western Ontario
London, Ontario, Canada
2014-2018 B.Sc.

The University of Western Ontario
London, Ontario, Canada
2018-2023 Ph.D.

Honours and Awards:

Natural Sciences and Engineering Research Council of Canada
Postgraduate Scholarship - Doctoral
2021-2024

Queen Elizabeth II Ontario Graduate Scholarship
2021-2022 (declined)

Children's Health Research Trainee Award
2020-2021

Related Work Experience

Teaching Assistant
The University of Western Ontario
2019-2023

Summer Research Student
The University of Western Ontario
2018

Publications:

1. Stephanie A. Giza, Tianna L. Koreman, Michael R. Miller, **Simran Sethi**, Genevieve D. Eastabrook, Debbie A. Penava, Charles A. McKenzie, Barbra de Vrijer. (2023). *Clinical Correlations with Fetal Adipose Tissue as Quantified by Magnetic Resonance Imaging.* Pediatric Radiology. In review.

2. **Simran Sethi,** Lanette J. Friesen-Waldner, Trevor P. Wade, Marc Courchesne, Karen Nygard, Ousseynou Sarr, Brian Sutherland, Timothy R.H. Regnault, Charles A. McKenzie. (2022). *Feasibility of MRI Quantification of Myelin Water Fraction in the Fetal Guinea Pig Brain.* Journal of Magnetic Resonance Imaging. DOI: 10.1002/jmri.28482

3. Gurneet Jassal, Ornela Kljakic, **Simran Sethi**, Cailey Salagovic, Neha Khemani, Kara Hannah. (2022). *Inspiring Diversity in STEM Conference 2022*. Undergraduate Research in Natural and Clinical Science and Technology. 6(1). DOI: 10.26685/urncst.386.

4. **Simran Sethi,** Stephanie A. Giza, Estee Goldberg, Mary-Ellen E.T. Empey, Sandrine de Ribaupierre, Genevieve D.M. Eastabrook, Barbra de Vrijer, Charles A. McKenzie. (2021). *Quantification of 1.5 T T_1 and T_2^* Relaxation Times of Fetal Tissues in Uncomplicated Pregnancies. Journal of Magnetic Resonance Imaging.* 54(1): 113-121. DOI: 10.1002/jmri.27547.

5. Stephanie A. Giza, Tianna L. Koreman, **Simran Sethi**, Michael R. Miller, Debbie A. Penava, Genevieve D. Eastabrook, Charles A. McKenzie, Barbra de Vrijer. (2021). *Water-fat magnetic resonance imaging of adipose tissue compartments in the normal third trimester fetus*. Pediatric Radiology. 51(7): 1214-1222. DOI: 10.1007/s00247-020-04955-z.

6. Stephanie A. Giza, **Simran Sethi**, Lauren M. Smith, Mary-Ellen E.T. Empey, Lindsay E. Morris, Charles A. McKenzie. (2020). *The Application of In-Utero Magnetic Resonance Imaging in the study of Developmental Origins of Health and Disease*. Journal of Developmental Origins of Health and Disease. 12(2): 193-202. DOI: 10.1017/S2040174420001154.

Conference Proceedings:

1. Stephanie A. Giza, **Simran Sethi,** Genevieve D.M. Eastabrook, Barbra de Vrijer, Charles A. McKenzie. High Flip Angle Chemical-Shift Encoded MRI for Imaging Fetal Adipose Tissue. International Society of Magnetic Resonance in Medicine Annual Meeting 2022. Digital poster presentation at International Society of Magnetic Resonance in Medicine Annual Meeting *in Toronto, Canada* on June 3-8, 2023.

2. Stephanie A. Giza, **Simran Sethi,** Genevieve D.M. Eastabrook, Barbra de Vrijer, Charles A. McKenzie. Increasing Signal of Water-Fat MRI for Imaging Fetal Adipose Tissue. Canadian National Perinatal Research Meeting 2023. Poster presentation at Canadian National Perinatal Research Meeting *in Montebello, Quebec* on May 23-26, 2023.

3. **Simran Sethi,** Lanette J. Friesen-Waldner, Trevor P. Wade, Marc Courchesne, Karen Nygard, Ousseynou Sarr, Brian Sutherland, Timothy R.H. Regnault, Charles A. McKenzie. Quantifying Fetal Myelin Content in Guinea Pigs with MRI. Canadian National Perinatal Research Meeting 2022. Poster presentation at Canadian National Perinatal Research Meeting *(virtual)* on May 30-June 3, 2022.

4. **Simran Sethi,** Lanette J. Friesen-Waldner, Trevor P. Wade, Marc Courchesne, Karen Nygard, Ousseynou Sarr, Brian Sutherland, Timothy R.H. Regnault, Charles A. McKenzie. Feasibility of Quantifying Myelin Water Fraction in the Fetal Guinea Pig Brain. International Society of Magnetic Resonance in Medicine Annual Meeting 2022. Poster presentation at International Society of Magnetic

Resonance in Medicine Annual Meeting *in London, England* on May 7-May 12, 2022.

5. **Simran Sethi,** Lanette J. Friesen-Waldner, Trevor P. Wade, Marc Courchesne, Karen Nygard, Ousseynou Sarr, Brian Sutherland, Timothy R.H. Regnault, Charles A. McKenzie. Quantifying Myelin Water Fraction in the Fetal Guinea Pig Brain. Imaging Network of Ontario 2021. Power pitch presentation at Imaging Network of Ontario *(virtual)* on March 22-24, 2022.

6. Lindsay E. Morris, Flavien Delhaes, Lanette J. Friesen-Waldner, Trevor P. Wade, Lauren M. Smith, Mary-Ellen E.T. Empey, **Simran Sethi,** Timothy R.H. Regnault, Charles A. McKenzie. Effects of Life-Long Western Diet Consumption on Fetal and Maternal Guinea Pig Body Composition at Mid-Gestation. International Society of Magnetic Resonance in Medicine Annual Meeting 2021. Poster presentation at International Society of Magnetic Resonance in Medicine Annual Meeting *(virtual)* on May 15-20, 2021.

7. **Simran Sethi,** Stephanie A. Giza, Mary-Ellen E.T. Empey, Barbra de Vrijer, Charles A. McKenzie. Quantification of 1.5 T T_1 & T_2^* Relaxation Times of Fetal Lungs, Intraabdominal Organs & Muscle in Uncomplicated Pregnancies. Wavelengths 2021. Oral presentation at Wavelengths *(virtual)* on April 24, 2021.

8. Lindsay E. Morris, Flavien Delhaes, Lanette J. Friesen-Waldner, Trevor P. Wade, Lauren M. Smith, Mary-Ellen E.T. Empey, **Simran Sethi,** Timothy R.H. Regnault, Charles A. McKenzie. Fetoplacental and Maternal Body Composition Effects of Life Long Western Diet Consumption at Mid-Gestation Guinea Pig Pregnancy. Imaging Network of Ontario 2021. Power pitch presentation at Imaging Network of Ontario *(virtual)* on March 23-24, 2021.

9. **Simran Sethi,** Stephanie A. Giza, Mary-Ellen E.T. Empey, Barbra de Vrijer, Charles A. McKenzie. Quantification of T_1 & T_2^* Relaxation Times of Fetal Adipose Tissue & Fetal Muscle at 1.5 T. Imaging Network of Ontario 2020.

Poster presentation at Imaging Network of Ontario *(virtual)* on March 26-27, 2020.

10. **Simran Sethi,** Stephanie A. Giza, Mary-Ellen E.T. Empey, Barbra de Vrijer, Charles A. McKenzie. Quantification of T_1 & T_2^* Relaxation Times of Fetal Adipose Tissue & Fetal Muscle at 1.5 T. In-Utero MRI Workshop 2020. Power pitch and poster presentation at In-Utero MRI Workshop in Oxford, England on January 7-10, 2020.

11. Stephanie A. Giza, **Simran Sethi,** Barbra de Vrijer, Charles A. McKenzie. Challenges of Identifying Human Fetal Adipose Tissue using MRI. In-Utero MRI Workshop 2020. Oral and poster presentation at In-Utero MRI Workshop in Oxford, England on January 7-10, 2020.

12. **Simran Sethi,** Stephanie A. Giza, Mary-Ellen E.T. Empey, Barbra de Vrijer, Charles A. McKenzie. Quantification of T_1 & T_2^* Relaxation Times of Fetal Tissues at 1.5 T. London Imaging Discovery Day 2019. Oral presentation at London Imaging Discovery Day on June 12, 2019.

13. **Simran Sethi,** Stephanie A. Giza, Mary-Ellen E.T. Empey, Barbra de Vrijer, Charles A. McKenzie. Quantification of T_1 & T_2^* Relaxation Times of Fetal Fat, Fetal Liver, Fetal Kidney, and Amniotic Fluid at 1.5 T. International Society of Magnetic Resonance in Medicine Annual Meeting 2019. Oral presentation at International Society of Magnetic Resonance in Medicine Annual Meeting in Montréal, Canada on May 11-16, 2019.

14. **Simran Sethi,** Stephanie A. Giza, Mary-Ellen E.T. Empey, Barbra de Vrijer, Charles A. McKenzie. Quantification of T_1 & T_2^* Relaxation Times of Fetal Tissues at 1.5 T. London Health Research Day 2019. Poster presentation at London Health Research Day in London, Canada on April 30, 2019.

15. **Simran Sethi,** Stephanie A. Giza, Mary-Ellen E.T. Empey, Barbra de Vrijer, Charles A. McKenzie. Quantification of T_1 & T_2^* Relaxation Times of Fetal Tissues at 1.5 T. Imaging Network of Ontario 2019. Oral presentation at Imaging Network of Ontario in London, Canada on March 28-29, 2019.

16. Stephanie A. Giza, **Simran Sethi,** Takashi Hashimoto, Barbra de Vrijer, Charles A. McKenzie. Non-alcoholic Fatty Liver Disease Assessment in Obese and Non-obese Pregnant Women with Water-Fat MRI. International Society of Magnetic Resonance in Medicine Annual Meeting 2018. Poster presentation at International Society of Magnetic Resonance in Medicine Annual Meeting in Paris, France on June 16-21, 2018.

17. Stephanie A. Giza, **Simran Sethi,** Takashi Hashimoto, Barbra de Vrijer, Charles A. McKenzie. Fatty Liver Assessment in Obese and Non-obese Pregnant Women with Water-Fat MRI. Imaging Network of Ontario 2018. Poster presentation at Imaging Network of Ontario in Toronto, Canada on March 28-29, 2018.

18. **Simran Sethi,** Stephanie A. Giza, Takashi Hashimoto, Barbra de Vrijer, Charles A. McKenzie. Quantitative Assessment of Fat Accumulation in Liver of Pregnant Women with Normal and Obese Body Mass Index. Inspiring Young Women in STEM 2018. Poster presentation at Inspiring Young Women in STEM in London, Canada on March 18, 2018.